Alma Mater Studiorum - Università di Bologna

DOTTORATO DI RICERCA IN

MECCANICA E SCIENZE AVANZATE DELL'INGEGNERIA

Ciclo 34

Settore Concorsuale: 09/C2 - FISICA TECNICA E INGEGNERIA NUCLEARE

Settore Scientifico Disciplinare: ING-IND/11 - FISICA TECNICA AMBIENTALE

GEOMETRIC OPTIMIZATION OF COMPLEX THERMAL-FLUID DYNAMIC SYSTEMS BY MEANS OF CONSTRUCTAL DESIGN

Presentata da: Andrea Natale Impiombato

Coordinatore Dottorato

Marco Carricato

Supervisore

Cesare Biserni

Co-supervisore

Antonio Barletta

Esame finale anno 2022

GEOMETRIC OPTIMIZATION OF COMPLEX THERMAL-FLUID DYNAMIC SYSTEMS BY MEANS OF CONSTRUCTAL DESIGN

A Dea e Alessio

Abstract

In this work the Constructal Theory is initially exposed in its generality, trying to approach it through examples mostly of a physical-engineering nature. Constructal Theory proposes to see living bodies as elements subject to constraints, which are built with a goal, an objective, which is to obtain maximum efficiency. Constructal Theory is characterized by Constructal Law, which states that if a system has the freedom to morph it develops over time a flow architecture that provides easier access to the currents that pass through it. In this context the term “flow” means everything that invades a territory, such that in a living territory such as the human body it includes flows of heat, electricity and biological fluids, and also flows of mechanical stress.

The Constructal Law is as general as the First and Second Laws of Thermodynamics, but it has a very different purpose which makes it unique and complementary to those laws. While the First Law points to the conservation of energy, both the Constructal Law and the Second Law point to change, that is, to a direction in time. Although the latter two laws share this common feature, they diverge as to purpose. Contrary to the Second Law, the Constructal Law applies to systems that are out of balance, that is, to systems that evolve over time. While the second law deals with state variables, the Constructal Law combines flows and design (size, shape, structure).

The thesis continues with the application of the Constructal Theory for a cardiac bypass shape optimization. Through the Constructal Theory the constraints under which the system is free to morph are defined and, through the classical engineering optimization processes (numerical simulations and optimization algorithms) the optimum conditions are defined, i.e., those conditions that guarantee the minimum resistance to the passage of the fluid. The characterization of the blood flow was an important step in the study of this system, as the heartbeat induces a pulsed regime

inside the veins. Therefore, the simulations conducted in transient regime consider the deformed velocity profile according to the conditions dictated by the pressure gradient established by the heartbeat.

Another no less important aspect is the modelling of the fluid of interest. In literature there are many authors who consider blood to have the characteristics of water; therefore, an accepted and well-established approximation is to consider blood with Newtonian characteristics. However, this approximation is not always accepted, since, under certain stress conditions, the fluid changes its viscosity characteristics. Then it is necessary to identify the parameters and the model suitable for the rheological description of the blood and consider them in the application of the bypass.

Index

1. Constructal Theory Analysis 2

1.1 Constructal Theory and Constructal Law 7

1.2 Constructal Design Method 8

1.3 Examples of Application 9

1.3.1 Constructal Design Approach for Open Cavities Shape optimization 9

1.3.2 Flow System in Earth 15

1.3.3 Other Fields 20

1.4 Tree Network for Fluid Flow 21

1.4.1 T- and Y-Shaped Constructs 22

1.4.1.1 Example 28

1.5 Vascularization of the Systems: the Key of Constructal Theory 31

1.5.1 Influence of the Branching level on the Temperature Distribution 32

1.5.2 Influence of the Branching level on the Pressure Loss 34

1.6 Digression on Constructal Theory from the World of Science 36

2. Pulsatile Blood Flow 40

2.1 Pulsatile Flow Problem in a Circular Section Duct 40

2.2 Approximation of Womersley Velocity Profile 45

3. Optimization of a Cardiac Bypass Graft by Constructal Design ... 52

3.1 Introduction 53

3.2 Methodology 55

3.2.1 Constructal Design 55

3.2.2 Problem Formulation 58

3.2.3 Mathematical Modelling of Unsteady Blood Flow 59

3.2.4 Boundary Conditions and Initial Conditions 60

3.2.5 Numerical Method and Computational Grid 61

3.2.6 Response Surface Methodology 64

3.3 Results and Discussion 65

3.4 Results Extension 67

3.5 Concluding Remarks 69

4. Effect of the Bypass Attachment Point on Resistance to Flow by Constructal Design 72

4.1 Introduction 72
4.2 Methodology 75
4.2.1 Constructal Design 75
4.2.2 Mathematical Modelling 78
4.2.3 Numerical Method and Computational Grid 79
4.2.4 Procedure 82
4.3 Results and Discussion 83
4.4 Conclusions 88
5. Fluid Models Comparison for the Study of the Bypass 90
5.1 Classification of Fluid Behaviour 90
5.1.1 Definition of a Newtonian Fluid 90
5.2.1 Non-Newtonian Fluid behaviour 96
5.1.2.1 Time-Independent 97
5.2 Comparison of Different Bypass Fluid Models 109
5.2.1 Results 113
6 Conclusion 124
7 List of Publications 126
Appendix A: Pulsatile Flow Rate Description 128
Bibliography 130

List of Figures

Figure 1. The effect of svelteness (S_v) on the importance of local pressure losses relative to distributed friction losses in a pipe with sudden enlargement in cross-section. 5

Figure 2. Isothermal lateral intrusion into a two-dimensional conducting body with uniform heat generation. 10

Figure 3. The minimization of the global thermal resistance when the external shape of the heat generating body is fixed. 12

Figure 4. The effect of the external shape H/L on the global thermal resistance minimized in Figure 3. 12

Figure 5. The optimal shape of the cavity as function of H/L and φ. 12

Figure 6. T-cavity configuration: the first construct. 13

Figure 7. The effect of the ratio D_0/D_1 on the minimized $\boldsymbol{Tmaxmin}$ and the corresponding optimal ratio $(L_0/L_1)opt.$ 14

Figure 8. The effect of the ratio D_0/D_1 and ϕ_0 on the minimized global thermal resistance. 14

Figure 9. The effect of ψ and D_0/D_1 on the minimized global thermal resistance. 14

Figure 10. (a) Root shape with power-law diameter; (b) Constructal root design: conical shape and longitudinal tubes with constant (z-independent) diameters, density, u and v. 15

Figure 11. Slender tree canopy and trunk exposed to a horizontal wind with uniform velocity. 19

Figure 12. Three canopy shapes showing that the optimal trunk shape is near-conical in all cases. 19

Figure 13. T-shaped construct of round tubes 22

Figure 14. Y-shaped construct of round tubes 28

Figure 15. Sketch of proposed YLCHSs for different branching levels: (a) three-dimension view (n=1); (b) side view (n=1); (c) top view (n=1); (d) top view (n=2); (e) top view (n=3); (f) top view (n=4) 31

Figure 16. Comparison of temperature distribution for the heat sink. (a) n=1; (b) n=2; (c) n=3; (d) n=4. 33

Figure 17. Peak temperatures for YLCHSs with different branching levels. 33

Figure 18. Pressure distribution in the channel of the heat sinks: (a) n = 1; (b) n = 2; (c) n = 3; (d) n = 4. 34

Figure 19. Geometry and boundary conditions of the vascularized plate with parallel cooling channels. 37

Figure 20. (Left) Tree-shaped design configuration; (Right) Hybrid design configuration. 37

Figure 21. Temperature distributions of parallel channels design for experimental and numerical studies with (a) 50 W (b) 150 W of heat loads. 38

Figure 22. Temperature distribution of tree-shaped design for experimental and numerical studies with (a) 50 W (b) 150 W of heat loads. 38

Figure 23. Temperature distribution of hybrid design for experimental and numerical studies with (a) 50 W (b) 150 W of heat loads. 39

Figure 24. γ function (continuous line) and its average value 1.99923 (dashed line). Plot considering the example values: ρ = 1060 kg/m3, $\eta = 3.45 \times 10^{-3}$ Pa s, D = 0.003 m, T=1.68 s and Wo=1.61. .47

Figure 25. Comparison between the Womersley profile (line) and the transient Poiseuille profile (dot). Non-dimensional velocity comparison (left); percentage error (right). Plot considering the example value: ρ = 1060 kg/m3, $\eta = 3.45 \times 10^{-3}$ Pa s, D = 0.003 m, T=1.68 s and Wo=1.61.....48

Figure 26. Different shape of thre Womersley function due to the different Womersley number varies. 49

Figure 27. Comparison between the original Womersley profile (line) and the transient Poiseuille function profile (dot) using several times in different sections. The velocity was considerend in m/s. 50

Figure 28. Problem domain. 55

Figure 29. Flowchart showing the application of Constructal Design. 58

Figure 30. Isometric view of the computational mesh for the model with a detailed view of the cross-section in the bypass and native stenotic artery. 61

Figure 31. Dimensionless pressure drop p (a) S=50%, (b) S=75% 66

Figure 32. The ratio between pressure drop with bypass and pressure drop without bypass, (a) S=50%, $p0 = 12.401$ (b) S=75%, $p0 = 254.838$. 67

Figure 33. Plot of Eq.(21) with (a) $S = 50\%$, $ps = 12.401$ and (b) $S = 75\%$, $ps = 254.838$ 69

Figure 34. Problem Domain. 75

Figure 35. Some different bypass graft configuration for L2/D equal to 2.5 (top), 4 (middle) and 6.67 (bottom) at fixed bypass junction angle $\alpha = 30°$ and bypass diameter ratio D1/D = 1. 77

Figure 36 . Constructal design flowchart. 78

Figure 37. Computational mesh. 80

Figure 38. Plane measure. 82

Figure 39. Comparison of dimensionless pressure drop trend for S=50% (left) and S=75% (right) at different Reynolds Number Re. 83

Figure 40. Comparison of dimensional pressure drop trend for S=50% (left) and S=75% (right) at different Reynolds Number Re. 83

Figure 41. Mass flow rate for S = 50% (top: Table 4) and S = 75% (bottom: Table 5). 85

Figure 42. Resistance R for S = 50% (top: Table 6) and S = 75% (bottom: Table 7). 86

Figure 43. Velocity contours (top) and streamlines (bottom) with reference to a couple of points having coordinates L2/D=6.67, S=75%, Re=150 (right), and L2/D=2.27, S=75%, and Re=150 (left). 88

Figure 44. Schematic representation of unidirectional shearing flow. 91

Figure 45. Typical shear stress-shear rate data for a cooking oil and corn syrup 92

Figure 46. Stress components in three-dimensional flow 94

Figure 47. Types of time-independent flow behaviour 96

Figure 48. Schematic representation of shear-thinning behaviour 98

Figure 49. Demonstration of zero shear and infinity shear viscosities for a shear-thinning polymer solution [89] 99

Figure 50. Representative shear stress and apparent viscosity plots for three pseudo-plastic polymer solutions. 100

Figure 51. Representative stress-shear rate data showing viscoplastic behaviour in a meat extract (Bingham plastic) and in an aqueous Carbopol polymer solution (yeld-pseudoplastic). 106

Figure 52. Schematic representation of shear-thickening behaviour. 107

Figure 53. Shear stress-shear rate behaviour of polyvinylchloride (PVC) in dioctylphthalate (DOP) dispersion at 298 K showing regions of shear-thinning and shear-thickening [95] 108

Figure 54. Mesh sectional view. Stenosis degree 50% on the left and stenosis degree 75% on the right. 110

Figure 55. Comparison of the velocity profiles in the inlet (A) and bypass (B) sections for different values of time-steps (t_1, t_2 and t_3) with the results of Vimmr *et al.* [35] (red line) in the case of stenosis degree $S=75\%$, junction angle $\alpha=30°$, diameter ratio $D/d=1$ and Newtonian fluid with density $\rho=1060\ kg\ m^{-3}$ and dynamic viscosity $\mu=3.45*10^{-3}\ Pa\ s$. 112

Figure 56. 3D velocity profiles for Newtonian model at different time steps for both stenosis degree ($S=50\%$ and $S=75\%$) 114

Figure 57. 3D velocity profiles for Carreau model at different time steps for both stenosis degree ($S=50\%$ and $S=75\%$) 115

Figure 58. 3D velocity profiles for Power Law model at different time steps for both stenosis degree (S=50% and S=75%).....116

Figure 59. Contour velocity profiles for Newtonian model at different time steps for both stenosis degree (*S=50%* and *S=75%*) 117

Figure 60. Contour velocity profiles for Carreau model at different time steps for both stenosis degree (*S=50%* and *S=75%*) 118

Figure 61. Contour velocity profiles for Power Law model at different time steps for both stenosis degree (*S=50%* and *S=75%*) 119

Figure 62. 2D velocity profiles comparison along sections A, B, C, D and E for three time steps (t_1, t_2 and t_3) for stenosis degree *S=50%*. Solid line for Newtonian, dashed line for Carreau and dotted line for Power Law.....120

Figure 63. 2D velocity profiles comparison along sections A, B, C, D and E for three time steps (t_1, t_2 and t_3) for stenosis degree *S=75%*. Solid line for Newtonian, dashed line for Carreau and dotted line for Power Law.....121

Figure 64. Oscillatory Shear Index (OSI) 122

List of Tables

Table 1. Numerical value of the Womersley f(2r/D) profile and Poiseuille profile considering the example values: ρ = 1060 kg/m3, η = 3.45 × 10^{-3} Pa s, D = 0.003 m, T = 1.68 s, and Wo = 1.61. ..48

Table 2 Geometric parameters for artery and graft build up. 57

Table 3. Grid Convergence Index (GCI) for different bypass configurations 62

Table 4. Relative error $\varepsilon i,\ i-1$ from the cardiac cycle i to the cycle $(i-1)$ 63

Table 5. Grid Convergence Index (GCI) for arterial narrowing 63

Table 6. Relative error ε_(i,i-1) for arterial narrowing from the cardiac cycle i to the cycle (i-1) ...63

Table 7. Grid Convergence Index (GCI) for S = 50 %, α = 30° and D1/D = 1 (with D = 3 mm)..81

Table 8. Grid Convergence Index (GCI) for S = 75 %, α = 30° and D1/D = 1 (with D = 3 mm). ...81

Table 9. Grid Convergence Index (GCI) stenosis artery. 82

Table 10. Evaluation of the mass fluxes in the measure inlet section (min) stenosis section (mst) and central bypass section (mby) for S = 50 %, = 30° α and D1/D = 1 (with D = 3 mm). 86

Table 11. Evaluation of the mass fluxes in the measure inlet section (min) stenosis section (mst) and central bypass section (mby) for S = 75 %, = 30° α and D1/D = 1 (with D = 3 mm). 87

Table 12. Resistance R values for S = 50%. 87

Table 13. Resistance R values for S = 75%. 87

Table 14. Typical viscosity values at room temperature 93

Table 15. Examples of substances exhibiting non-Newtonian fluid behaviour 95

Table 16. Typical values of power-law constants for a few systems. 103

Table 17. Property values used in simulations for different models. 109

Table 18. Grid Convergence Index (GCI) for different bypass configurations. 111

Table 19. Relative error $\varepsilon i+1, i$ from the cardiac cycle (i+1) to the cycle i in dimensional and non-dimensional format. 111

1. Constructal Theory Analysis

Several research areas have used the Constructal Theory as a method for the problem solving. Some of the main areas of application are: (a) Structures exhibited in nature (also recognized wit “flow system on earth”), (b) Economics, (c) Medical engineering and technology and (d) Thermodynamics (known in the research community as “Constructal thermodynamics”).

This chapter first introduces the Constructive Theory proposed by Adrian Bejan with the aim of exposing in a general way the basic knowledge of this theory in order to specify in detail the expression proposed by Bejan and Lorente [1] which contains all the essence of this theory: *“Constructal Theory is the view that (i) the generation of images of design (pattern, rhythm) in nature is a phenomenon of physics and (ii) this phenomenon is covered by a principle (the Constructal Law). Constructal Design, on the other hand, is the method by which Constructal Law is applied”.*

That is, the Constructal Theory passes through a principle (Constructal Law) applicable through a tool (Constructal Design).

In the second part of this chapter, some of the works present in the literature for the different application areas are examined in order to understand the potential of this approach in an applicative sense.

Before starting the treatment of the Constructal Theory it is important to characterize some objects that are persistent: (i) Constructal Law, (ii) vascularization and (iii) svelteness.

A flow represents the movement of one entity relative to another (the background). To describe a flow, we talk about what the flow carries (fluid, heat or mass), how much it carries (mass flow, heat current, etc.), and where the flow is. A flow system has configuration, design, that is, design.

The Constructal Theory looks at systems with a different eye from the usual one, that is, it wants to consider the configuration (the design) not as something attributed to chance, but as something that follows certain laws.

Different considerations can be made if we consider a macro system made up of many particles each of which is in communication with the system through certain current flows. Every component of the system is placed in the right place, such as neurons in the brain or alveoli in the lung. It is the configuration of these extremely numerous components that makes the system perform at extraordinarily high levels.

Since natural flow systems have a configuration, in theory it is about the emergence of the flow configuration as a physical phenomenon based on a scientific principle. The constructive theory is the mental vision that the generation of the flow structures that we see everywhere in nature (river basins, lungs, atmosphere, circulation, vascularized tissues, etc.) can be reasoned on the basis of an evolutionary approach principle of increasing the access flow over time, that is, the temporal arrow of the animated video of subsequent configurations. That principle is the law of construction [2].

The configuration in space (geometry or drawing) is not a figure that has always existed and is now available to look at and take for granted. The figure is the mechanism by which the flow system achieves the global goal under global constraints. When the flow stops, the figure becomes the fossil of the flow (e.g., dry river bed, snowflake, animal skeleton, abandoned technology, and pyramids of Egypt).

The question that must be asked at the beginning of any architectural research is: "*What is the flow system and what flows through it?*". In the discussion of examples in later sections of the paper, this way of thinking is presented as a design method, mainly with engineering examples. The method, however, is universally applicable and has been used predictively to predict and explain many design features in nature.

There are many researchers from different campuses (Duke; Toulouse; Lausanne; Evora, Portugal; Istanbul; St. John's, Terranova; Pretoria; Shanghai) and

who use the Constructal Theory for better engineering and for better organization of movement and connection of people, goods and information.

With "animal design" as an icon of ideality in nature, the best name for the miniaturization trends we see emerging is vascularization. Any multiscale solid structure that is to be cooled, heated or maintained by our fluid streams must be and will be vascularized. This means trees and wheelbases and solid walls, with every geometric detail sized and positioned in the right place in the available space. These will be solid-fluid structures with multiple scales that are distributed nonuniformly through the volume—so nonuniformly that the “design” may be mistaken as random (chance) by those who do not quite grasp the generating principle, just like in the prevailing view of animal design, where diversity is mistaken for randomness, when in fact it is the fingerprint of the constructal law.

Bejan [2] points out several reasons why the future of engineering belongs to the vascularized. The first is geometric. Our "hands" (streams, entrances, exits) are few, but they must reach the infinity of points of the volume of material we need (the devices, the artifacts, that is, the engineered extensions of the human body). Point-volume and point-to-area flows require the use of tree-shaped configurations. The second reason is that the time to do this work is now. To design highly complex architectures requires strategy (theory) and computational power, which we now possess.

A flow system has new properties that are complementary to those recognized in thermodynamics until now. A flow system has configuration (layout, drawing, architecture), which is characterized by external size (e.g., external length scale L), and internal size (e.g., total volume of ducts V, or internal length scale $V^{1/3}$). This means that a flow system has svelteness, S_v, which is the global geometric property defined as

$$S_v = \frac{external\ flow\ length\ scale}{internal\ flow\ length\ scale} \tag{1.1}$$

This concept is important because it is a property of the global flow architecture. In duct flow, this property describes the relative importance of friction pressure losses distributed along the ducts and local pressure losses concentrated at junctions, bends, contractions, and expansions. It describes the "thinness" of all the lines of the drawing of the flow architecture.

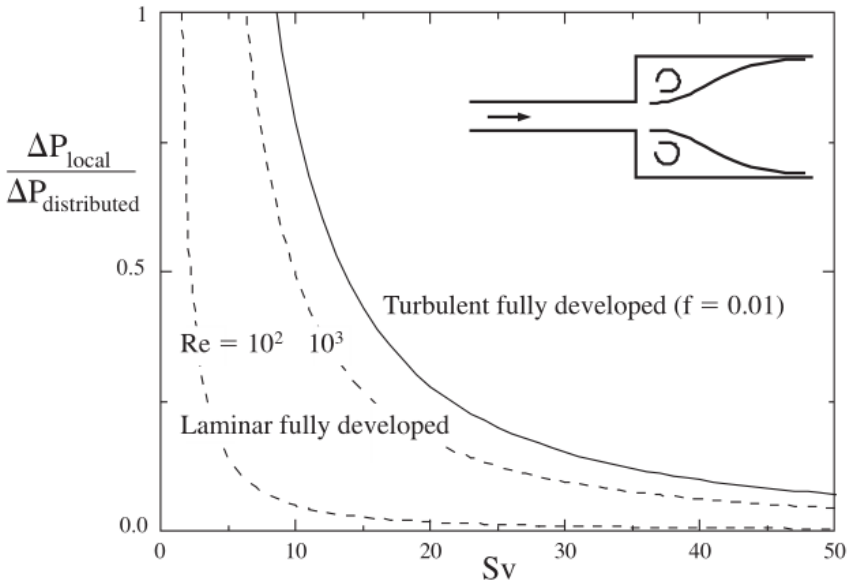

Figure 1. The effect of svelteness (S_v) on the importance of local pressure losses relative to distributed friction losses in a pipe with sudden enlargement in cross-section.

Bejan [2] to illustrate the use of the concept of slenderness, illustrates the following example: consider the flow through two co-linear tubes of different diameter, $D_1<D_2$ (Figure 1). The length of the tube is L_1 and L_2. The abrupt widening of the flow section leads to recirculation and dissipation (imperfection) immediately downstream of the expansion. This effect is measured as a local pressure drop, which is derived by invoking the momentum theorem:

$$\Delta P_{local} = \left[1 - \left(\frac{D_1}{D_2}\right)^2\right]^2 \frac{1}{2}\rho V_1^2 \qquad (1.2)$$

Equation (1.2) is known as the Borda formula. In the calculation of total pressure losses in a complex flow network, it is often convenient to neglect the local pressure losses. But is it correct to neglect the local losses?

The calculation of the svelteness of the network helps answer this question. The svelteness of the flow geometry of Figure 1 is

$$S_v = \frac{L_1 + L_2}{V^{1/3}} \tag{1.3}$$

where V is the total flow volume, namely $V = (\pi/4)(D_1^2 L_1 + D_2^2 L_2)$. The distributed friction losses ($\Delta P_{distributed}$) are associated with fully developed (laminar or turbulent) flow along L_1 and L_2, and have the form for which the friction factors are furnished by the Moody chart.

The derivation of the curves plotted in Figure 1 is derived from Bejan [2]. The distributed ratio $\Delta P_{local}/\Delta P_{distributed}$ decreases sharply as S_v increases. When S_v exceeds the order of 10, the local losses become negligible compared to the distributed losses. It is assumed from this example that S_v is a global property of the "inventory" flow space. This property guides the engineer in evaluating the performance of the flow design.

A flow system is also characterized by performance (function, objective, direction of morphing). Unlike in the black boxes of classical thermodynamics, a flow system has a drawing.

1.1 Constructal Theory and Constructal Law

Constructal Theory is the view that flow configuration (geometry, design) can be reasoned on the basis of a principle of configuration generation and evolution in time toward greater global flow access in systems that are free to morph. That principle is the Constructal law [3].

The phenomena that occur in nature are mostly described by laws of physics. The Constructal Law arise from the consideration that the "*Design*" is a universal physical phenomenon. In this context, it is possible to define the "*Design*" of animated and inanimate objects for different scales [3].

The concept of "*Evolution*" is explained by Bejan [4] in the physics of the Constructal Law:

"For a finite-size flow system to persist in time (to live), its configuration must evolve freely in such a way that provides easier access to the currents that flow through it."

According to the Constructal Law, a system to be defined alive must have two characteristics: it flows (it is not in thermodynamic equilibrium) and it is freely to morph towards configurations that facilitate the flow of all its currents over time.

Life and evolution are seen as a physical phenomenon and therefore belong to physics [5]. To define in a physical sense the position of "*Design*" in nature it is necessary to consider the fact that thermodynamics is based on two fundamental laws: the first law concerns the conservation of energy in any system, while the second law refers to the concept of irreversibility through the increase of entropy of any system. Both laws are defined for a generic system, i.e. a black box. The two laws of thermodynamics give global information on the equilibrium or imbalance of the flows (mass, heat, work, entropy) that cross the black box, but nature is not composed of black boxes, but the configuration must be taken into account.

Bejan [4] pointed out that thermodynamics does not consider the "Design" aspects of the system, but is studied independently of the configuration. To remedy this lack and complete the laws of thermodynamics, the Constructal Law was formulated.

The Constructal Law is not a statement of optimization, maximization, minimization or anything else that refers to a "final project". Constructal Law concern about evolution over time and the fact that the phenomenon of "*Design*" is a dynamic concept. Evolution never ends. The direction of time is the natural phenomenon, while the Constructal Law is the law that governs this phenomenon.

1.2 Constructal Design Method

Constructal Law is applied through Constructal Design, also named Design with Constructal Theory (DCT) [2]. Bejan, from an interview with Kosner [6] and reported by Rocha et al. [3], exposes a Constractal Design as the sequence of rules:

1. *Define Your System*: Identify clearly and unambiguously what constitutes your “system”, that is, the region in space, or the amount of mass that is the subject of your thinking, analysis, and design.
2. *Identify the Flows*: Make sure your system has the freedom to change, and that you understand “what flows” within it, that is, why your system is a “flow system”.
3. *Start Simple*: Allow only one feature of your system to change at first. This endows your system with one degree of freedom. Study if and how changes to this feature increase the flow access of the currents that inhabit your system. Incorporate the first feature with which you found that your system performs best into your design (be alert, this is not the end!)
4. *Add a Degree of Freedom*: Allow a second feature to change freely. As you investigate this second degree of freedom, you will find another best feature and adopt it. With this second feature in place, go back to step 3 and refine that first feature to work with the second.

5. *And Another*: Allow a third feature to vary freely, find the best variant of this feature, and then go back and repeat steps 3 and 4, that is, refine the preceding two features.
6. *And So On*: This is a construction process with no end, except the finite time of the investigator.

Points 1 to 6 are dictated by practice. That is, this is an example of rules to be respected, but nothing prevents other ways to apply the Constructal Law. As Rocha et al. [3] specify, there is no "best" in evolutionary design. There is "better" today, which turns out to be not as good tomorrow. DCT is not a mathematical optimization method. When the system has many degrees of freedom, the Constructal design method can be used in association with some optimization methods, for example, exhaustive search or genetic algorithm [7]. This approach makes possible to study complex systems, that is, systems with a larger number of degrees of freedom.

1.3 Examples of Application

In the work of Rocha et al. [3] a very important review was made of the main articles concerning the application of Constructal Theory to approach problems of vascular flow architectures, tree-shaped cavities, conductive inserts for cooling and networks for distributed heating on the inhabited landscape. For the sake of clarity, the fundamental concepts and results of some of the works proposed in the Constructal Theory literature will be reported in this section.

1.3.1 Constructal Design Approach for Open Cavities Shape optimization

Biserni et al. [8] have conducted a thermal optimization study of the C-shaped cavity. Figure 2 shows the system configuration.

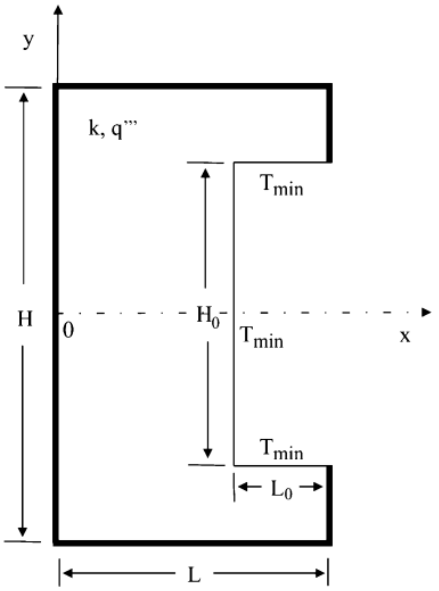

Figure 2. Isothermal lateral intrusion into a two-dimensional conducting body with uniform heat generation.

For the study of the system the following hypotheses were formulated:

- The body has an internal heat source per unit of volume q''' (W/m^3).
- The body is considered isotropic and its thermal conductivity k (W/mK) is constant.
- The external surfaces of the solid body are insulated.
- The thermal current generated by the body ($q'''A$) is removed by the cavity whose walls are kept at a constant temperature T_{min}.
- The dimensionless performance indicator is defined as $\tilde{T}_{max} = (T_{max} - T_{min})/(q'''A/k)$.

The system's constrains are defined starting from the definition of the total area

$$A = H\,L \tag{1.3.1.1}$$

and the area of the cavity

$$A_0 = H_0\,L_0 \tag{1.3.1.2}$$

where A and A_0 are fixed. The shape of the body (L, H) and the shape of the cavity (H_0, L_0) are free to move and this change is allowed by the two degrees of freedom. H/L, the ratio between the height and the length of the solid body, and the H_0/L_0, the ratio between the height and the length of the cavity.

Eq.(1.3.1.2) can be replaced by considering the fixed area fraction occupied by the cavity

$$\phi_0 = \frac{A_0}{A} = \frac{H_0\, L_0}{H\, L} \tag{1.3.1.3}$$

The search for best shapes starts by calculating the maximum temperature that occurs in the solid body and the location where it occurs. Changing the value of the degrees of freedom allows calculating the value of the global thermal resistance and discovers what shape has its minimum value. The non-dimensional problem of conduction was solved in a solid region

$$\frac{\partial^2 \tilde{T}}{\partial \tilde{x}^2} + \frac{\partial^2 \tilde{T}}{\partial \tilde{y}^2} + 1 = 0 \tag{1.3.1.4}$$

where the non-dimensional quantities were defined as

$$\tilde{T} = \frac{(T - T_{min})}{\frac{q''' A}{k}} \tag{1.3.1.5}$$

$$\left(\tilde{x}, \tilde{y}, \tilde{H}, \tilde{L}, \tilde{H}_0, \tilde{L}_0\right) = \frac{x, y, H, L, H_0, L_0}{A^{1/2}} \tag{1.3.1.6}$$

The boundary conditions are given by the outer surfaces of the external body

$$\frac{\partial \tilde{T}}{\partial \tilde{x}} = 0 \; or \; \frac{\partial \tilde{T}}{\partial \tilde{y}} = 0 \tag{1.3.1.7}$$

while the surfaces of the cavity are isothermal

$$\tilde{T} = 0 \tag{1.3.1.8}$$

Biserni et al. [8] solved this problem numerically for several configurations (H/L, H_0/L_0, φ). Figure 3 shows that there is an optimal ratio H_0/L_0 which minimizes the global thermal resistance for several values of the area fraction for a fixed external aspect ratio ($H/L = 1$). The optimal cavity aspect ratio $(H_0/L_0)_{opt}$ increases and the minimal $\tilde{T}_{max}$ decreases as the area fraction increases. The authors performed this procedure for several values of the ratio H/L and the results are shown in Figure 4. The results indicate that the minimal global thermal resistance decreases as H/L decreases and the area fraction also decreases. The same behavior of the optimal ratio $(H_0/L_0)_{opt}$ is also seen for the minimum global thermal resistance in Figure 5. The authors point

attentions to notice the important that Figure 4 and Figure 5 shows that there is no optimal aspect ratio *H*/*L*.

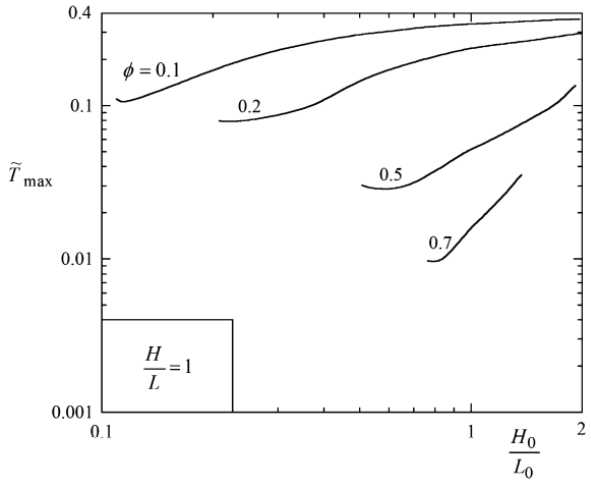

Figure 3. The minimization of the global thermal resistance when the external shape of the heat generating body is fixed.

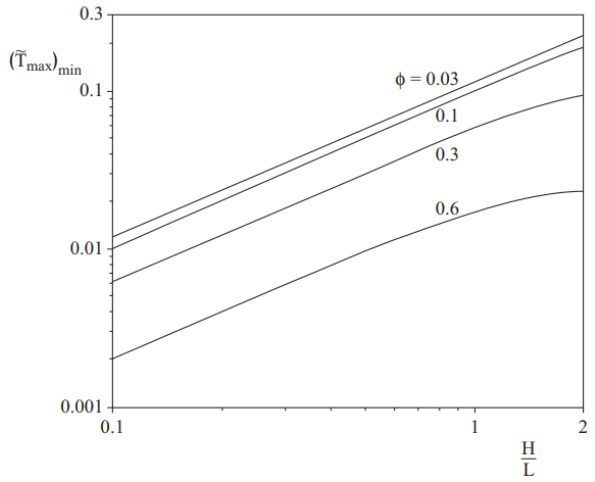

Figure 4. The effect of the external shape *H*/*L* on the global thermal resistance minimized in Figure 3.

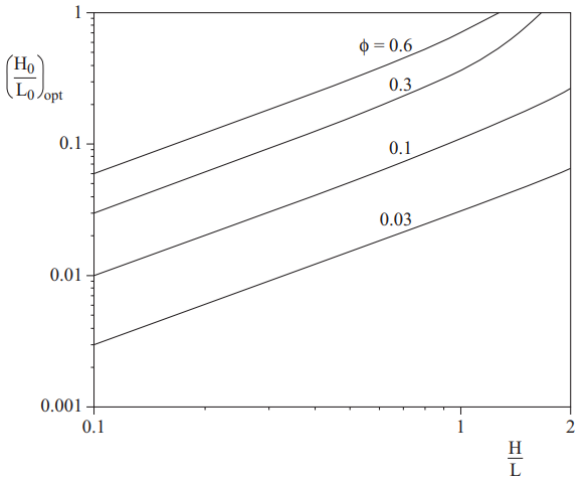

Figure 5. The optimal shape of the cavity as function of *H*/*L* and φ.

The results presented in Figure 5 suggest that the results can be correlated as

$$\left(\frac{H_0}{L_0}\right) \cong \phi \frac{H}{L} \qquad (1.3.1.9)$$

The isothermal assumption considers that the heat transfer coefficient in the cavity surfaces is large enough

Following the philosophy of Constructal Design, one way to find the best configuration of the system is to vary its degrees of freedom. Biserni et al. [8] have considered the modification of the system of Figure 2 with that of Figure 6.

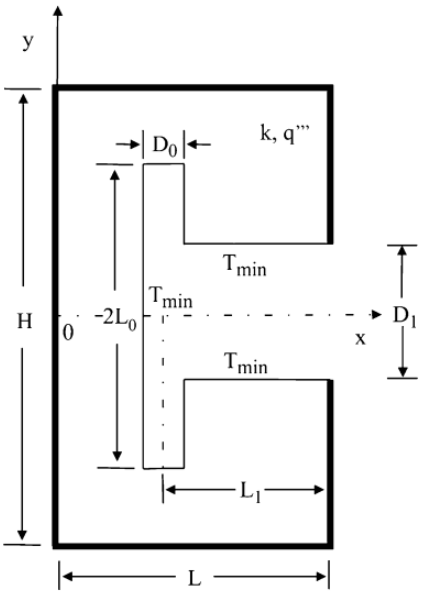

Figure 6. T-cavity configuration: the first construct.

The added bifurcation (also called first construct principle) results in an increase in the degrees of freedom of the system. In fact, this configuration has the addition of two parameters:

$$\phi = \frac{2L_0D_0 + \left(L_1 - \frac{D_0}{2}\right)}{H\ L} \tag{1.3.1.10}$$

$$\psi = \frac{2L_0 + \left(L_1 + \frac{D_0}{2}\right)}{H\ L} \tag{1.3.1.11}$$

that is, the total degrees of freedom of the system are three: H/L, L_0/L and D_0/D.

Figure 7 shows that the results calculated for the optimal configurations with respect to L_0/L_1 are practically insensitive to changes in D_0/D_1. The effect of ϕ and ψ are shown in Figure 8 and Figure 9, respectively. The minimized global thermal resistance decreases as the ϕ and ψ increases, that is, the cavity becomes larger. The best geometries can be correlated when $H/L < 1$ by

$$\frac{(H_0/L_0)_{opt}}{\phi H/L} \sim 1 \tag{1.3.1.12}$$

And

$$\left(\frac{L}{L_0}\right)^2 \sim 1 \tag{1.3.1.13}$$

When the performance of the elemental cavity shown in Figure 2 is compared with the performance of the first construct drawn in Figure 6, it is noted that the T-shaped cavity performs approximately 29% better under the same thermal conditions, uniform heat generation, and the same volume fraction $\phi = 0.1$.

Following the construction principle, one can continue to add degrees of freedom to the system by adding further bifurcations. Biserni et al. [8] and Rocha et al. [9] has also solved the same range of problems by considering the cavity lapped by a fluid. With a Constructal Design method they have achieved an improvement of the results.

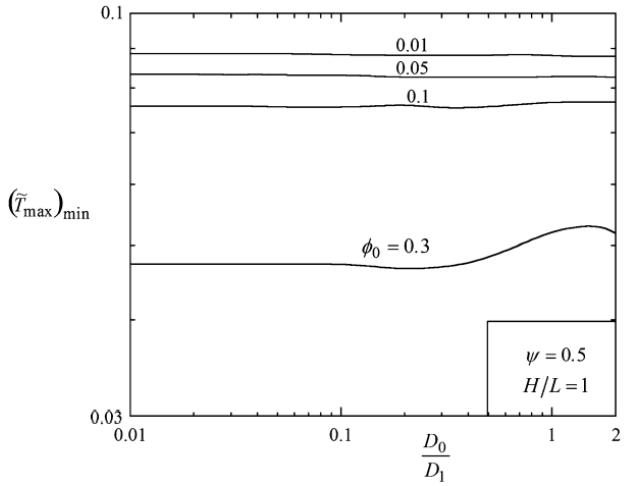

Figure 7. The effect of the ratio D_0/D_1 on the minimized $(\tilde{T}_{max})_{min}$ and the corresponding optimal ratio $(L_0/L_1)_{opt}$.

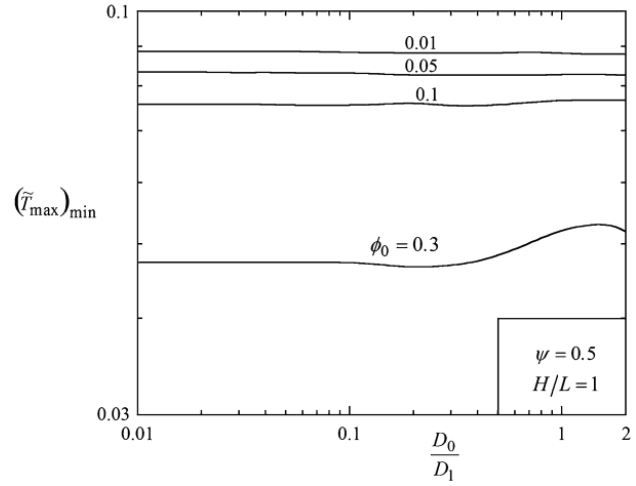

Figure 8. The effect of the ratio D_0/D_1 and ϕ_0 on the minimized global thermal resistance.

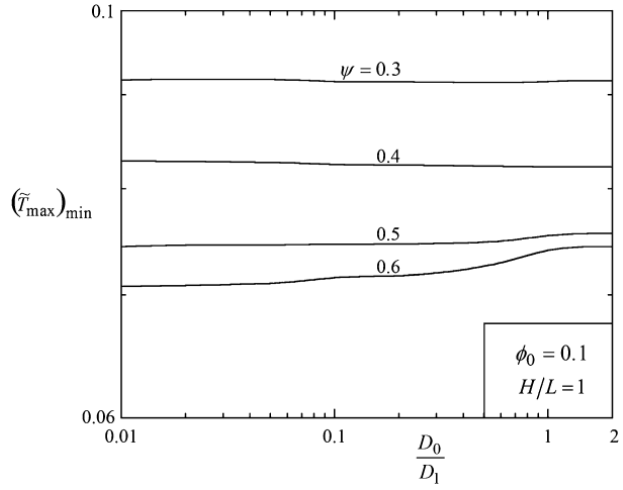

Figure 9. The effect of ψ and D_0/D_1 on the minimized global thermal resistance.

Several work was performed in this area as Lorenzini et al [10] concerns the optimization of the heat exchange in a Y-shaped cavity, meanwhile Biserni et al [11] studied a H-shape cavity. In all cases, the approach proposed by the authors leads to an improvement in performance.

1.3.2 Flow System in Earth

In the context of Constructal Theory, even spatial and temporal structures exhibited in nature are the result of a global process of search for better shapes subject to global and local constraints (Bejan et al. [12]-[13]). The most basic features of tree and forest architecture can be put on a unifying theoretical basis given by the Constructal Law. Trees and forests are viewed as integral components of the much greater global architecture that facilitates the cyclical flow of water and the flow of stresses between wind and ground.

An important example about the plant root design was investigated by Bejan et al. [13];

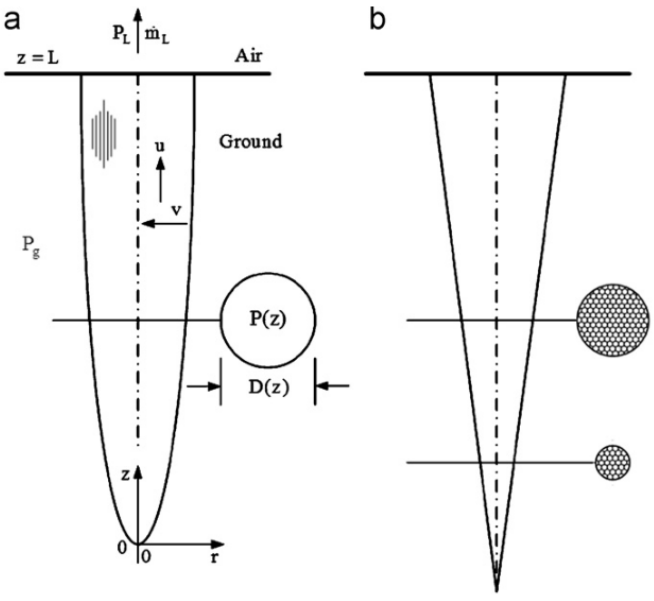

Figure 10. (a) Root shape with power-law diameter; (b) Constructal root design: conical shape and longitudinal tubes with constant (z-independent) diameters, density, u and v.

The plant root is a conduit shaped in such a way that it provides maximum access for the ground water to escape above ground, into the trunk of the plant. The ground

water enters the root through all the points of its surface. In the simplest possible description, the root is a porous solid structure shaped as a body of revolution (Figure 10). The shape of the body (L, $D(z)$) is not known, but the volume is fixed:

$$V = \int_0^L \frac{\pi}{4} D^2 \, dz \tag{1.3.2.1}$$

The flow of water through the root body is in the Darcy regime. The permeability of the porous structure in the longitudinal direction (K_z) is greater than the permeability in the transversal direction (K_r). Anisotropy is due to the fact that the woody vascular tissue (the xylem) is characterized by vessels and fibres that are oriented longitudinally.

The assumption that the (L, D) body is sufficiently slender means that the pressure inside the body depends mainly on longitudinal position, $P(r,z) \cong P(z)$. This slenderness assumption is analogous to the slender boundary layer assumption in boundary layer theory. For Darcy flow, the z volume averaged longitudinal velocity is given by

$$u = -\frac{K_z}{\mu}\frac{dP}{dz} \tag{1.3.2.2}$$

where μ is the fluid viscosity. Because of the $P(r,z) \cong P(z)$ assumption, for the transversal volume averaged velocity v (oriented toward negative r) is it possible to approximate:

$$v \cong \frac{K_r}{\mu}\frac{P_g - P(z)}{D/2} \tag{1.3.2.3}$$

The ground-water pressure (P_g) outside the body is assumed constant. This means that in this model the hydrostatic pressure variation with depth $P_g(z)$ is assumed to be negligible, and that the root sketched in Figure 10 can have any orientation relative to gravity. Ground level is indicated by z=L: here the pressure is P_L, and is lower than P_g. Throughout the body, $P(z)$ is lower than P_g, and the radial velocity v is oriented toward the body centreline.

The conservation of water flow in the body requires

$$d\dot{m} = \rho \, \pi \, D \, v \, dz \tag{1.3.2.4}$$

where $\dot{m}$ is the longitudinal mass flow rate at level *z*:

$$\dot{m} = \rho \frac{\pi}{4} D^2 u \tag{1.3.2.5}$$

and ρ is the density of water. Eqs.(1.3.2.4)-(1.3.2.5) yield

$$\frac{d}{dz}(D^2 u) = 4vD \tag{1.3.2.5}$$

Summing up, the three Eqs.(1.3.2.2)-(1.3.2.3) and Eq.(1.3.2.6) should be sufficient for determining *u*(*z*), *v*(*z*) and *D*(*z*) when the length *L* is specified. Here, the challenge is of a different sort (much greater). It is necessary to determine the shape (*L*, *D*(*z*)) that allows the global pressure difference (P_g - P_L) to pump the largest flow rate of water to the ground level:

$$\dot{m}_L = \rho \frac{\pi}{4} D^2(L) u(L) \tag{1.3.2.7}$$

Subject the volume constraint Eq.(1.3.2.1). The assumption is now made that the unknown function *D*(*z*) belongs to the family of power-law functions:

$$D = bz^m \tag{1.3.2.8}$$

Where *b* and *m* are two constants. Another assumption is that the function *P*(*z*) belongs to the family represented by

$$\frac{P_g - P(z)}{\mu / K_z} = az^n \tag{1.3.2.9}$$

where *a* and *n* are two additional constants. Substituting Eqs.(1.3.2.8)-(1.3.2.9) into Eqs. (1.3.2.2)- (1.3.2.3) and then substitute the resulting *u* and *v* expressions into Eq. (1.3.2.6), it is obtained two compatibility conditions for the assumptions made in Eq. (1.3.2.8) and Eq. (1.3.2.9):

$$m = 1 \tag{1.3.2.10}$$

$$b^2 n(n+1) = 8 \frac{K_r}{K_z} \tag{1.3.2.11}$$

The volume constraint (Eq. (1.3.2.1)) yields a third condition:

$$b^2 L^3 = \frac{12}{\pi} V \tag{1.3.2.12}$$

A fourth condition follows from the statement that the overall pressure difference is fixed, which in view of Eq. (1.3.2.9) means that

$$\frac{P_g - P_L}{\mu/K_z} = aL^n, \qquad constant \tag{1.3.2.13}$$

Finally, the mass flow rate through the $z=L$ end of the body is, cf. Eq.(1.3.2.7):

$$\dot{m}_L = \rho\frac{\pi}{4}(bL)^2\frac{K_z}{\mu}\left(\frac{d\left(P_g - P\right)}{dx}\right)_{z=L} = \rho\frac{\pi}{4}b^2anL^{n+1} \tag{1.3.2.14}$$

for which $b(n)$ and $L(n)$ are furnished by Eq.(1.3.2.11) and Eq.(1.3.2.12). The resulting ground-level flow rate is

$$\dot{m}_L = \rho\frac{\pi}{4}(aL^n)\left(8\frac{K_r}{K_z}\right)^{2/3}\left(\frac{12}{\pi}V\right)^{1/3}\frac{n^{1/3}}{(n+1)^{2/3}} \tag{1.3.2.15}$$

with the observation that (aL^n) is a constant, cf. Eq.(1.3.2.13).

In conclusion $\dot{m}_L$ depends on root shape (n) according to the function $n^{1/3}/(n+1)^{2/3}$. This function is maximum when

$$n = 1 \tag{1.3.2.16}$$

The Constructal root design, subject to volume constraint has the following length and aspect ratio

$$L = \left(\frac{3VK_z}{\pi K_r}\right)^{1/3} \tag{1.3.2.17}$$

$$\frac{L}{D_L} = \frac{1}{2}\left(\frac{K_z}{K_r}\right)^{1/2} \tag{1.3.2.18}$$

The Constructal root shape is conical. The slenderness of this cone is dictated by the anisotropy of the porous structure $(K_z/K_r)^{1/2}$. The root is more slender when the vascular structure is more permeable longitudinally.

Another important feature of the discovered root geometry is that the longitudinal volume averaged fluid velocity (u) is independent of longitudinal position (z), because n=1 means that dP/dz =constant, and

$$u = \frac{K_z}{\mu}\frac{P_g - P_L}{L} \quad (0 < z < L) \tag{1.3.2.19}$$

$$\dot{m}_L = \rho \frac{\pi}{4} (bL^n) u = \frac{K_z}{v} \left(P_g - P_L\right) (3V)^{1/3} \left(\pi \frac{K_r}{K_z}\right)^{2/3} \qquad (1.3.2.20)$$

The morphological implications of this theoretical feature are important. If the porous structure is a bundle of tiny capillary channels, then the fluid velocity through each tube must be constant, and must not depend on the size of the root cross-section that the channel pierces.

Bejan et al. [13] through the same mental scheme describes the natural tendency of objects of nature to assume certain forms. Trunk and canopy (and forest) architecture (Figure 11 and Figure 12) is driven by the same "mental viewing", i.e. the tendency to generate flow access for water from ground to air. The optimal trunk shape is near-conical in all cases, in the hypothesis that the canopy has a shape that belongs in the family of power law functions.

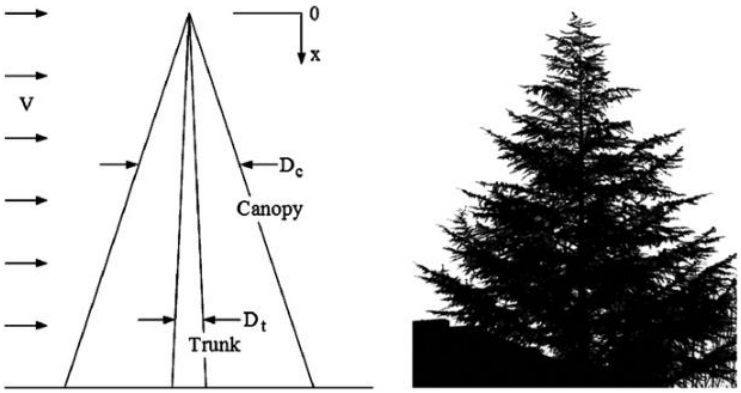

Figure 11. Slender tree canopy and trunk exposed to a horizontal wind with uniform velocity.

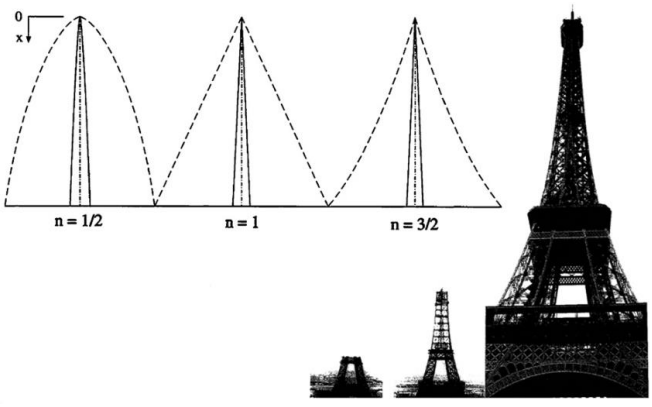

Figure 12. Three canopy shapes showing that the optimal trunk shape is near-conical in all cases.

The largest flow system on earth from the point of view of the Constructal Theory of organization in nature has been examined theoretically. Thermodynamically, the earth as a whole is a non-equilibrium closed system-flow system with heat input and heat rejection, and with internal flows [14].

1.3.3 Other Fields

Bejan's theory has also been stretched to economics using the same principle of cost minimization in the transport of goods [15]: the fundamental contribution of this extension is that the ``law of parsimony'' emerges as the economics analogue of the resistance minimization principle, already recognized in physics and engineering.

Bejan's theory has also been applied to hyperthermia cancer treatments (medicine) [16]: the crucial problem is to keep the temperature of the normal tissue surrounding the tumor below a certain threshold so as not to cause damage to the tissue.

Constructal theory is also named "*Constructal Thermodynamics*" [17] since it has been considered as a sort of evolution and spreading of the laws of thermodynamics. Thermal sciences expanded in new directions, most vigorously now because of the Constructal Law, which unifies science (physics, biology, engineering, social sciences). Constructal thermodynamics [5] places the concepts of life, design, and evolution in physics. It constitutes a wide open door to new advances, especially in areas where design evolution is key to performance, for example, in logistics [18], biological evolution [19], art [20], and business and economics [21].

1.4 Tree Network for Fluid Flow

Bejan [2] explain how for a fluid flows, the tree-shaped layouts are an optimum configuration for the overall benefit of the system. The purpose is to generate the design intended as (i) configuration, (ii) geometry and (iii) geography of the flow system. The simplest class of tree-shaped streams are the T- and Y-shaped ones. More space is devoted to shafts that connect a circle with its center, because these near-radial structures will be used in heating and cooling applications. The methods to reduce the cost and time required to generate tree architectures consist, for example, of minimizing path lengths everywhere and optimizing the confluence angles between the different branches.

The purpose of a tree network is to create a flow connection between a point (source, sink) and a continuum, an infinity of points (line, area, volume). In civil engineering is it possible to see the water distribution system consisting of a region of space (area) in which there are a certain number of points (consumers). The branches of the sewer system are the way in which water is brought to the user. The tree-shaped streams on continuums are the rule in nature, not the exception. They define the design of animate and inanimate flow systems: lungs, vascularized tissues, nervous systems, river basins and deltas, lightning, snowflakes, vegetation, and so on.

Dendritic flow configurations are widely reflected in physiology and geophysics. From the point of view of natural sciences, tree-shaped flows are examples of a spontaneous organization and optimization of the system. In contrast to this, the constructive view is theory: flow architectures such as the tree are the result of a process of evolution towards greater access to the global flow. Tree flows are deductible from the construction law.

Tree-shaped flows persist in time (in nature, as well as in engineering) because they are efficient and use the available space to the maximum. These structures are important for technological progress, because the relationship between efficiency and compactness is fundamental for the design and integration of an increasing number of

ever smaller functioning components. Tree-shaped architectures are therefore the new weapon in the revolution of miniaturization and vascularization.

1.4.1 T- and Y-Shaped Constructs

Starting with a simple case of tree flow shown in Figure 13. The maximum-access geometry for fluid flow between two points is the straight duct with round cross-section. The round shape holds for both laminar and turbulent flow. It is a very robust design feature: nearly round shapes are almost as effective as the perfectly round shape.

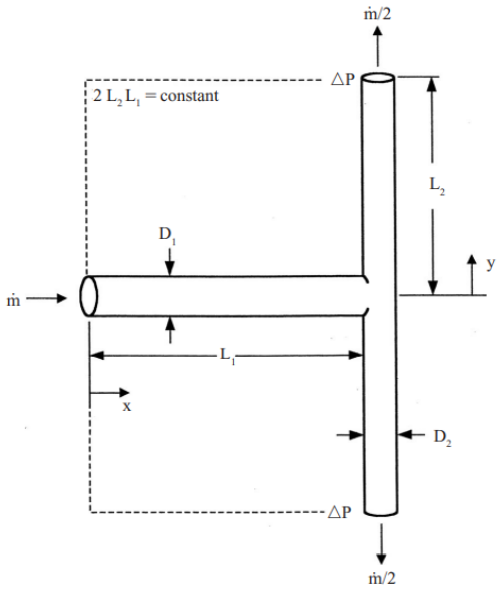

Figure 13. T-shaped construct of round tubes

The simple tree is the T-shaped construct of round tubes shown if Figure 13. The flow connects one point (source or skin) with two points. There are two global constraints: (a) the total duct volume

$$V = \frac{\pi}{4}(D_1^2 L_1 + 2D_2^2 L_2), constant \qquad (1.4.1.1)$$

and (b) the total space (area) occupied by the construct

$$A = 2L_2 L_1, constant\ A = H\ L \qquad (1.4.1.2)$$

Regardless of the size of the system, the image Figure 13 is decided by selecting the values of two dimensionless ratios, D_1/D_2 and L_1/L_2. The latter represent the shape of the area A. Both are free to vary; therefore, they represent the 2 degrees of freedom of the drawing (flow architecture). In the following analysis, Bejan [2] has determine the

two aspect ratios by minimizing the total flow resistance posed by the T-shaped construct on area A.

The optimal ratio D_1/D_2 turns out to be independent of the shape of A, and is determined as follows. Assume that the flow through every tube is in the Poiseuille regime. This means that the svelteness of the construct is large, $S_v=A^{1/2}/V^{1/3}$. The longitudinal pressure drops for the two tube sizes are

$$\Delta P_1 = C\dot{m}_1 \frac{L_1}{D_1^4} \tag{1.4.1.3}$$

$$\Delta P_2 = C\dot{m}_2 \frac{L_2}{D_2^4} \tag{1.4.1.4}$$

where $C=128\ \upsilon/\pi$, and υ is the kinematic viscosity of the fluid. The two mass flow rates are related by

$$\frac{\dot{m}_1}{\dot{m}_2} = 2 \tag{1.4.1.5}$$

Because the assumed T configuration is symmetric: symmetric rules out a flow imbalance between the streams that flow through the two L_2 tubes. Without symmetry, there is no equipartitioning of $\dot{m}_1$ streams into two $\dot{m}_2$ streams.

The overall pressure drop is $\Delta P = \Delta P_1 + \Delta P_2$. After using Eq.(1.4.1.3) trough Eq.(1.4.1.5), we find the global flow resistance:

$$\Delta \mathrm{P} = C\dot{m}_1 R_{lam} \tag{1.4.1.6}$$

where R_{lam} is a factor that depends solely on the geometry of the T:

$$\mathrm{R_{lam}} = \frac{L_1}{D_1^4} + \frac{L_2}{2D_2^4} \tag{1.4.1.7}$$

To minimize R_{lam}, our thoughts guide us to increasing both D_1 and D_2. This idea is not workable because the diameters D_1 and D_2 are related through the volume constraint (1.4.1.1): D_1 and D_2 cannot be increased indefinitely and independently.

The correct path to the optimal D_1 and D_2 values is to minimize R_{lam} subject to keeping V constant. Using the Lagrange multipliers method is it possible to minimize the expression shown in Eq.(1.4.1.7) subject to the constant expressed in Eq.(1.4.1.1). Defining the following function:

$$\phi = \frac{L_1}{D_1^4} + \frac{L_2}{2D_2^4} + \lambda(D_1^2 L_1 + 2D_2^2 L_2) \qquad (1.4.1.8)$$

which was obtained by combining linearly the two expressions. The factor λ is a constant (the Lagrange multiplier), which can be determined from the constraint (1.4.1.1) later, after optimization. The extremum of φ is found by solving the system of equations:

$$\frac{\partial \phi}{\partial D_1} = \frac{-4L_1}{D_1^5} + \lambda 2 D_1 L_1 = 0 \qquad (1.4.1.9)$$

$$\frac{\partial \phi}{\partial D_2} = \frac{-4L_2}{2D_2^5} + \lambda 4 D_2 L_2 = 0 \qquad (1.4.1.10)$$

From which L_1 and L_2 will drop out. This is how we discover that the layout (L_1, L_2) does not influence the diameter ratio D_1/D_2. Solving Eqs.(1.4.1.9) and (1.4.1.10) for $D_1(\lambda)$ and $D_2(\lambda)$, and eliminating λ we find

$$\frac{D_1}{D_2} = 2^{1/3} \qquad (1.4.1.11)$$

This ratio was first reported in physiology by Hess [22] and 12 years later by Murray [23]; therefore, we shall refer to it as the Hess-Murray rule. This result is remarkable for its robustness: the optimal D_1/D_2 ratio is independent of the assumed tube lengths. It is also independent of the relative positions of the three tubes; hence, it is independent of geometry.

Another remarkable consequence of Eq.(1.4.1.11) is that the wall shear stress along the D_1 tube is the same as along the D_2 tube. The design distributes stresses uniformly through the solid that houses the bifurcating flow structure.

The Hess-Murray rule holds for perfectly symmetric bifurcations. When the mother channel (D_1, L_1) splits into two dissimilar daughter channels, (D_2, L_2) and (D_3, L_3), the optimal size ratios D_1/D_2 and D_2/D_3 depend on the ratio L_2/L_3, which accounts for the lack of symmetry.

It is important to capitalize on an optimization result right after it is obtained. According to Ref. [24], if we substitute Eq. (1.4.1.11) into Eqs. (1.4.1.1) and (1.4.1.7), we obtain

$$\frac{2V}{\pi D_2^2} = 2^{-1/3}L_1 + L_2 \quad (1.4.1.12)$$

$$2D_2^4 R_{lam} = 2^{-1/3}L_1 + L_2 \quad (1.4.1.13)$$

Eliminating D_2 between these two equations we find

$$\frac{8}{\pi^2}V^2 R_{lam} = \left(2^{-\frac{1}{3}}L_1 + L_2\right)^3 \quad (1.4.1.14)$$

in which V is constant. The global resistance R_{lam} decreases when both L_1 and L_2 decrease, but the two tube lengths cannot be varied independently because of the area constraint (1.4.1.2). The best that we can do is to minimize the expression ($2^{-1/3}L_1+L_2$) subject to constraint (1.4.1.2), which is the same as finding the extremum of another aggregate function:

$$\psi = 2^{-1/3}L_1 + L_2 + \mu L_1 L_2 \quad (1.4.1.15)$$

where μ is a new Lagrange multiplier. The ψ extremum is located where its two first derivatives are zero:

$$\frac{\partial \psi}{\partial L_1} = 2^{-1/3} + \mu L_2 = 0 \quad (1.4.1.16)$$

$$\frac{\partial \psi}{\partial L_2} = 1 + \mu L_1 = 0 \quad (1.4.1.17)$$

Eliminating μ between Eqs.(1.4.1.16) and (1.4.1.17), we discover that the optimal shape of the A rectangle that houses the T construct is

$$\frac{L_1}{L_2} = 2^{1/3} \quad (1.4.1.18)$$

Combining this ratio with the A construct (1.4.1.2), we find the optimal lengths $L_1 = 2^{-1/3}A^{1/2}$ and $L_2 = 2^{-2/3}A^{1/2}$, in which $A^{1/2}$ plays the role of length scale.

Combining Eqs. (1.4.1.11) and (1.4.1.18), we find that the pressure drop along the D_1 tube is the same as along the D_2 tube. The uniform distributing of pressure drop from tube to branches is the merit of coupling the Hess-Murray diameter ratio with the lengths ratio determined from the search for the best layout of tubes [24] in a constrained space.

We capitalize on this latest result (Eq. (1.4.1.18)), and by substituting the optimal L_1 and L_2 expressions into Eq.(1.4.1.14), we arrive at the smallest of all possible resistances, which is

$$R_{lam} = \frac{\pi^2 A^{3/2}}{4\,V^2} \tag{1.4.1.19}$$

This corresponds to the best T-shaped architecture, which is represented by Eqs. (1.4.1.11) and (1.4.1.18). The R_{lam} expression (1.4.1.19) makes sense: this is the best (the smallest) that can be achieved by morphing the flow configuration subject to the V and A constraints. Further reductions in R_{lam} can be achieved only by changing the constraints, namely, by increasing V and/or decreasing A.

The integer 2 in the diameter ratio $2^{1/3}$ (Eq.(1.4.1.11)) comes from the assumption of dichotomy (pairing, bifurcation) in the T configuration of Figure 13. If the L_1 tube splits into n identical tubes (L_2, D_2), then $2^{1/3}$ is replaced by $n^{1/3}$. The global resistance of a junction with fixed total tube volume and one mother tube and n identical daughter tubes increases monotonically with n. This means that dichotomy (n = 2) is the best way to configure a junction with Poiseuille flow

The exponent 1/3 in Eq.(1.4.1.11) is a reflection of the assumption of fully developed laminar flow. If in Figure 13 the Poiseuille regime is replaced by fully developed turbulent flow in the fully rough regime, then the exponent 1/3 is replaced by 3/7 and Eq.(1.4.1.11) becomes [24]

$$\frac{D_1}{D_2} = 2^{3/7} \tag{1.4.1.20}$$

The corresponding forms of Eqs. (1.4.1.18) and (1.4.1.19) are

$$\frac{L_1}{L_2} = 2^{1/7} \tag{1.4.1.21}$$

$$R_{turb} = \frac{\pi^{5/2} A^{7/4}}{4^{3/2}\,V^{5/2}} \tag{1.4.1.22}$$

These results are obtained by performing the analysis of Eqs. (1.4.1.1) trough (1.4.1.19) after substituting in place of Eqs.(1.4.1.3) and (1.4.1.4) the corresponding relations for fully developed, fully rough duct flow, namely,

$$\Delta P_1 = C' \dot{m}_1^2 \frac{L_1}{D_1^5} \quad (1.4.1.23)$$

$$\Delta P_2 = C' \dot{m}_1^2 \frac{L_2}{D_2^5} \quad (1.4.1.24)$$

where C' is a constant factor. In place of Eq.(1.4.1.7), we find that the global flow resistance $\Delta P/\dot{m}_1^2$ is proportional to the geometric expression

$$R_{turb} = \frac{L_1}{D_1^5} + \frac{L_2}{4D_2^5} \quad (1.4.1.25)$$

The smallest of all the values of R_{turb} is given in Eq.(1.4.1.13) and it corresponds to the aspect ratios optimized in Eqs. (1.4.1.11) and (1.4.1.12).

The smallest R_{lam} and R_{turb} are surprisingly close to each other, even though their respective flow regimes are drastically different. The roles played by the global constraints (A, V) are clear. Flow resistances are smaller when the bathed territories are smaller and when the tube volumes are larger. Eqs. (1.4.1.19) and (1.4.1.22) can also be written as

$$R_{lam} = \frac{\pi^2}{4} \frac{Sv^3}{V} \quad (1.4.1.26)$$

$$R_{turb} = \frac{\pi^{5/2}}{4^{3/2}} \frac{Sv^{7/2}}{V^{4/3}} \quad (1.4.1.27)$$

where , again, the svelteness of the T construct is defined as Sv=(external length scale)/(internal length scale)=$A^{1/2}/V^{1/3}$.

The construct of three tubes (Figure 13) can be optimized further by giving the morphing geometry more degrees of freedom. One option is to allow the angle of confluence to vary. This alternative is outlined in Figure 14, where the total space constraint is a disc-shaped area with specified radius (r). in Ref.[24] was founded that when the flow is fully developed and laminar, the optimized flow architecture is represented by $D_1/D_2=2^{1/3}$, α=0.654 rad, and $L_1=L_2=r$. In this configuration the tubes are connected in the center of the disc, and the angle between the two L_2 tubes is very close to 75 degrees.

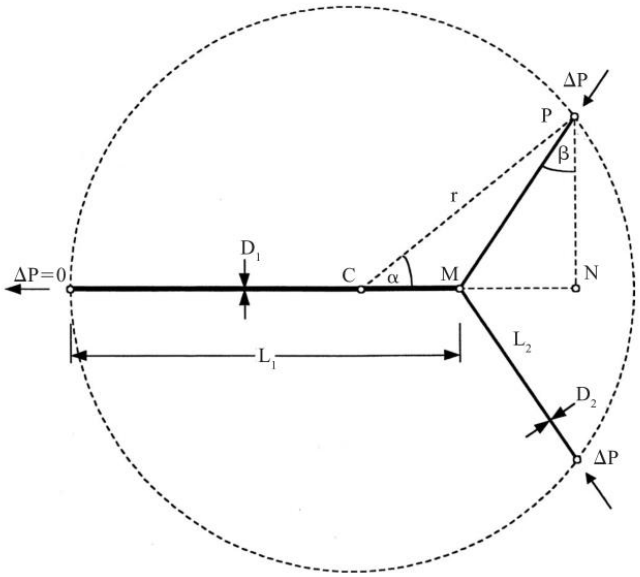

Figure 14. Y-shaped construct of round tubes

More recent work has shown that the 75 degrees angle appears as an optimized feature in much more complex tree-shaped flow architectures [25], and that it is nearly insensitive to the change from symmetric Y to asymmetric Y [26],[27]. This angle, like the Hess-Murray rule (1.4.1.11), provides a useful shortcut in the development of effective strategies to design equilibrium or near-equilibrium tree flow architectures [28].

1.4.1.1 Example

In this example Bejan [2] tech how to use the above principle for the purpose of sizing the terminal (smallest scales) ramifications of a bifurcated assembly of three flow channels (Figure 13) such that the flow volume occupied by the assembly packs maximum heat-transfer rate or mass-transfer rate. We are interested in the ratios D_1/D_2 and L_1/L_2. The first ratio follows from the minimization of pressure drop across the entire Y-shaped construct, subject to fixed total flow volume:

$$\frac{D_1}{D_2} = 2^{1/3} \qquad (1.4.1.1.1)$$

The ratio L_1/L_2 is determined from the observation that in all the tubes the boundary layers meet at the exit,

$$\delta_1 \sim \frac{D_1}{2} \quad \delta_2 \sim \frac{D_2}{2} \tag{1.4.1.1.2}$$

where δ_1 and δ_2 are the boundary layer thicknesses for laminar flow

$$\delta_1 = C\ L_1 Re_1^{-1/2} \quad \delta_2 = C\ L_2 Re_2^{-1/2} \tag{1.4.1.1.3}$$

with

$$Re_1 = \frac{U_1 L_1}{\nu} \quad Re_2 = \frac{U_2 L_2}{\nu} \tag{1.4.1.1.4}$$

The average velocities trough the mother tube (U_1) and daughter tube (U_2) are defined as

$$U_1 = \frac{\dot{m}_1}{\rho \frac{\pi}{4} D_1^2} \quad U_2 = \frac{\dot{m}_2}{\rho \frac{\pi}{4} D_2^2} \tag{1.4.1.1.5}$$

Dividing Eq.(1.4.1.1.3) and using Eq.(1.4.1.1.2), we obtain

$$\frac{D_1}{D_2} = \left(\frac{L_1}{L_2}\frac{U_2}{U_1}\right)^{1/2} \tag{1.4.1.1.6}$$

Next, we eliminate U_2/U_1 by using Eq.(1.4.1.1.5) and the assumption of symmetric bifurcations such that

$$\dot{m}_2 = \frac{1}{2}\dot{m}_1 \tag{1.4.1.1.7}$$

And Eq.(1.4.1.1.6) becomes independent of the ratio D_1/D_2;

$$\frac{L_1}{L_2} = 2 \tag{1.4.1.1.8}$$

In conclusion, for packing a maximum rate of transport (heat, mass) inside the flow volume, one must use rules (1.4.1.1.1) and (1.4.1.1.8), which, combined, read

$$\frac{L_1/D_1}{L_2/D_2} = 2^{2/3} \tag{1.4.1.1.9}$$

Another conclusion, then, is that the slenderness ratio L/D decreases in going toward smaller channels. These conclusion change somewhat if one accounts for the volume of the tissue that surrounds each tube and is penetrated by diffusion diffusion during the time L_1/U_1 and L_2/U_2, whether the Y configuration is asymmetric, and for whether

each channel has a flat (parallel-plate) cross-section instead of the round cross-section assumed here.

1.5 Vascularization of the Systems: the Key of Constructal Theory

The Constructal Theory aims to improve the performance of a system by seeking its vascularization. Zhihao et al. [29] studied the improvement in performance dictated by the different types of branches of a cooling circuit for microchips. In particular was studied the performance of the Y-shaped liquid cooling heat sink (YLCHS).

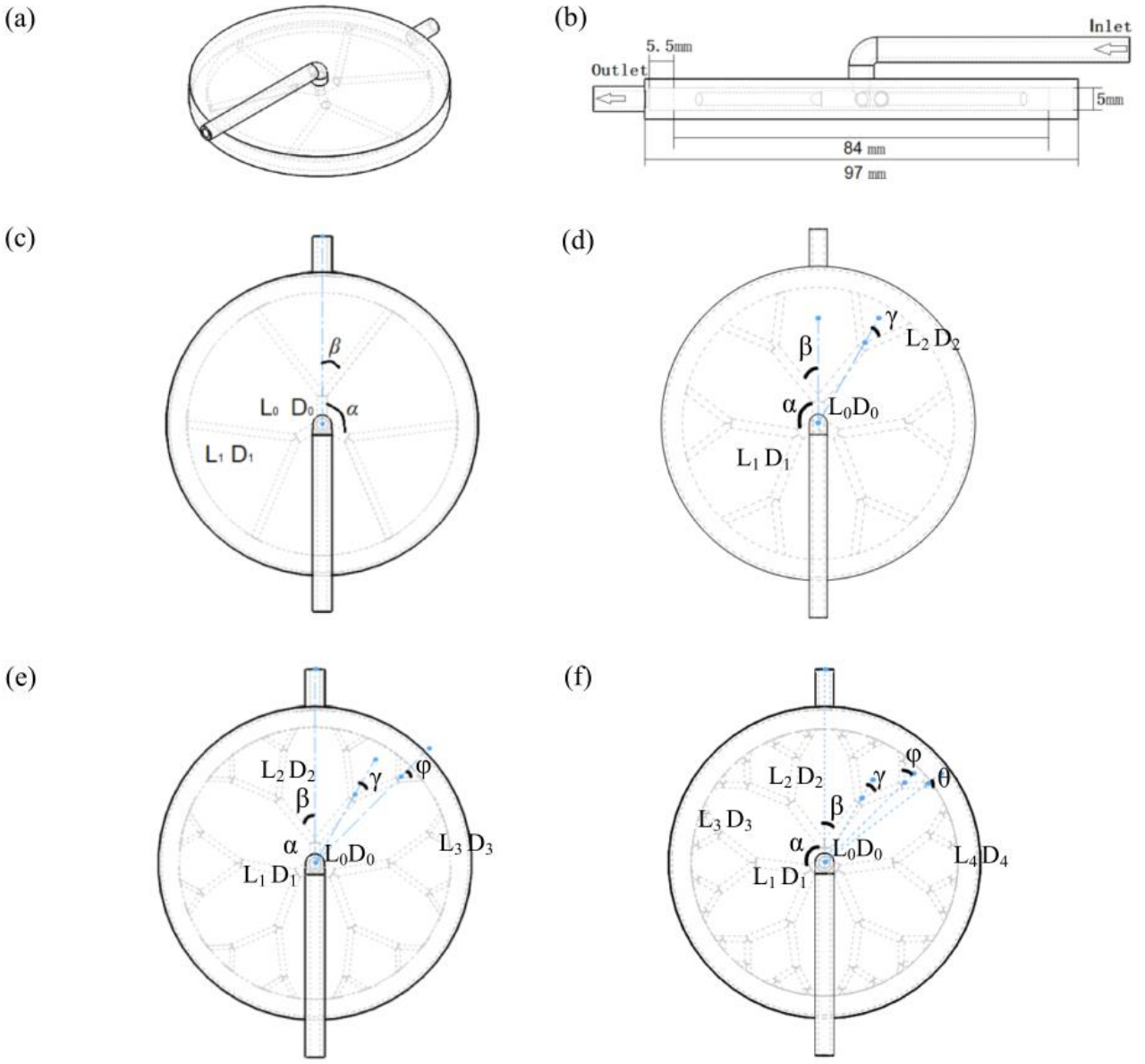

Figure 15. Sketch of proposed YLCHSs for different branching levels: (a) three-dimension view (n=1); (b) side view (n=1); (c) top view (n=1); (d) top view (n=2); (e) top view (n=3); (f) top view (n=4)

The maximum branching level has been determined as 4 accounted for the limited size of the heat sink because it is hard to fabricate the Y-shaped channels once

the branching level is higher than 4. The sketches of the proposed YLCHSs for different branching levels (i.e., 1 to 4) are shown in Figure 15.

As shown in Figure 15, the height and diameter of these heat sinks are set to 7 mm and 97 mm. The diameter of the outlet and inlet pipes is configured as 3.6 mm, and the lengths of the outlet and inlet pipes are 11.5 mm and 60 mm respectively. The height and width of the return flow ring are 5 mm and 5.5 mm. The thickness of the walls for heat sink (i.e., upper, lower, and surrounding) and pipes (i.e., inlet and outlet) are all 1 mm. The parameters for the channel deployment inside the proposed YLCHS can be calculated by:

$$\frac{D_{i+1}}{D_i} = 2^{-1/3} \tag{1.5.1}$$

$$L_i = \widehat{L_\iota}\, r \tag{1.5.2}$$

where D_i is the diameter of the i-th flow channel (i=0,1,2,3,4), L_i is the length of the i-th flow channel, $\widehat{L_\iota}$ is the dimensionless length of the i-th flow channel, and r is the radius of the circular area in which the Y-shaped network is located.

Then the dimensions of the channel deployment inside the YLCHS for different branching levels.

For the numerical simulation, three assumption was given: (1) the cooling water was considered as incompressible fluid; (2) the radiant heat transfer is ignored; and (3) the electronic chip and YLCHS was completely tightly fitted. The continuity, momentum, and energy balance equation were solved numerically.

1.5.1 Influence of the Branching level on the Temperature Distribution

The temperature distribution for the proposed YLCHSs can be seen in Figure 16. To clearly indicate the effect of branching level on the cooling performance, the peak surface temperatures for these heat sinks are presented in Figure 17. The heat exchange area of the YLCHSs is increased with the increasing branching level, resulting in a more uniform temperature distribution as well as a lower surface peak temperature of the Y-shaped network.

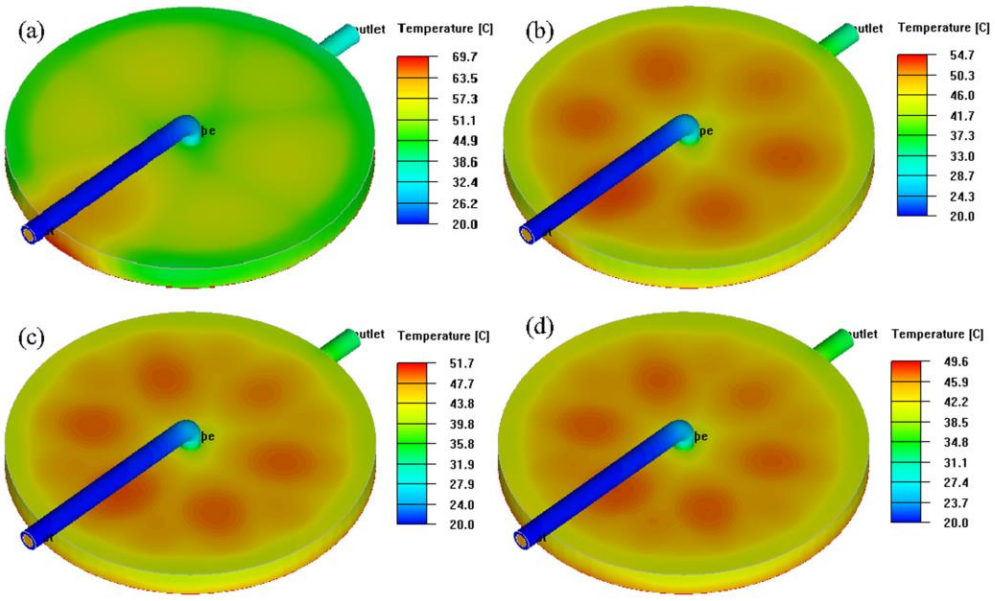

Figure 16. Comparison of temperature distribution for the heat sink. (a) n=1; (b) n=2; (c) n=3; (d) n=4.

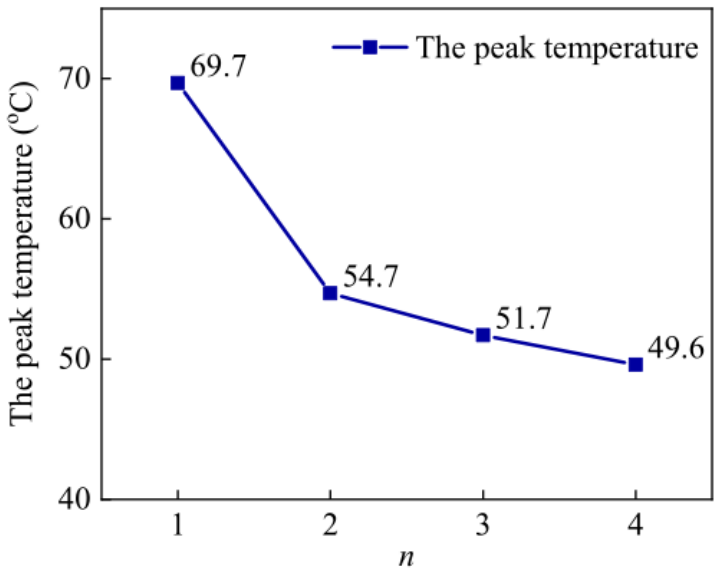

Figure 17. Peak temperatures for YLCHSs with different branching levels.

Although the peak temperature was decreased with the increasing of branching level, the reduction rate is decreased. As an example, the relationship between the branching level and the peak temperature can be regressed from Figure 17, which is given as:

$$T_p = 48.75 + 91.42 \cdot 0.26^n \quad (R^2 = 0.99) \qquad (1.5.1.1)$$

where T_p is the peak temperature of the YLCHS, and n is the branching level.

It can be seen from Eq.(1.5.1.1) that the peak temperature cannot be lower than 48.75 °C regardless of the branching level. From above, the peak temperature is 49.6 °C when branching level is 4. Thus, it can be predicted that the effect of branching level on the peak temperature is very small once the branching level is greater than 4 (e.g., The peak temperature is only reduced by about 0.12 °C when n is increased from 4 to 5.), which means that the branching level of 4 is preferable to improving the cooling performance of the YLCHSs.

1.5.2 Influence of the Branching level on the Pressure Loss

The pressure loss of the YLCHS also impacts on the performance of YLCHS because the flow resistance and associate pump power demand can be increased with the increasing of branching level. However, the pressure distribution under the four structures is almost identical, and their pressure losses are all about 4.4 kPa (Figure 18). Furthermore, the increase of pressure loss is lower than 0.04 kPa while the number of branching level is increased by one level. It is because the structures employed in this study are all developed based on the minimum flow resistance. Thus, the variation of pressure loss is very small, which is hardly influenced by the branching level.

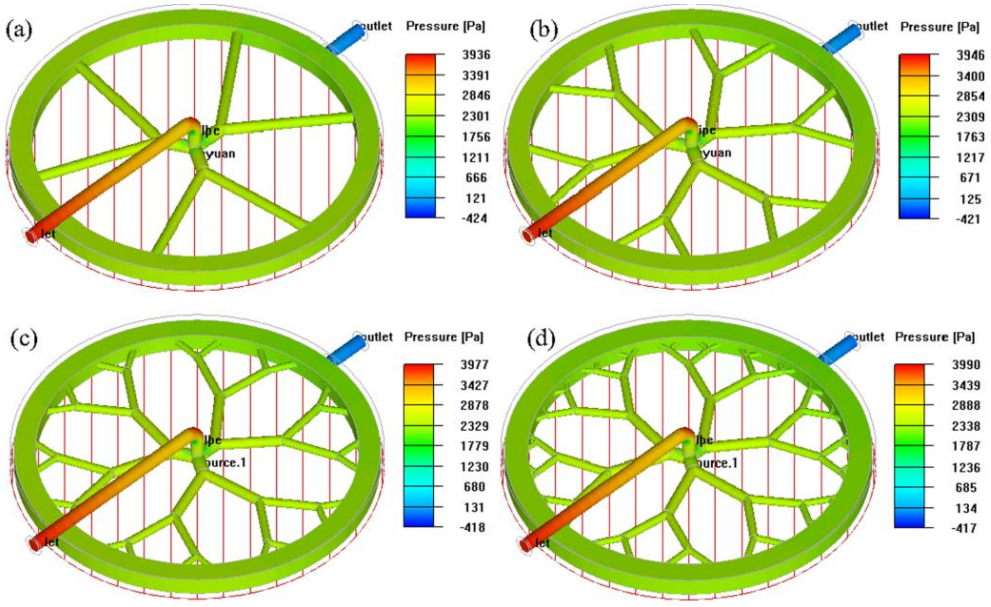

Figure 18. Pressure distribution in the channel of the heat sinks: (a) n = 1; (b) n = 2; (c) n = 3; (d) n = 4.

According to the calculated pressure loss in Figure 18, the pump power demands for these YLCHSs can be obtained by

$$N = \frac{\rho g Q H}{1000\,\eta} \tag{1.5.2.1}$$

where N is the pump power, ρ is the density of the medium, g is the gravitational acceleration, H is the head loss, Q is the volume flow rate, and η is the pump efficiency which is selected as 0.85 (the common value).

Accordingly, the branching level had little effect on the flow resistance and pump power demand for the proposed YLCHS. And only about 0.08 W of pump power demand is required to achieve the circulating of the cooling liquid from the inlet to the outlet for all kinds of branching level configuration. The smaller difference in the energy consumption of the pump can be ignored comparing with the significant improvement of the cooling performance.

1.6 Digression on Constructal Theory from the World of Science

Currently, not many academic people have considered the Constructal Theory as a valid approach to find the systems optimization. This is due to several factors including the relative youth of this theory.

Over the years, an increasing number of authors have published work in whose title the term "*Constructal Theory*" or "*Constructal Design*" appears.

Kuddusi et al. [30], and Ghodoossi [31], carried out studies to validate the Constructal Theory and concluded that increasing the complexity of the branching system does not necessarily improve its performance.

Ghodoossi [31] reviewed three basic constructal applications of Constructal Theory and showed that the expectation above is baseless. Thus, Ghodoossi [31] questioned the generality of constructal theory. However, later, a critique arose that the three unsuccessful applications are not sufficient means of evidence to question the generality of constructal theory. That is, constructal theory may fairly work well in applications other than the three reviewed by Ghodoossi [31].

The Kuddusi et al. [30] work is an attempt to clarify whether construction theory is successful in other applications or not. The work involves reviewing 14 different applications of construction theory involving tree-shaped flow networks. A constructive application could be successful if a decrease in flow resistance or, equivalently, an increase in flow performance with increasing branching is achieved. The review supported the conclusion of Ghodoossi [31]: "constructal theory will not necessarily improve the flow performance if the internal complexity of the flow area is increased … In contrast, the performance will mostly be lowered if the internal complexity of the flow area is increased."

Yenigun et al. [32] had conducted an experimental and numerical study in which a platelet suitable for cooling a microchip was considered. The system set-up is shown in Figure 19.

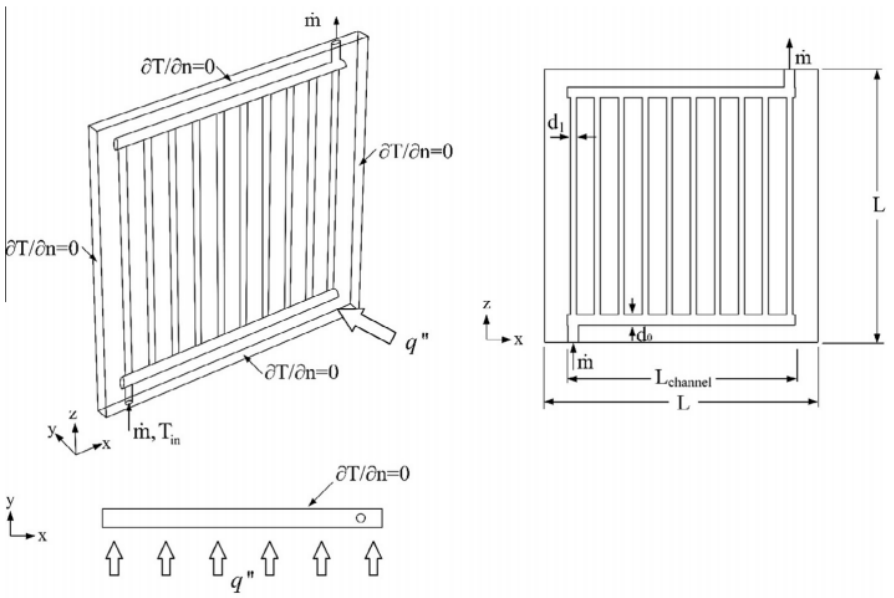

Figure 19. Geometry and boundary conditions of the vascularized plate with parallel cooling channels.

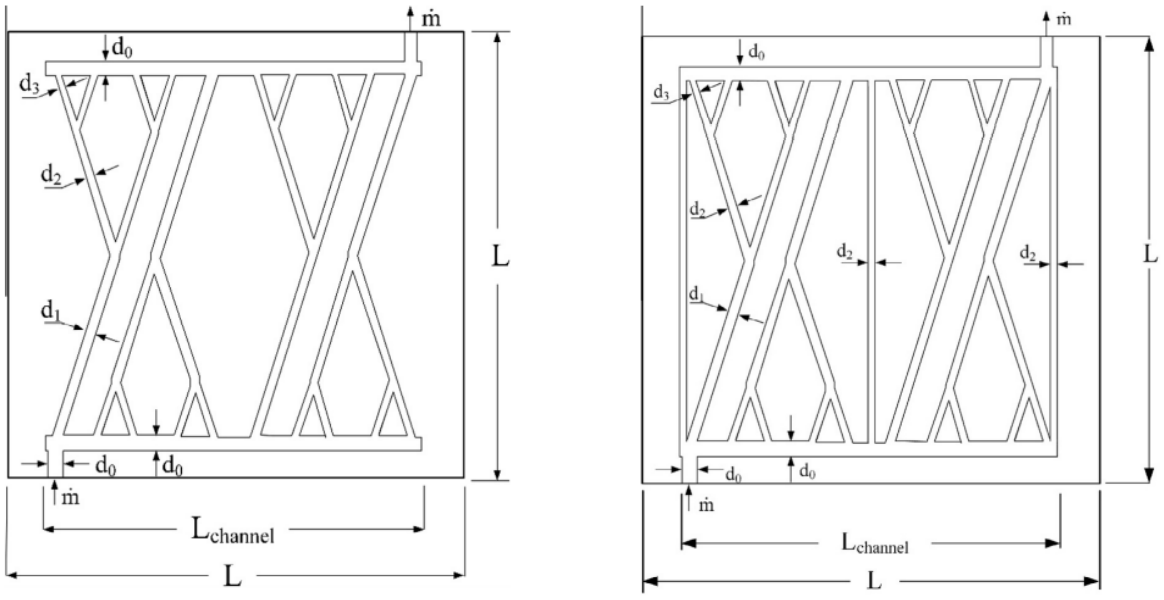

Figure 20. (Left) Tree-shaped design configuration; (Right) Hybrid design configuration.

The system of Figure 19 was compared with the two different systems obtained according to the rules of the Constructal Theory.

By solving the equations of thermo-fluid dynamics in stationary conditions, the results of Figure 21, Figure 22 and Figure 23 are obtained. The numerical results are compared to the experiments.

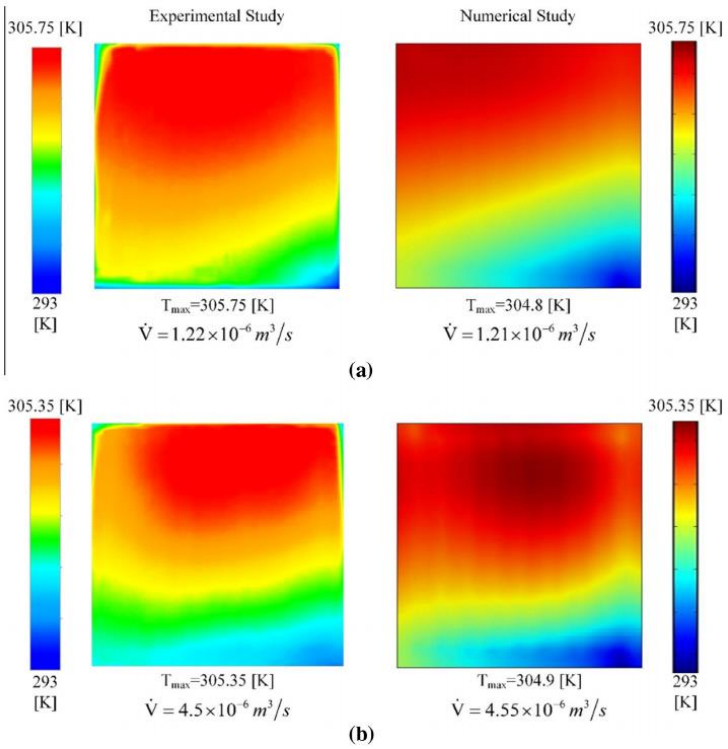

Figure 21. Temperature distributions of parallel channels design for experimental and numerical studies with (a) 50 W (b) 150 W of heat loads.

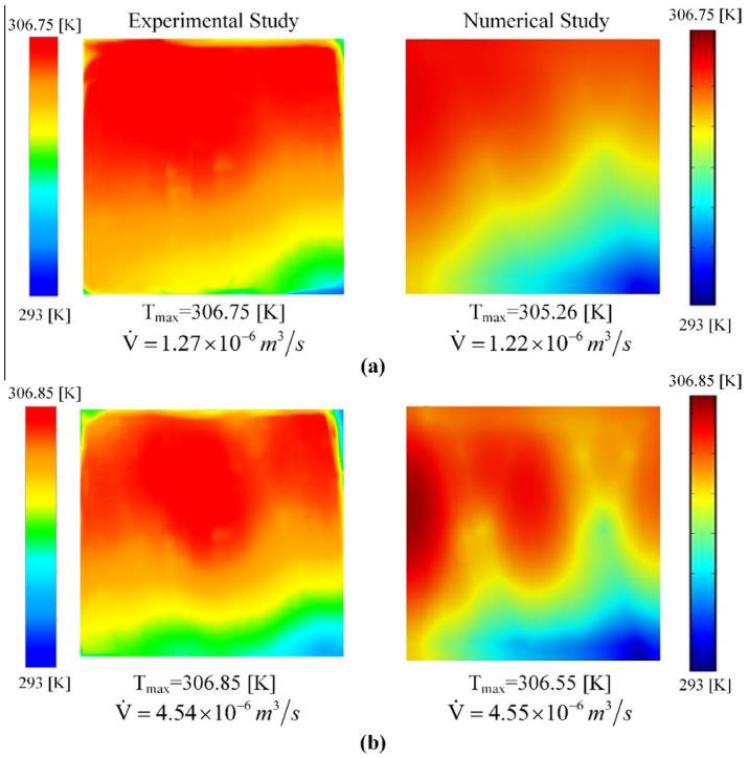

Figure 22. Temperature distribution of tree-shaped design for experimental and numerical studies with (a) 50 W (b) 150 W of heat loads.

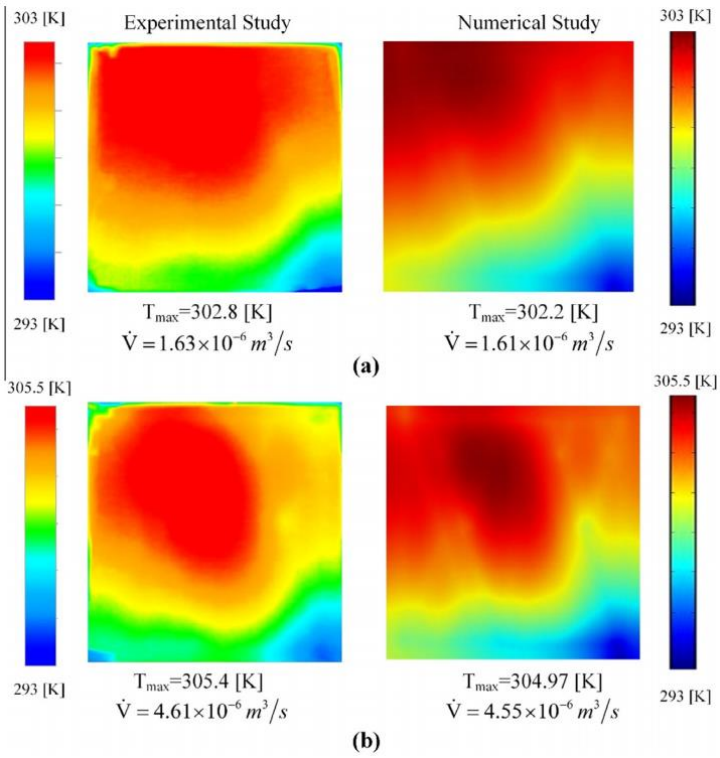

Figure 23. Temperature distribution of hybrid design for experimental and numerical studies with (a) 50 W (b) 150 W of heat loads.

The results show that the temperature distributions on the surface of the plate are not uniform in the case of the application of the tree shape. The best result remains that of parallel channels. Furthermore, in addition to the non-uniformity of the temperature, higher temperature peaks are reached with the Constructal Theory.

A further aspect concerns the pressure drops. Branches add local pressure drops and, consequently, the pressure drop is greater all other things being equal.

Attempting to optimize heat exchange through paths with lower flow resistance may be a good idea were it not for the fact that a smaller heat exchange surface is covered than in parallel channel geometry. Therefore, in this case, the application of the Constructal Theory has worsened the performance of the system.

2. Pulsatile Blood Flow

This chapter presents the problem of the motion of a fluid in pulsed regime inside a circular section duct, also called the "*Womersley problem*" or more general "*Pulsatile Flow Problem*" [33]. This result is important for modelling the velocity profile of the fluid inside a vein due to the pulsed motion regime induced by the pulsation of the heart. The mathematical nature of the Womersley function is somewhat complicated, furthermore its implementation in a fluid dynamics simulation code is not very easy. Therefore, in the second part of this chapter, a simplified method for the numerical implementation of the Womersley velocity profile was sought.

2.1 Pulsatile Flow Problem in a Circular Section Duct

Pulsatile flow implies that the pressure gradient varies periodically in time. This can mimic the blood flow in arteries. It is possible to idealize the problem and restrict the study to Newtonian fluid inside a tube with a rigid wall.

The Poiseuille profile is obtained by solving the Navier-Stokes equations and considering a constant pressure gradient. Therefore, considering an oscillation around this profile, the following pressure gradient can be defined:

$$-\frac{\partial P}{\partial z} = G_0(1 + \epsilon \sin(\omega t)) \tag{2.1.1}$$

where G_0 is the average time value of pressure drop, ε is the amplitude of the pressure wave, ω is the frequency of the pressure signal and t is the time.

Using cylindrical coordinates it is possible to consider better the symmetry of the problem:

$$u_z = u_z(r, t) \tag{2.1.2}$$

where u_z is the velocity along the tube axis z, r is the radius coordinate and t is the time. The focus is placed in case to the limit $t \to \infty$. In this case it is expected that the velocity

become periodic. Then, any periodic function can be expressed by a Fourier series. This justifies the use of $\sin(\omega t)$.

The starting point to analyse the problem is the equation of motion in cylindrical coordinates with the pressure gradient defined from Eq.(2.1.1):

$$\rho \frac{\partial u_z}{\partial t} = G_0(1 + \epsilon \sin(\omega t)) + \frac{\mu}{r}\frac{\partial}{\partial r}\left(r\frac{\partial u_z}{\partial r}\right) \tag{2.1.3}$$

Considering the characteristic dimensions:

$$u_{ch} = \frac{G_0\, R^2}{\mu} \tag{2.1.4}$$

$$l_{ch} = R \tag{2.1.5}$$

$$t_{ch} = \frac{R^2}{\nu} \tag{2.1.6}$$

the dimensionless variables can be written as

$$\tilde{u} = \frac{u}{u_{ch}} \tag{2.1.7}$$

$$\tilde{r} = \frac{r}{l_{ch}} \tag{2.1.8}$$

$$\tilde{t} = \frac{t}{t_{ch}} \tag{2.1.9}$$

Substituting Eqs.(2.1.4)-(2.1.6) into Eq.(2.1.3) and using Eqs.(2.1.7)-(2.1.9) the non-dimensional motion equation arise (for sake of clarity the tilde symbol was ignored)

$$\frac{\partial u}{\partial t} = (1 + \epsilon \sin(R_\omega t)) + \frac{1}{r}\frac{\partial}{\partial r}\left(r\frac{\partial u}{\partial r}\right) \tag{2.1.10}$$

where $R_\omega = R^2\omega/\nu$ is the ratio of the time scale and ε is the amplitude of periodic component.

The boundary conditions for this problem are

$$r = 1, \qquad u = 0 \tag{2.1.11}$$

$$r = 0, \qquad u = fixed \tag{2.1.12}$$

$$t = 0, \qquad u = 0 \tag{2.1.13}$$

Therefore, the non-dimensional problem of pulsatile flow in a circular section duct is formulated from Eq.(2.1.10) to Eq.(2.1.13).

It is important to note that the problem just formulated is linear and the pressure gradient comes into play as two-part source therm. This means that defining the velocity as

$$u = u_0 + \epsilon\, u_1 \tag{2.1.14}$$

the problem is split in two

$$\begin{cases} \dfrac{\partial u_0}{\partial t} = 1 + \dfrac{1}{r}\dfrac{\partial}{\partial r}\left(r\dfrac{\partial u_0}{\partial r}\right) \\ r = 1, \quad u_0 = 0 \\ r = 0, \quad u_0 = fixed \\ t = 0, \quad u_0 = 0 \end{cases} \tag{2.1.15}$$

and

$$\begin{cases} \dfrac{\partial u_1}{\partial t} = \sin(R_\omega t) + \dfrac{1}{r}\dfrac{\partial}{\partial r}\left(r\dfrac{\partial u_1}{\partial r}\right) \\ r = 1, \quad u_1 = 0 \\ r = 0, \quad u_1 = fixed \\ t = 0, \quad u_1 = 0 \end{cases} \tag{2.1.16}$$

u_o is independent of *t*, then the solution of system (2.1.15) is a parabolic profile.

For the system (2.1.16) arise an important question: is velocity in phase with pressure drop? If the answer is positive, it is possible to define

$$u_1 = \sin(R_\omega t)\, f(r) \tag{2.1.17}$$

Substituting Eq.(2.1.17) in Eq.(2.1.16) we get

$$R_\omega \cos\big((R_\omega t)\, f(r)\big) = \sin(R_\omega t) + \frac{1}{r}\frac{\partial}{\partial r}\left(r\frac{\partial f}{\partial r}\right)\sin(R_\omega t\,) \tag{2.1.18}$$

In general, there is going to be a phase difference between velocity and pressure drop. Since $\sin(\omega t)$ does not occur in all time (Eq.(2.1.17)). If $R_\omega \ll 1$ the velocity unlikely to be in phase. Remembering then

$$e^{i\,R_\omega t} = \cos(R_\omega t) + i\sin(R_\omega t) \tag{2.1.19}$$

Eq.(2.1.18) can be rewritten in form

$$\frac{\partial u_1^*}{\partial t} = e^{i\,R_\omega t} + \frac{1}{r}\frac{\partial}{\partial r}\left(r\frac{\partial u_1^*}{\partial r}\right) \tag{2.1.20}$$

where

$$u_1 = I(u_1^*) \tag{2.1.21}$$

want to search for the function

$$u_1^* = e^{i\,R_\omega t}\,H(r) \tag{2.1.22}$$

Substituting Eq.(2.1.22) into Eq.(2.1.20) the new problem is obtained

$$\begin{cases} \frac{1}{r}\frac{d}{dr}\left(r\frac{dH}{dr}\right) - i\,R_\omega H = -1 \\ H(r=0) = fixed \\ H(r=1) = 0 \end{cases} \tag{2.1.23}$$

The solution of the problem (2.1.23) is composed of a particular solution and a homogeneous solution:

$$H = H_p + H_h \tag{2.1.24}$$

$$H_p = \frac{1}{i\,R_\omega} = -\frac{i}{R_\omega} \tag{2.1.25}$$

For finding H_h we have to sole

$$\frac{1}{r}\frac{d}{dr}\left(r\frac{dH_h}{dr}\right) - i\,R_\omega H_h = 0 \tag{2.1.26}$$

Definie

$$r^2(-i\,R_\omega) = r^{*2} \tag{2.1.27}$$

$$r = r^*\left(\frac{i}{R_\omega}\right)^{1/2} \tag{2.1.28}$$

Eq.(2.1.26) becomes

$$\frac{1}{r^*}\frac{d}{dr^*}\left(r^*\frac{dH_h}{dr^*}\right) - H_h = 0 \tag{2.1.29}$$

The solution of Eq.(2.1.29) is

$$H_h = A\,J_0(r^*) + B\,Y_0(r^*) \tag{2.1.30}$$

But $Y_0(r^*=0)$ is unbounded, then B=0. However

$$H_h = A\,J_0(r^*) \tag{2.1.31}$$

Then Eq.(2.1.23) becomes

$$H = -\frac{i}{R_\omega} + A\,J_0\left(\sqrt{\frac{R_\omega}{i}}\;\; r\right) \tag{2.1.32}$$

For

$$H(r=1) = 0, \qquad A = \frac{i}{R_\omega}\frac{1}{J_0\left(\sqrt{\frac{R_\omega}{i}}\right)} \tag{2.1.33}$$

However

$$H(r) = \frac{i}{R_\omega}\left[1 - \frac{J_0\left(\sqrt{\frac{R_\omega}{i}}\; r\right)}{J_0\left(\sqrt{\frac{R_\omega}{i}}\right)}\right] \tag{2.1.34}$$

$$u_1 = I\left(e^{i\,R_\omega t}\,H(r)\right) \tag{2.1.35}$$

Recall Eq.(2.1.14) the solution is

$$u = u_0 + u_1 = u_0 + I\left(e^{i\,R_\omega t}\,H(r)\right) \tag{2.1.36}$$

2.2 Approximation of Womersley Velocity Profile

The complexity of the numerical language required for the implementation of the Womersley profile has paved the way for finding an easier scheme to write such function.

The work [34] entitled "*A Simple Transient Poiseuille-Based Approach to Mimic the Womersley Function and to Model Pulsatile Blood Flow*" was the result of the search for an approximation of the Womersley function through the Poiseuille parabolic profile.

Several authors (i.e., [35]) adapt the Womersley function to the measured pulsed flow by writing the following function:

$$v_W\left(\frac{2r}{D},t\right)=\Re\left\{Wo\sqrt{i^3}\left[\frac{J_0\left(Wo\sqrt{i^3}\,\frac{2r}{D}\right)-J_0\left(Wo\sqrt{i^3}\,\right)}{2\,J_0\left(Wo\sqrt{i^3}\right)-Wo\sqrt{i^3}\,J_0\left(Wo\sqrt{i^3}\right)}\right]\frac{Q(t)}{Q_0}\right\} \qquad (2.2.1)$$

where $R\{\cdot\}$ denotes the real part of the function defined in the complex plane, $i = (-1)^{0.5}$ is the imaginary unit, $J_0(.)$ is the zero order modified Bessel function, (2r/D) is the dimensionless variable in which D is the tube diameter, r is the distance from the tube centreline, $Wo=0.5D(\omega\rho/\eta)^{0.5}$ represents the Womersley number in which $\omega = 2\pi/T$ is the angular frequency determined from characteristic period T, ρ is the fluid density, η is the dynamic viscosity, Q(t) is the flow rate variable in time, and Q_0 is the average flow rate.

If the inlet pressure difference is kept constant, the result is the Poiseuille velocity profile, illustrated in [36]:

$$v_P\left(\frac{2r}{D}\right)=\gamma\left[1-\left(\frac{2r}{D}\right)^2\right] \qquad (2.2.2)$$

where γ denotes the non-dimensional amplitude.

Finally, it is worth mentioning that both velocity profiles refer to laminar and steady-state flow conditions.

The Womersley velocity profile (Eq.(2.2.1)) is a function of r and t, while the Poiseuille velocity profile (Eq.(2.2.2)) is a function of r. In order to compare the mentioned two curves, the Womersley profile was considered in the following version:

$$v_W\left(\frac{2r}{D}\right) = f\left(\frac{2r}{D}\right) g(t) \tag{2.2.3}$$

where the function f(2r/D) is composed from the real part of Eq.(2.2.1) and g(t) is equal to R(Q(t)/Q0) (the remaining term of Eq.(2.2.1)). In this modality, it is now possible to compare Eq.(2.2.2) with the function f(2r/D) defined in Eq.(2.2.3).

Therefore, the problem is now represented by the equivalence:

$$\Re\left\{Wo\sqrt{i^3}\left[\frac{J_0\left(Wo\sqrt{i^3}\,\frac{2r}{D}\right) - J_0\left(Wo\sqrt{i^3}\,\right)}{2\,J_0\left(Wo\sqrt{i^3}\right) - Wo\sqrt{i^3}\,J_0\left(Wo\sqrt{i^3}\right)}\right]\right\} = \gamma\left[1 - \left(\frac{2r}{D}\right)^2\right] \tag{2.2.4}$$

γ denotes the unknown variable, which will be a function of (2R/D). From Eq.(2.2.4), the following calculation is obtained:

$$\gamma\left(\frac{2r}{D}\right) = \frac{\Re\left\{Wo\sqrt{i^3}\left[\frac{J_0\left(Wo\sqrt{i^3}\,\frac{2r}{D}\right) - J_0\left(Wo\sqrt{i^3}\,\right)}{2\,J_0\left(Wo\sqrt{i^3}\right) - Wo\sqrt{i^3}\,J_0\left(Wo\sqrt{i^3}\right)}\right]\right\}}{\left[1 - \left(\frac{2r}{D}\right)^2\right]} \tag{2.2.5}$$

In order to validate the approach pointed out here, typical values of the blood flow inside an artery were considered (data are taken from Vimmr et al. [33]): D = 0.003 m, blood density ρ = 1060 kg/m3 , blood dynamic viscosity $\eta = 3.45 \times 10^{-3}$ Pa s and cardiac cycle period T = 1.68 s.

The plot of Eq.(2.2.5) is represented in Figure 24 together with the average value of this calculated according to the formula:

$$M\left(\gamma\left(\frac{2r}{D}\right), [a, b]\right) = \frac{1}{b-a}\int_a^b \gamma\left(\frac{2r}{D}\right)\, d\left(\frac{2r}{D}\right) \tag{2.2.6}$$

where [a, b] = [0, 1] is the integral range. The average value M of Eq.(2.2.6) is equal to 1.99923.

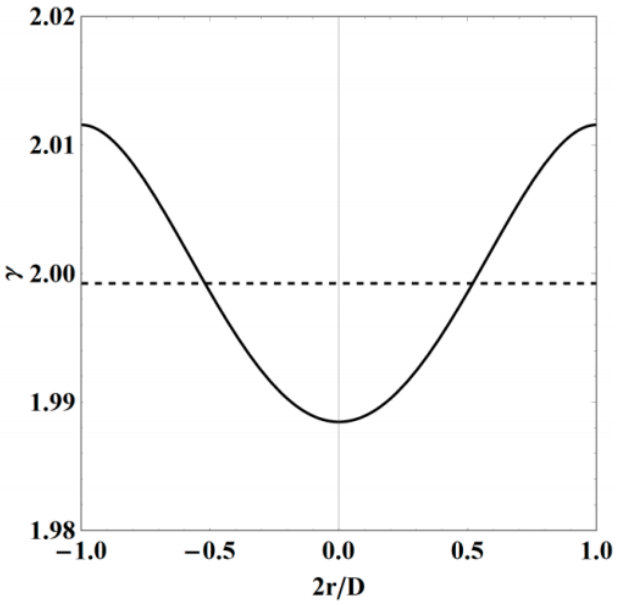

Figure 24. γ function (continuous line) and its average value 1.99923 (dashed line). Plot considering the example values: ρ = 1060 kg/m3, η = 3.45 × 10^{-3} Pa s, D = 0.003 m, T=1.68 s and Wo=1.61. [Ref. 7.3]

The calculated γ average value can be used as an approximate amplitude value in the Poiseuille Eq.(2.2.2). Therefore, the function R{.} has been approximated in a transient Poiseuille velocity profile. For the sake of clarity, the "transient" Poiseuille velocity profile has been referred to as the Poiseuille velocity profile multiplied by the function that adjusts the amplitude over time; that is, the following equation is intended:

$$v_P\left(\frac{2r}{D},t\right)=\gamma\left[1-\left(\frac{2r}{D}\right)^2\right]g(t) \tag{2.2.7}$$

where g(t) is defined in Eq.(2.2.3).

What varies during the transient flow is, therefore, the function g(t), which has an influence on the width of the profile.

The relative percentage error is evaluated according to the relation:

$$\epsilon\% = \frac{\left|f\left(\frac{2r}{D}\right)-v_P\left(\frac{2r}{D}\right)\right|}{f\left(\frac{2r}{D}\right)}100 \tag{2.2.8}$$

Figure 25 shows the comparison between function f(2r/D) and v_P(2r/D) and the corresponding percentage error along the dimensionless axis. In addition, all the

corresponding numerical values have been reported in Table 1. The maximum approximation error is slightly greater than 0.60% in the boundary points. This discrepancy validates the calculation approach developed here.

The Womersley number Wo, defined in Eq.(2.2.1), is a very important parameter that affects the validity of the approximation explained above. As shown in Figure 26, as the Womersley number increases, the behavior of the Womersley function moves further and further away from the parabolic profile.

Due to this, the approximation of the Womersley profile with the Poiseuille profile is valid for little values of the Womersley number Wo (Wo < 2).

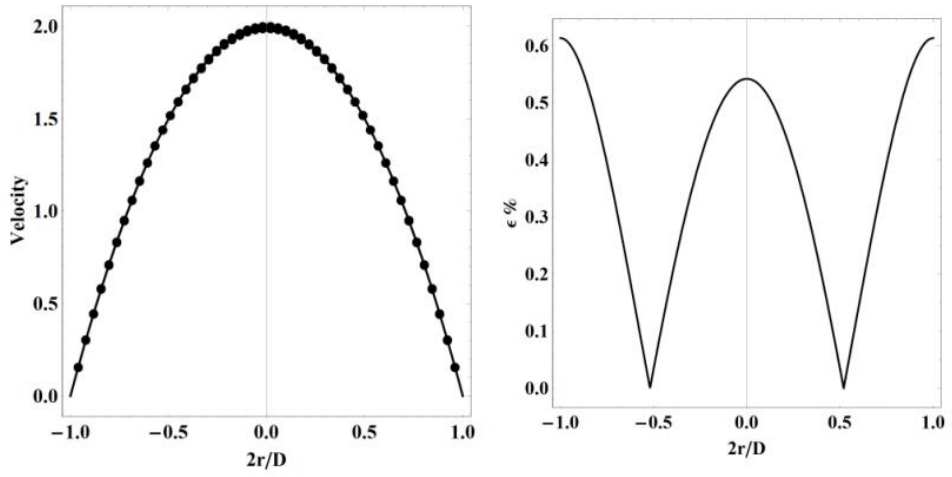

Figure 25. Comparison between the Womersley profile (line) and the transient Poiseuille profile (dot). Non-dimensional velocity comparison (left); percentage error (right). Plot considering the example value: ρ = 1060 kg/m3, η = 3.45 × 10^{-3} Pa s, D = 0.003 m, T=1.68 s and Wo=1.61. [Ref. 7.3]

Table 1. Numerical value of the Womersley f(2r/D) profile and Poiseuille profile considering the example values: ρ = 1060 kg/m3, η = 3.45 × 10^{-3} Pa s, D = 0.003 m, T = 1.68 s, and Wo = 1.61. [Ref. 7.3]

2r/D	*f(2r/D)*	v_P*(2r/D)*	ε%	*2r/D*	*f(2r/D)*	v_P*(2r/D)*	ε%
0.00	1.98845	1.99923	0.542061	0.55	1.39521	1.39446	0.053681
0.05	1.98360	1.99423	0.536241	0.60	1.28133	1.27951	0.142441
0.10	1.96902	1.97924	0.518870	0.65	1.15722	1.15456	0.230149
0.15	1.94472	1.95425	0.490221	0.70	1.02283	1.01961	0.314656
0.20	1.91065	1.91926	0.450745	0.75	0.87812	0.87466	0.393649
0.25	1.86679	1.87428	0.401073	0.80	0.72308	0.71972	0.464652
0.30	1.81310	1.81930	0.342012	0.85	0.55772	0.55479	0.525025
0.35	1.74952	1.75433	0.274547	0.90	0.38204	0.37985	0.571956
0.40	1.67601	1.67936	0.199834	0.95	0.19611	0.19493	0.602458
0.45	1.59249	1.59439	0.119200	1.00	0.00000	0.00000	-
0.50	1.49891	1.49942	0.034141				

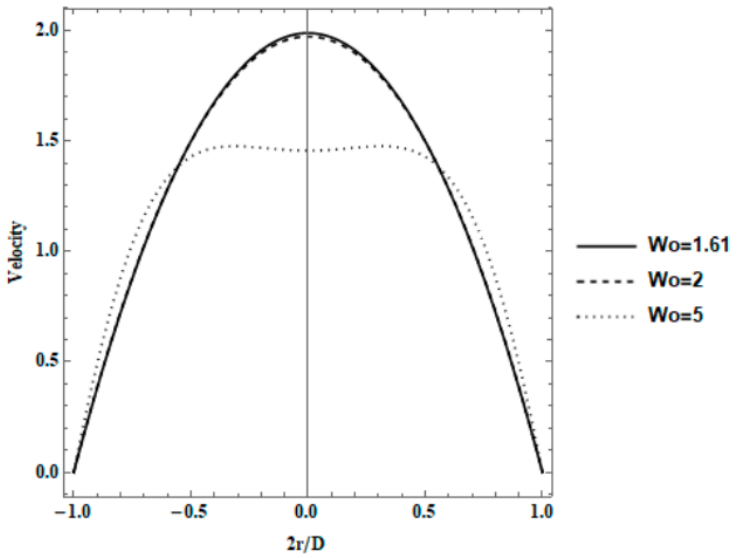

Figure 26. Different shape of thre Womersley function due to the different Womersley number varies. [Ref. 7.3]

It is worth mentioning that the limit of this approximation mainly relays on the neglection of possible flow inversions. More specifically, the above-mentioned approximation is valid for code implementation, when an input flow value is imposed or a fully developed parabolic velocity profile is considered, provided that Wo < 2.

In the work of Impiombato et al. [34], in addition to the treatment of the problem exposed, it was a numerical case found for the verification of the approximation just discovered.

Appendix A shows how the time-dependent inlet flow rate Q(t) was approximated through the Fourier series function.

Figure 27 shows the velocity comparison between the Womersley velocity profile (shown in solid line) and the Poiseuille function profile (indicated with dots) in different sections (denoted with A, B, C, D and E) for different times relating to the cardiac cycle. Based on pure observation, the results clearly show that there is no evident difference between the two studied velocity profiles.

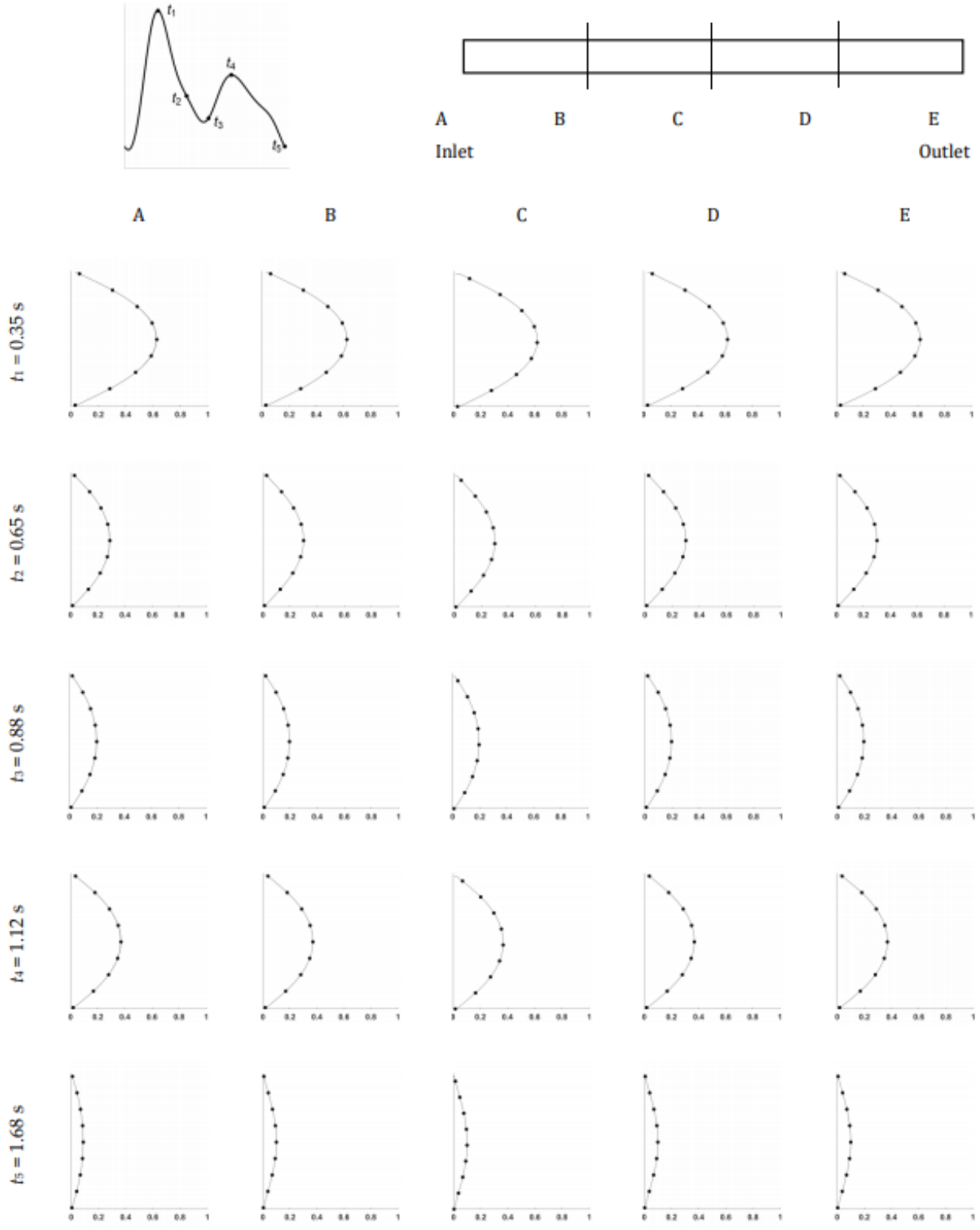

Figure 27. Comparison between the original Womersley profile (line) and the transient Poiseuille function profile (dot) using several times in different sections. The velocity was considerend in m/s. [Ref. 7.3]

3. Optimization of a Cardiac Bypass Graft by Constructal Design

Bypass grafts are used to promote blood flow impaired by partial obstruction (stenosis) of arteries by fat accumulation. The computational modelling of this type of system is used to understand the flow characteristics and to look for reasons and solutions for postoperative failures. The present work deals with the effects of changes in geometry in the performance of a system consisting of an idealized partially obstructed artery and a bypass graft. The Constructal Design Method has been employed in previous works in the analysis of such system assuming steady-state flow. In the present work, blood flow is modelled as transient and pulsatile. The Constructal Design Method is used to determine the performance indicator (dimensionless pressure drop), constraints (system volume and stenosis degrees – 50% and 75%) and degrees of freedom: junction angle ($30^o \leq \alpha \leq 70^o$) and diameter ratio ($0.5 \leq D1/D \leq 1$). The Response Surface Methodology was used to evaluate the conditions of minimum pressure drop in transient conditions. As the junction angle decreased to 30^o, and the diameter ratio increased to 1, the pressure drop decreased, and there was a considerable dependence of pressure drop on the stenosis degree. The effects of the diameter ratio were more pronounced than those of the junction angle. A resistance model based on an analogy with an electronic circuit was introduced, resulting in a correlation for the pressure drop due to the bypass. This correlation confirmed that the point (α, $D1/D$)=(30°,1) is a point of minimization of flow resistance. The application of the Constructal Design method in hemodynamic might be an excellent alternative to

configuring enhanced performance and providing valuable results to the understanding of biological flows

3.1 Introduction

According to T.J. Pedley et al [37], atherosclerosis and diseases of the blood circulatory system cause more than half of the deaths in today's western society. Atherosclerosis is the phenomenon characterized by the deposit of material in the artery wall, which in turn leads to inflammation. When the lumen of the blood vessels narrows, health is in serious danger: being the narrowest passage, the quantity of blood that can flow inside them is less; consequently, the supply of oxygen and nutrients to tissues and organs (including the heart) can be severely compromised. The consequences can be just as serious and include heart attacks and strokes, sometimes fatal. The accumulation of fat in the arteries walls can block the flow of blood partly or entirely and causes atherosclerosis, which consists of stiffening the walls of these vessels (KU et al. [38]). As explained by Tian et al. [39], and Liu et al. [40], this abnormal accumulation is commonly designated as stenosis. Patients under these conditions can lose the quality of life due to the loss of oxygenation of organs, tissues, or the brain and are at risk for heart attacks or strokes. According to Guerciotti et al. [41], effective therapy for high-risk patients is coronary artery bypass graft (CABG) surgery, which consists of bypassing a stenotic region to restore the proper blood flow to the heart. Bassiouny et al. [42] points that the main cause for the CABG surgery failure is intimal hyperplasia (IH) – an abnormal proliferation of smooth muscle cells that is mainly observed between the graft and the coronary artery, resulting in the reduction of the lumen of the graft and leading to restenosis and graft occlusion (BASSIOUNY et al. [42]). As reviewed by Dutra et al. [43], several authors have investigated the correlation between the blood flow dynamics in CABGs and the developing of IH. Some authors have used a three-dimensional numerical model to investigate the effects on blood flow caused by different locations of the stenosis (Bertolotti and Deplano [44]; Ko et al. [45]), Reynolds number (Lee et al. [46]; Chua

et al. [47]), graft diameter (Fan et al. [48]), junction angles (Lee et al. [46]; Ko et al. [49]), fluid deflector (Roos et al. [50]) and compliance mismatch (Post et al. [51]). Other studies applied optimization methods to predict the best geometry of the graft according to the diameter of the artery and graft (Chua et al. [47]; Xiong and Chong, [52]; Do et al. [53]; Vimmr et al. [35]), junction angle and stenosis degree (Vimmr et al. [47]). Tiwari et al. [54], using an analytical two-fluid model, investigated the role of rheology on blood flow through constricted vessels. They addressed the importance of the accurate modeling for blood flow, stressing the impact of blood and flow modeling in parameters such as flow rate and flow resistance, which are crucial in the treatment of many diseases.

Recently, Dutra et al. [43] investigated the design of bypass grafts circumventing idealized stenosed coronary arteries using the Constructal Design Method (Rocha et al. [3]) and a Computational Fluid Dynamics (CFD) model. Their model assumed the steady-state flow of blood, modeled as a Newtonian fluid. The response surfaces for pressure drop as a function of geometric parameters showed that the highest diameter ratios between graft and artery, and the lowest junction angles promoted the lowest resistance to flow, consisting in the optimal geometry in the context of the Constructal Design Method.

The Constructal Design Method is a method of geometry design and analysis conceived in the framework of the Constructal Theory, established by Adrian Bejan from 1996 and summarized by the Constructal Law: “for a finite-size flow system to persist in time (to live) it must evolve with freedom in such a way that it provides easier access to imposed currents that that flow through it” (Bejan [55]). The Constructal Theory literature has shown in the past few years, that evolution in nature follows this principle (Bejan and Zane [56]; Bejan [5]). Constructal Design is the philosophy of evolutionary design in engineering applications (Rocha et al. [5]). It may be employed to assess the effect of geometric parameters on the performance of flowing systems by identifying the purpose of these systems and the flowing currents (Rocha et al. [3]). The first applications of Constructal Theory in medicine were within the field of cancer

treatments, as studied by Wang et al. [16], and Lucia and Grisolia [57], and vision, in two papers by Lucia et al. [58] and [57].

This work goes more in-depth in the investigation of the steady-state bypass graft explored by Dutra et al. [3]. The present study investigates numerically, using CFD, the Constructal Design of the bypass graft circumventing a stenosed artery subjected to pulsatile blood flow. The system of analysis consists of the set artery-graft. The geometry performance parameter is the time average pressure drop. The constraint is the system volume and the degrees of freedom for the system to morph and improve its performance are the diameter ratio and the junction angle between graft and artery. The Constructal Design Method, with the aid of Response Surfaces, allows to explore the effects of the degrees of freedom on flow performance. As the bypass geometry is known to significantly affect the blood flow field and play an essential role in potential graft failure due to intimal hyperplasia, this work intends to bring valuable results to the understanding of biological problems.

3.2 Methodology

3.2.1 Constructal Design

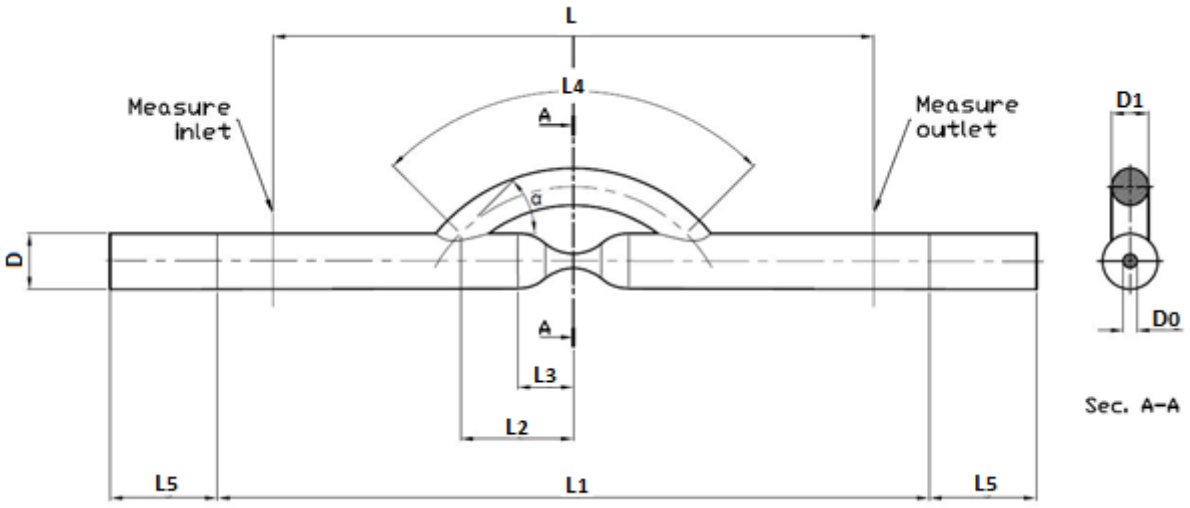

Figure 28. Problem domain. [Ref. 7.4]

The computational geometry of an idealized bypass with obstruction is shown in Figure 28. The main artery is represented with a diameter equal to D and length equal

to L_1. The main tube undergoes stenosis that reduces it to diameter D_0. The geometry is symmetric over the center of the stenosis in the axial direction. The graft is placed at a distance L_2 from the center of the stenosis, and its diameter is denoted D_1. The junction angle is α. L_3 is the distance from the center where the stenosis begins.

The problem consists of a pulse of blood flow, which enters the domain at the tube inlet, as described in Appendix A. Depending on flow conditions and geometry configuration, the flow is partially deviated through the bypass. It is assumed that the tube walls are rigid, impermeable, and non-slip. The flow is also assumed to be three-dimensional, incompressible, and laminar.

To obtain a fully developed flow, it is built the computational model for the geometry depicted in Figure 28 with main tube extensions of 25 diameters upstream and downstream (L_5=25.D). At the inlet patch, it was imposed a pulsatile velocity profile. At the outlet patch, it was imposed pressure outlet as boundary conditions. The host artery diameter, D, was fixed to 3 mm for all simulations. This diameter was corresponding to an average value of the right coronary artery (Bertolotti et al. [44]).

Since the stenosis is usually formed by material deposition, it is considered the main tube volume as its external volume is not narrowed:

$$V = \pi \frac{D^2}{4} (L_1 + L_5) \tag{3.2.1.1}$$

where V is the total artery volume, D is the artery diameter, and (L_1+L_5) is the total artery length. The graft volume is

$$V = \pi \frac{D_1^2}{4} L_4 \tag{3.2.1.2}$$

where V_1 is the total graft volume, D_1 is the graft diameter, and L_4 is the total graft length. The process of finding the optimal condition aims to find the value of V_1, that is, the product between D_1^2 and L_4, keeping constant V.

The stenosis degree is calculated as

$$S = \frac{D - D_0}{D} 100\% \tag{3.2.1.3}$$

where S is the stenosis degree, and D_0 is the diameter at the center of the stenosis.

It is defined as constants the ratios L_1/D, L_2/D, and L_3/D and employed the geometric parameters as detailed in Table 2. A baseline case from the literature (Vimmr et al. [44]) was used to define these values.

Table 2 Geometric parameters for artery and graft build up. [Ref. 7.4]

Parameters	Values
L_1/D	16.67
L_2/D	2.5
L_3/D	1

Two values of stenosis degree have been evaluated: S = 50% and S = 75%. Blood is modeled as an incompressible Newtonian fluid with mass density, ρ=1000 kg/m³, and dynamic viscosity, μ=0.0035 Pa.s (Ko et al. [45]). The assumption of blood as Newtonian fluid is a consent already used by other studies in the hemodynamic area) Vimmr et al. [45].

Constructal Theory assumes that living systems evolve limited by space (Rocha et al. [45]. According to Constructal Theory systems must evolve to provide easier access to its flows (Bejan and Lorente [13]), it was considered that the dimensionless pressure drop along the length L, $\tilde{p}$, should be as low as possible. Thus, the effects of the degrees of freedom diameter ratio, D_1/D, and junction angle, α., on the dimensionless pressure drop were investigated in this Constructal Design application. The ranges investigated comprised of $D_1 \leq D$ and $30^o \leq \alpha \leq 70^o$. It was searched for the diameter ratio, D_1/D, and junction angle, α, that minimize the value of the pressure drop. Figure 29 details all the steps required by the Constructal Design methodology.

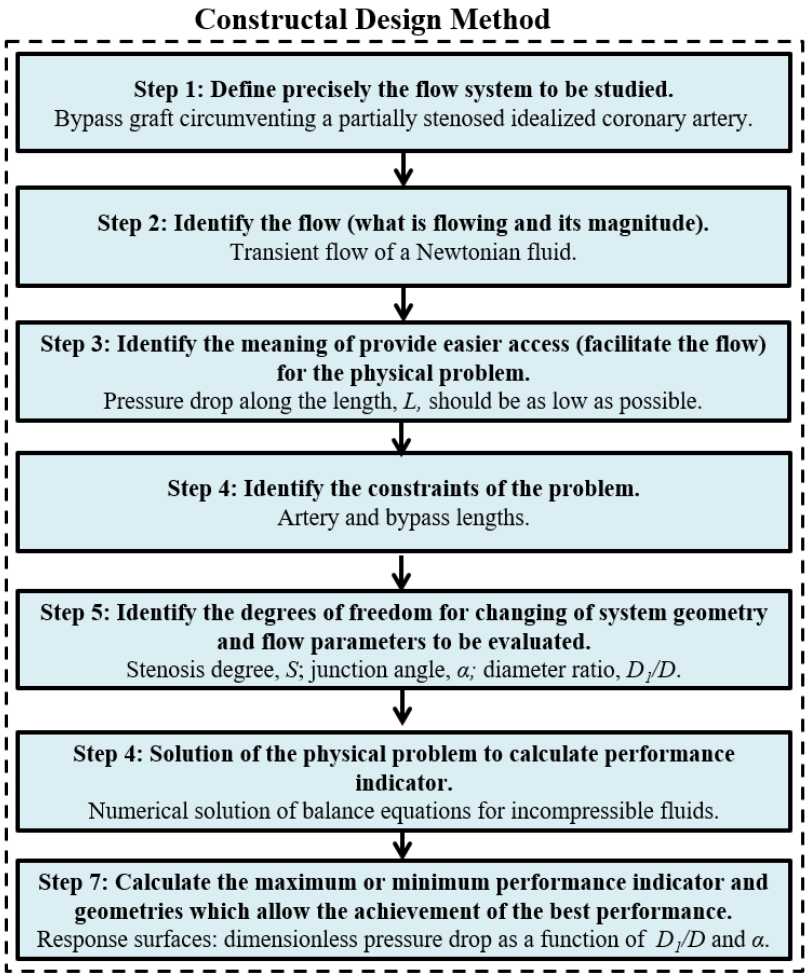

Figure 29. Flowchart showing the application of Constructal Design. [Ref. 7.4]

3.2.2 Problem Formulation

Several simplification hypotheses enter the study: 1) The blood flow is considered as a laminar isothermal pulsatile flow of an incompressible Newtonian fluid with density ρ=1000 kg m^{-3} and dynamic viscosity μ=0.0035 Pa s. The consideration of blood as a Newtonian fluid is used in literature to simplify the numerical model. 2) The pulsed blood flow is considered to simulate the blood flow triggered by the heartbeat. The inlet flow rate Q(t) it is considered, which is taken from Vimmir et al. [35] and should correspond to flow rate values measured in the right coronary artery during rest. In Appendix A the model for the description of the pulsed regime is presented through the use of the Fourier series.

3.2.3 Mathematical Modelling of Unsteady Blood Flow

The non-dimensional continuity and momentum balance equations for incompressible fluids are the equations solved to characterize the flow through the bypass model:

$$\frac{\partial \tilde{u}_i}{\partial \tilde{x}_i} = 0 \tag{3.2.3.1}$$

$$\frac{\partial \tilde{u}_i}{\partial \tilde{t}} + \tilde{u}_i \frac{\partial \tilde{u}_i}{\partial \tilde{x}_j} = -\frac{\partial \tilde{p}}{\partial \tilde{x}_i} + \frac{1}{Re}\frac{\partial \tilde{\tau}_{ij}}{\partial x_j} \tag{3.2.3.2}$$

where $\tilde{u}_i$ is the dimensionless velocity field, $\tilde{x}_i$ is the dimensionless position vector, $\tilde{p}$ is the dimensionless pressure drop, $\tilde{\tau}_{ij}$ is the dimensionless extra stress tensor field and Re the Reynolds number such that:

$$\tilde{u}_i = \frac{u_i}{U_m}; \qquad \tilde{x}_i = \frac{x}{D}; \qquad \tilde{p} = \frac{P_{RMS}}{\rho {U_m}^2}; \qquad \tilde{\tau} = \frac{\tau_{ij}}{(U_m \mu)/D}; \qquad Re = \frac{\rho U_m D}{\mu} \tag{3.2.3.3}$$

The reference velocity is obtained from the average inlet flow rate as $U_m = 4\,Q_0/\pi D^2 = 0.153\ m\ s^{-1}$. P_{RMS} is the root mean square pressure drop along with L.

The constitutive equation for the stress tensor is that of a generalized Newtonian liquid:

$$\tau_{ij} = 2\eta(\dot{\gamma})D_{ij} \tag{3.2.3.4}$$

where $\eta(\dot{\gamma})$ is the viscosity function and D_{ij} is the strain rate tensor, given as the symmetric part of the velocity gradient tensor (Slattery [59]). For a Newtonian fluid, $\eta(\dot{\gamma})$ is a constant and equal to μ.

According to Berger [60], blood presents Newtonian behavior when subjected to high shear rates (above 100 s^{-1}). In large vessels, such as the aorta, some authors have assumed Newtonian behavior for blood (Perktold et al. [61], Vimmr et al. [35]). Some authors have mentioned the importance of modeling blood as non-Newtonian in transient flows (Gisen et al. [62]), while others have concluded that blood could be modeled as a Newtonian fluid without significant changes in results when considering large arteries (Perktold et al. [63]).

Tiwari et al. [64] used analytical two-fluid models to investigate the roles of rheology and vessel wall porosity on the blood flow to constricted and unconstricted

vessels. They concluded that the modeling of blood rheology has a great effect in predicting flow behavior, having an important influence even in the deposition of fat over the vessel walls and in the hematocrit decay. In a further work, Tiwari et al. [64] also extended their modeling to investigate the flow of blood through microvessels and concluded that the modeling of blood as three-layered brings important features to the modeling that may have significant impact in the treatment of various diseases.

Although Vinoth et al. [65] point out that there may be a significant increase in wall shear stress patterns when using a non-Newtonian model, in comparison with Newtonian results, in the present paper the Newtonian model was employed, in view that the performance indicator for the Constructal Design Method was the time average pressure drop.

3.2.4 Boundary Conditions and Initial Conditions

The part of tube L_5 has been added in the inlet and outlet to measure the pressure drop in the length L. L_5 is *25D* long to allow the flow to reach fully stabilized speed. In this way, the velocity in the input patch can be set according to the formula

$$v(t) = \frac{Q(t)}{A} \tag{3.2.4.1}$$

where *Q(t)* is the flow rate taken from the Appendix A (Eq.(A.1)) and $A = \pi D^2/4$ is the area of the inlet section.

At the outlet boundary, the pressure outlet condition was employed, with an additional pipe length equal to L_5 to guarantee the complete flow development. Thanks to these choices, it is possible to measure the pressure over time *t* in the measurement sections, respectively, at $\pm L/2$ from the stenosis, as shown in the drawing of Fig. 1. As an initial condition, the velocity field was set as equal to *0.05 m/s* in the axis along with the whole flow domain.

3.2.5 Numerical Method and Computational Grid

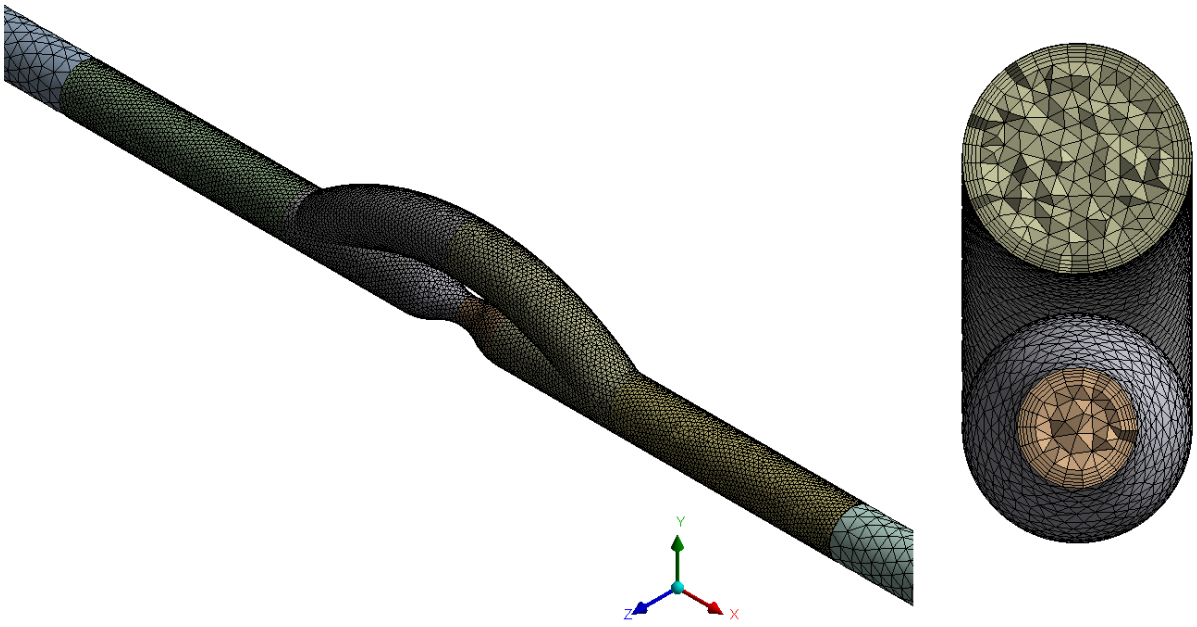

Figure 30. Isometric view of the computational mesh for the model with a detailed view of the cross-section in the bypass and native stenotic artery. [Ref. 7.4]

In order to solve the mathematical model given by Eqs. (81)-(85), the Finite Volume Method was employed (FVM). The FVM is known to be a robust method in the approximation of flow equations, for it is a conservative method at the level of the mesh control volume (Patankar [66]). The commercial code ANSYS Fluent 2019 R2 [67] was employed for its robustness and ease to use. The computational model was implemented using a pressure-based solver with a SIMPLE scheme (Patankar [66]) and second-order interpolation functions for pressure and momentum. All calculations used double-precision representation of real numbers. A time step of *0.01 s* was used for all simulations for tree cycle. The mesh was constructed to have a proper resolution in the narrowing area (stenosis position) and the bypass. Figure 30 presents a sample of the model's computational mesh with detailed views at the cross-section in the bypass and native stenotic artery. Grid quality tests were conducted for the cases shown in Table 3, where N_i is the number of mesh elements and $\tilde{p}_{N_i}^{3T}$ is the root mean square value of the pressure drop measured in the third cardiac cycle. As explained by Celik et al. [68], this method is useful for calculating and reporting discretization error estimates in CFD simulations where experimental data may not be available for comparison. It is

important to observe that the method considers, based on experience rather than formal derivation, a GCI value until 5% as acceptable (Celik et al. [68]). In this case the maximum GCI value is 3%. This ensures an acceptable mesh quality for all simulations as this value is less than 5%.

Table 3. Grid Convergence Index (GCI) for different bypass configurations [Ref. 7.4]

	Case 1	**Case 2**	**Case 3**	**Case 4**	**Case 5**	**Case 6**	**Case 7**	**Case 8**
$\boldsymbol{S}$	50%	50%	50%	50%	75%	75%	75%	75%
$\boldsymbol{D_1/D}$	1	1	0.5	0.5	1	1	0.5	0.5
$\boldsymbol{\alpha}$	30°	70°	30°	70°	30°	70°	30°	70°
$\boldsymbol{N_1}$	338492	356831	287447	356831	335188	353121	284653	290682
$\boldsymbol{N_2}$	187946	194353	163843	166519	185864	192902	162218	165150
$\boldsymbol{N_3}$	111398	114525	100512	102949	110599	114406	100431	102878
$\widetilde{\boldsymbol{p}}_{\boldsymbol{N_1}}^{\boldsymbol{3T}}$	3.879	4.931	8.462	9.325	4.356	6.237	29.091	35.198
$\widetilde{\boldsymbol{p}}_{\boldsymbol{N_2}}^{\boldsymbol{3T}}$	3.858	4.906	8.454	9.313	4.298	6.185	29.846	36.351
$\widetilde{\boldsymbol{p}}_{\boldsymbol{N_3}}^{\boldsymbol{3T}}$	3.862	4.925	8.481	9.327	4.306	6.255	31.576	38.781
$\boldsymbol{GCI}$	**0.16%**	**2.00%**	**0.050%**	**0.97%**	**0.27%**	**3.0%**	**2.5%**	**3.7%**

In Table 4 it is represented the error of the measure of the Root Mean Square from the relative cycle. The relative error is computed from the Eq.(3.2.5.1) and Eq.(3.2.5.2).

$$\varepsilon_{2,1} = \frac{|\tilde{p}_{2T} - \tilde{p}_{1T}|}{\tilde{p}_{2T}} \cdot 100 \qquad (3.2.5.1)$$

$$\varepsilon_{3,2} = \frac{|\tilde{p}_{3T} - \tilde{p}_{2T}|}{\tilde{p}_{3T}} \cdot 100 \qquad (3.2.5.2)$$

The pressure errors evaluated in the third cycle are of the order of 0.40 %, which is acceptable as an approximation.

Table 4. Relative error $\varepsilon_{i,i-1}$ from the cardiac cycle i to the cycle $(i-1)$ [Ref. 7.4]

	Case 1	Case 2	Case 3	Case 4	Case 5	Case 6	Case 7	Case 8
S	50%	50%	50%	50%	75%	75%	75%	75%
D_1/D	1	1	0.5	0.5	1	1	0.5	0.5
α	30°	70°	30°	70°	30°	70°	30°	70°
$\tilde{p}_{1T}$	3.897	4.949	8.497	9.357	4.364	6.257	29.170	35.264
$\tilde{p}_{2T}$	3.8789	4.935	8.479	9.324	4.350	6.2368	28.990	35.183
$\tilde{p}_{3T}$	3.879	4.931	8.462	9.325	4.356	6.237	29.091	35.198
$\varepsilon_{2,1}$	**0.46%**	**0.27%**	**0.22%**	**0.36%**	**0.33%**	**0.33%**	**0.62%**	**0.23%**
$\varepsilon_{3,2}$	**0.0048%**	**0.089%**	**0.21%**	**0.011%**	**0.14%**	**0.0038%**	**0.35%**	**0.042%**

The same procedure was used to characterize the mesh of the arteria narrowing without the bypass. The results are shown in Table 5 and Table 6. Also in this case, the maximum error is less than 0.3% so the calculation is an acceptable approximation.

Table 5. Grid Convergence Index (GCI) for arterial narrowing [Ref. 7.4]

	Case 1	Case 2
S	50%	75%
N_1	254011	251175
N_2	144907	143707
N_3	90391	89762
$\tilde{p}_{N_1}^{3T}$	12.741	226.589
$\tilde{p}_{N_2}^{3T}$	12.576	227.592
$\tilde{p}_{N_3}^{3T}$	12.401	254.838
GCI	**0.27%**	**0.021%**

Table 6. Relative error ε_(i,i-1) for arterial narrowing from the cardiac cycle i to the cycle (i-1) [Ref. 7.4]

	Case 1	Case 2
S	50%	75%
$\tilde{p}_{1T}$	12.783	227.711
$\tilde{p}_{2T}$	12.742	227.116
$\tilde{p}_{3T}$	12.741	226.589
$\varepsilon_{2,1}$	**0.32%**	**0.26%**
$\varepsilon_{3,2}$	**0.0038%**	**0.23%**

The numerical method and mesh to approximate the flow through the system comprised by the partially obstructed artery and the bypass graft has been verified through comparison with the results by Ko et al. [45]. This verification study may be found in detail in Dutra et al. [45].

3.2.6 Response Surface Methodology

To investigate the effects of the junction angle, α, and the artery diameter ratio, D_1/D, on the pressure drop along the length L, a Response Surface methodology was employed. Response surfaces provide a way to analyze the effect of two parameters on a result. The interaction between parameters is easily observed and quantified. It is common to find applications of the Constructal Design Method with two or more degrees of freedom where each degree of freedom is varied at a time (Razera et al. [69]). More recent works (Klein et al. [70]) have been using the Response Surface Method to investigate simultaneous effects of degrees of freedom as this is a basic premise of the Constructal Design Method: not only to get to the best geometry, but to investigate the effects of the degrees of freedom on system performance.

The Matlab Curve Fitting tool was used to create this surface. The application supports a variety of adaptation methods. The response surfaces were obtained with a second-order polynomial interpolation in the two variables. In the Measure inlet and outlet section (Figure 28), it was monitored the pressure's trend, obtaining the pressure values in the inlet and outlet for each time step. The difference between $p_{in}(t)$ and $p_{out}(t)$ gives the pressure drop along with L:

$$\frac{\Delta P}{L} = P_{in} - P_{out} \tag{3.2.6.1}$$

this pressure drop can be dimensionless with the equation

$$\tilde{p} = \frac{\left(\Delta P / L\right)}{\rho\, U^2} \tag{3.2.6.2}$$

Each geometry was computed using the Root Mean Square of the non-dimensional pressure drop (). For the seek of clarity the Root Mean Square formula is

$$\theta_{RMS} = \sqrt{\frac{\sum_{k=1}^{n_{max}} \theta_k^2}{n_{max}}} \tag{3.2.6.3}$$

where n_{max} is the number of the time step.

3.3 Results and Discussion

Figure 31 shows that when the aspect ratio D_1/D increases to 1 and the junction angle, α, decreases to 30º, $\tilde{p}$ decreases. However, as the stenosis degree becomes larger, i.e., the flow is highly deviated through the bypass, the influence of α in the $\tilde{p}$ has become almost unnoticeable. The results show that the diameter ratio D_1/D has more significant effects on the pressure drop than α.

The prominent influence of the D_1/D ratio compared to the α angle has been confirmed experimentally (Tsukui et al. [71]) and numerically (Xiong et al. [52]; Do et al. [52]; Vimmr et al. [52]) in idealized steady and pulsatile stenotic flows. Tsukui et al. [52], also confirmed that a smaller junction angle (α) yielded lower energy loss at the bypass graft. The present work confirms that the Constructal Design Method predicts the same trends found elsewhere using different frameworks for evaluating performance.

The surfaces of Figure 31 have been obtained by using polynomial interpolation. So, the surface equations are given by

$$\begin{aligned} &\tilde{p}(\alpha, D_1/D\,, S) \\ &= \begin{cases} \tilde{p}(\alpha, D_1/D) = 12.15 + 0.02363\,\alpha - 8.942\,(D_1/D), & for\ \ S = 50\% \\ \tilde{p}(\alpha, D_1/D) = 53.81 + 0.09958\,\alpha - 53.52\,(D_1/D), & for\ \ S = 75\% \end{cases} \end{aligned} \tag{3.3.1}$$

with a value of $R^2 = 0.9997$ for $S = 50\%$ and $R^2 = 0.9961$ for $S = 75\%$.

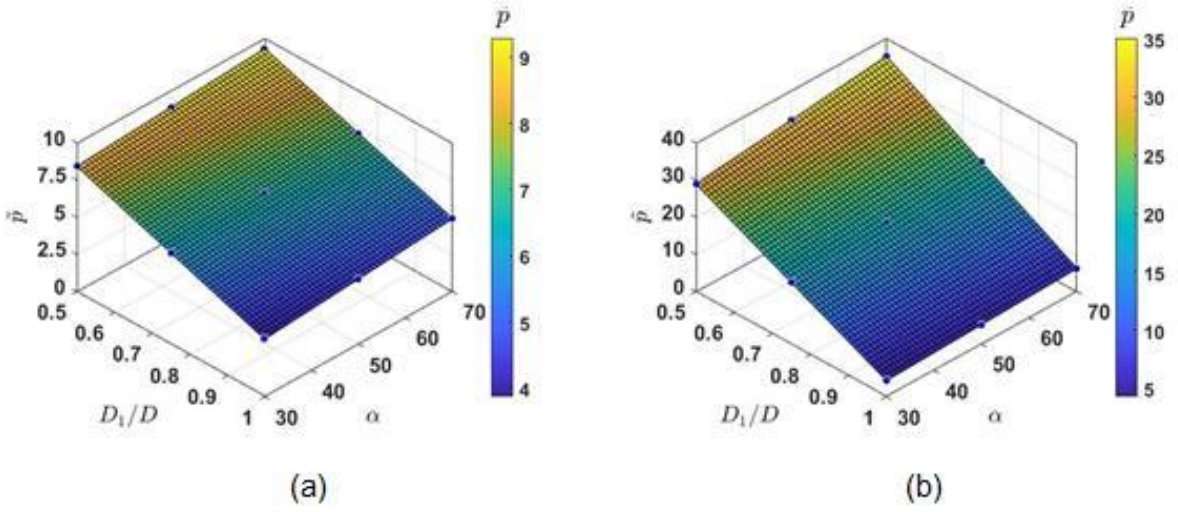

Figure 31. Dimensionless pressure drop $\tilde{p}$ (a) S=50%, (b) S=75% [Ref. 7.4]

The optimum point for both cases is D_1/D equal to 1 and α equal to 30°. This result leads us to believe that by increasing the aspect ratio D_1/D and decreasing the angle α, a better result would be obtained. However, this situation would be impracticable from the surgical standpoint because a graft of difficult suture would be produced (Vimmr et al. [35]). As a possible solution to this problem, Chua et al. [52], proposed sleeve models that could be used as mechanical connectors between the bypass graft and host artery, eliminating the need for quality suturing.

Chua et al [52], speculated that graft with a diameter of about 1 to 1.5 times larger than that of the host artery, and a junction angle in the range of 30–45° would improve hemodynamics.

Figure 32, on the other hand, shows the pressure drop $\tilde{p}$ compared to the pressure drop $\tilde{p}_0$ about the geometry without bypass. For stenosis degree S=50%, the pressure drop for the geometry without a bypass is $\tilde{p}_0 = 12.401$, and for S = 75% $\tilde{p}_0 = 254.838$. As can be seen, the introduction of the bypass ensures a decrease in the pressure drop value.

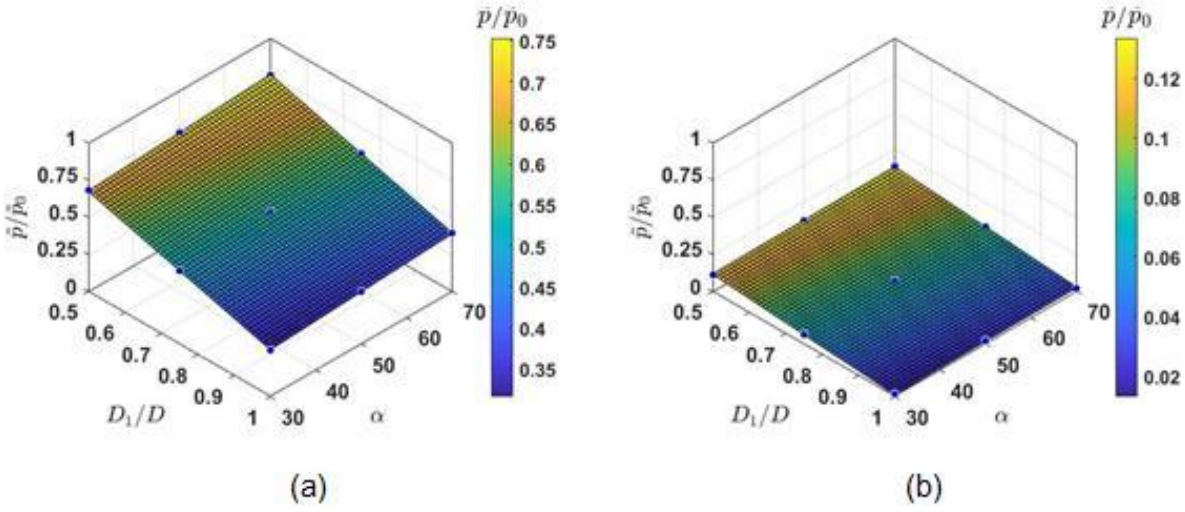

Figure 32. The ratio between pressure drop with bypass and pressure drop without bypass, (a) S=50%, $\tilde{p}_0 = 12.401$ (b) S=75%, $\tilde{p}_0 = 254.838$. [Ref. 7.4]

3.4 Results Extension

In literature, there are several numerical studies on the bypass graft (eg. Vimmr et al. [52] and references therein), but few of these consider the set of parameters to derive a correlation function. In this section the results are extended in order to access the effect of the bypass on the pressure drop of the system. The approach is based on the Constructal Theory, for it assumes the resistance to flow as the performance parameter to be calculated. The treatment of fluid dynamics through electrical equivalence is discussed in the literature (Bejan and Lorente [1]). So, the resistance R, measured in [Pa s / kg], that the fluid encounters to pass through a certain type of conduit from an inlet to an outlet section is defined as:

$$R = \frac{\Delta P}{\dot{m}} \tag{3.4.1}$$

where ΔP is the pressure drop measured in [Pa] and $\dot{m}$ is the mass flux measured in [kg/s].

The tube without bypass can be considered as a resistance R_s that creates a pressure drop that, at this point, is known. However, the overall effect of the pressure drop (the total resistance R) is known, but the pressure drop R_b due to the bypass is not known.

The system can be considered as the composition of two resistances in parallel, obtaining

$$\frac{1}{R} = \frac{1}{R_s} + \frac{1}{R_b} \tag{3.4.2}$$

where the unknown is R_b. From Eq.(3.4.1) it possible to write

$$R_b = \frac{R\ R_s}{R_s - R} \tag{3.4.3}$$

Thanks to Eq.(3.3.1), the Eq.(3.4.2) become

$$\Delta P_b = \frac{\Delta P\ \Delta P_s}{\Delta P_s - \Delta P} \tag{3.4.4}$$

Thanks to the response surface, obtained with simulations, the results for Eq.(3.3.1) are known in the range of this work. In other words, the pressure drop ΔP_b is a function of the type $\Delta P_b = f(\alpha, D_1/D, S)$. This means that Eq.(3.4.3) becomes

$$\Delta P_b(\alpha, D_1/D, S) = \frac{\Delta P(\alpha, D_1/D, S)\ \ \Delta P_s(S)}{\Delta P_s(S) - \Delta P(\alpha, D_1/D, S)} \tag{3.4.5}$$

where $\Delta P_s = \Delta P_s(S)$ is only a function of S as it has been determined not considering the bypass.

Therefore, considering Eq.(3.3.1) in the Eq.(3.4.5) the surfaces of Figure 33 are obtained, representing the pressure drop solely due to the bypass as a function of junction angle and diameter ratio for two stenosis degrees, 50%, and 75%. The pressure drop due to the bypass, ΔP_b, decreases as the values of the parameters of which this is a function decrease. This result is in good agreement with the results in the previous section.

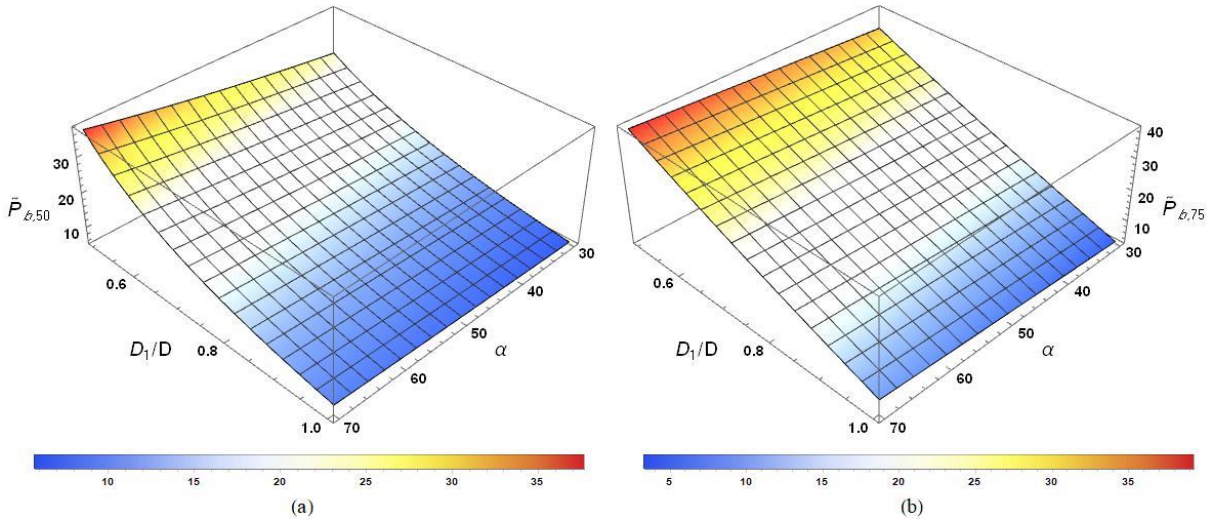

Figure 33. Plot of Eq.(21) with (a) $S = 50\%$, $\tilde{p}_s = 12.401$ and (b) $S = 75\%$, $\tilde{p}_s = 254.838$ [Ref. 7.4]

3.5 Concluding Remarks

This manuscript examined the effects of geometric parameters in different flow conditions of a bypass graft in a partially stenosed idealized coronary artery. By determining the constraints across the Constructal Design and using the Response Surface methodologies, two principal response surfaces were generated (Figure 31 with Eq.(3.3.1)), each representing the stenosis degree, *S*, equal to 50% and 75%. It was found in which values of D_1/D and α, the dimensionless pressure drop, $\tilde{p}$, is minimum. In all situations, as the junction angle decreases to 30º, and the diameter ratio increases to 1, the pressure drop $\tilde{p}$ decreases. Furthermore, the impact on pressure drop $\tilde{p}$ due to the degree of stenosis *S* was of considerable importance. The optimum point for all cases is $D_1/D_{,opt}$ equal to 1 and $\alpha_{,opt}$ equal to 30°, which is confirmed by previous studies. The results showed that D_1/D has more significant effects than α.

The results obtained from the entire geometry were compared with the pressure variation due to the stenosis presence without the bypass (Figure 32). As a result, bypass's presence is all the more beneficial, the higher the shrinkage. The overpressure caused by the shrinkage is significantly reduced thanks to the deviation that the flow undergoes in the bypass region.

From this analysis, it is possible to derive the system pressure drop, but this data can be manipulated to understand the influence of the single bypass on the pressure

drop. Thanks to the analogy between fluid dynamics and electronics, it is possible to see the system consisting of two parallel resistors. Therefore, the correlation that determines the pressure drop due to the bypass as a function of parameters α and D_1/D was established. The results of Eq.(3.19) in Figure 33 confirm that the point $(\alpha, D_1/D) = (30°, 1)$ is a point of minimization of the resistance, i.e., it is the optimum point. It is possible to conclude that the Constructal Design Method predicts lower flow resistance for smaller angles (α) and greater diameter ratio (D_1/D), as found in previous works.

This study presents limitations as using an idealized geometry for the coronary artery and neglecting vessel walls elasticity. Nonetheless, it brings insights on the performance of artery-bypass systems in the framework of the Constructal Theory. As the Constructal Design Method has been increasingly used in engineering projects, it is expected that the present work will provide motivation for its use in the area of bioengineering and health.

4. Effect of the Bypass Attachment Point on Resistance to Flow by Constructal Design

This chapter aims to investigate, through the 3D numerical analysis of an idealized arterial bypass graft, the dependence of the resistance to flow on the bypass insertion point. The computational model assumes a laminar steady-state Newtonian fluid flow and three different Reynolds numbers: 150, 250, and 400. In this study constructal theory has been employed, a self-standing law in physics which covers the statement of minimum flow resistance to optimize morphing architectures, i.e. the coronary artery bypass grafting. According to the Constructal Design method, the constraints were stenosis degree, junction angle, and diameter ratio, while the attachment point was defined as a design parameter. The results demonstrated that the distance between the bypass attachment point and the stenosis influences the pressure drop; more specifically, the pressure drop decreases with the augmentation of the distance. On this regard, a different distribution of the mass flows between the bypass, and the artery was observed and seemed to be the main reason for that behavior. The application of the Constructal Design method in hemodynamics is a tool to describe the biological system to search for better flow performance since it is based on the natural evolution of living systems.

4.1 Introduction

Arteriosclerosis is a tissue hardening, or sclerosis, of the arterial wall that appears with age as a consequence of the accumulation of fibrous connective tissue at

the expense of the elastic component [72]. Tian at al. [39] and Liu et al. [40] explain that the main manifestations of atherosclerosis are stenoses, or the formation of atherosclerotic plaques on the internal wall of the arteries with consequent narrowing of the lumen, and aneurysms, or the loss of elasticity of the wall of a vessel that involves distension. According to Guerciotti et al. [40], one type of surgery, for people with high risk, is the coronary artery bypass graft (CABG) innest. The surgical procedure consists of bypassing a stenotic region to restore the heart's blood flow. Intimal hyperplasia (IH) is the principal factor that affects graft patency. An anomalous production of smooth muscle cells arises between the graft and the coronary artery instigating a reduction of the lumen of the graft and the consequent restenosis and obstruction of the graft [42]. The science of computational fluid dynamics (CFD) has been applied extensively to explore the connection between hemodynamics in CABGs and IH development and assist in the improvement of a top graft design. Bertolotti and Deplano [73] used a three-dimensional numerical model with different stenosis positions relative to the downstream junction. They concluded that the risks of intimal hyperplasia at the anastomosis might be reduced by increasing the distance between the stenosis and the junction. Lee et al. [46] studied the flow behavior of a complete bypass graft and a 100% occluded artery with different Reynolds number and junction angles. Vimmr et al. [46] implemented several numerical simulations of a complete three-dimensional coronary bypass model as a function of three geometrical parameters (stenosis degree, junction angle, and diameter ratio). They revealed that the diameter ratio was the most crucial parameter for coronary artery bypass grafting (CABG).

In Ref. [74], the stenosed coronary artery bypass graft including an analysis of the blood flow phenomena and wall shear stress, based on a three-dimensional computer model, was analyzed and developed to approach a realistic situation, inlet pulse and non-Newtonian behavior. The results demonstrated that the anastomosis of 45° was the most appropriate for resolving the coronary heart disease problem. Moreover, Ref. [75] is focused on the study of several configurations of patient-specific coronary artery bypass grafts while a specific design for coronary arterial bypass

surgical grafting, consisting of coupled sequential side-to-side and end-to-side anastomoses, is treated in Ref. [76]. On the same topic, O'Callaghan et. Al. in Ref. [77] demonstrated that the choice of blood constitutive equation (among Newtonian, Carreau, Power law, Carreau–Yasuda, Bi-exponential, Cross, Modified Cross, Herschel–Bulkley, etc.) has to be based on the particular situation under study e.g. flow rate, steady/unsteady flow, and geometry. Additional interesting computations regarding coronary artery bypass grafting have been treated in Refs. [78]-[79].

Dutra et al. [43] applied the Constructal Design to investigate the effect of geometric parameters on the flow through a bypass graft circumventing an idealized, partially-stenosed coronary artery. They have discovered that at fixed flow conditions, the pressure drop is mitigated if the parameters assume a specifics values. The introduction of the Constructal Design method into the field of hemodynamics brings a valuable tool to the understanding of biological problems since the bypass geometry is known to affect the blood flow field significantly and to play an essential role in potential graft failure due to intimal hyperplasia.

The Constructal design method has been employed in various engineering sectors [80]-[81], and beyond, as a new approach for solving optimization problems. In general, according to Constructal Law, stated by Adrian Bejan in 1996, "for a finite-size flow system to persist in time (to live) it must evolve with freedom in such a way that it provides easier access to imposed currents that that flow through it" [82]. Constructal Law deals with the physical concepts of life, evolution, design, performance, and time arrow. Under Constructal Theory, evolution and design in nature are deterministic because the living systems evolve in such a way to decrease resistance to flow [13]. Constructal Design is the method that allows the mathematical modeling of flow systems evolution. It can explain the configuration of existing systems in nature and to design flow systems in engineering. This design methodology has the objectives of accessing the effects of shape and geometry in flow performance and finding the so that the optimal geometry may be discovered by means of a given optimization technique (exhaustive search or heuristic methods), according to

Constructal Law [3]. Therefore, taking into account the domain of coronary artery bypass grafting, this papers documents numerically, on the basis of Constructal design, the search for the length ratio that minimizes the dimensionless pressure drop for definite combinations of stenosis degree, junction angle, aspect ratio and Reynolds number. It is worth mentioning that no previous studies were found in literature specifically focused on the effect of the bypass attachment point.

4.2 Methodology

4.2.1 Constructal Design

Dutra at al. [43] have conducted a very detailed study on the application of the Constructal Design method to determine the system constraints and parameters. The evaluation of the constraints begins from the definition of the domain shown in Figure 34.

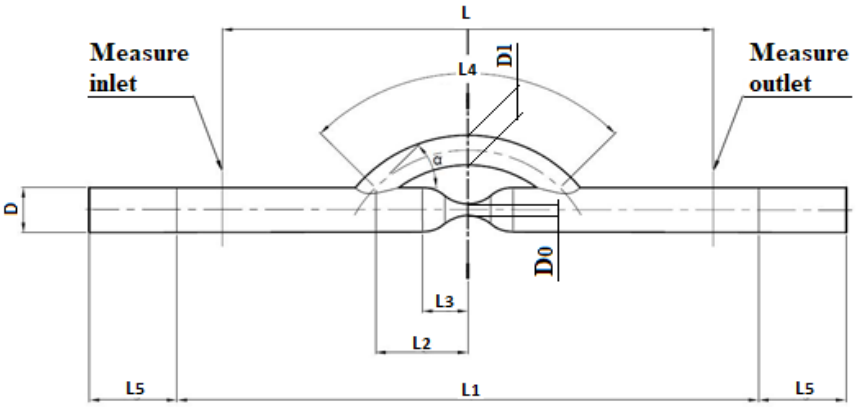

Figure 34. Problem Domain. [Ref. 7.5]

It is an idealized version of an artery partially obstructed and implanted with a symmetrical graft. The artery is represented as the host artery with a diameter equal to D and length equal to L_1+ $2L_5$. The main tube undergoes stenosis that reduces its diameter D_0. The graft is placed at a distance L_2 from the center of the stenosis, and D_1 denotes its diameter. The junction angle is α, and the graft diameter is D_1. L_3 is the distance from the center at the tube starts to get narrow, i.e., it models the stenosis morphology. According to Ref. [43], the flow is incompressible and Newtonian. The inlet average velocity is Um, assessed by fixing the Reynolds Number. The tube walls

are modeled as rigid, impermeable, and non-slip. The flow is also assumed to be three-dimensional, steady, incompressible, and laminar. It is worth mentioning that the hypothesis of steady state simulations is common in literature (Refs. [83]). The inlet section was placed far from the stenosis (L_5 = 25D) to ensure that the flow arrives, at the bypass inlet, fully developed. Instead, the outlet section was also taken away from the stenosis (L_5) in such a way as to minimize the effect of imposing the constant outlet pressure value. Imposing a constant outlet pressure value is not realistic, but it is necessary to solve the equations in this case. For all simulations, the host artery diameter D is equal to 3 mm, corresponding to an average value of the right coronary artery. The system's characteristic volumes were defined in the following way [83], where the total artery volume V is considered without the narrowed:

$$V = \pi \frac{D^2}{4} (L_1 + 2L_5) \tag{4.2.1.1}$$

where D is the artery diameter and (L_1+2L_5) is the total artery length. The graft volume V_1 is

$$V_1 = \pi \frac{D_1^2}{4} L_4 \tag{4.2.1.2}$$

where D_1 is the graft diameter and L_4 is the total graft length. It is worth mentioning that the graft is not a straight cylinder with inlet/outlet normal to its axis. In this work, the value of V was fixed considering D = 3 mm, L_1 = 50D and L_5 = 30D. Instead, the value of V_1 is not fixed because the length L_4 is a function of the bypass attached point position (L_2) and the junction angle α. The stenosis degree S is calculated as

$$S = \frac{D - D_0}{D} 100 \tag{4.2.1.3}$$

where D_0 is the diameter at the center of the stenosis.

A baseline case from literature [84] was used for the definition of the values L_1/D = 16.67 and L_3/D=1. The value L_2/D is the parameter that is made to vary in the range 2.5≤L_2/D≤6.67. Figure 35 shows the configuration for L_2/D equal to 2.5, 4 and 6.67. In Ref. [83] this parameter was fixed at 2.5 D. This means that considering D = 3mm, the value of L_2 was fixed at 7.5 mm. In this work L_2 varies from 7.5 mm to 20 mm.

At fixed bypass junction angle α (30°) and bypass diameter ratio D_1/D=1, two values of stenosis degree S (50% and 75%) were evaluated at three different Reynolds Numbers (150, 250 and 400). Blood is modelled as an incompressible Newtonian fluid with density ρ = 1000 kg/m^3 and dynamic viscosity μ = 0.0035 Pa.s [45]. The assumption of blood as Newtonian fluid is acceptable and used by other studies in the hemodynamic area, e.g., Ko et al. [45], [49], Xiong and Chong [52] and Vimmr et al. [35]. The choice to keep α and D_1/D fixed at the chosen values derives from the fact that it is interesting to investigate the effect over the pressure drop due to the bypass attachment point position. From previous studies [35], [43] it is known that an increase of α would cause a greater pressure drop while a decrease of α would cause a lower pressure drop. With D_1/D values close to 1, the effect on the pressure drop improves significantly [35], [43].

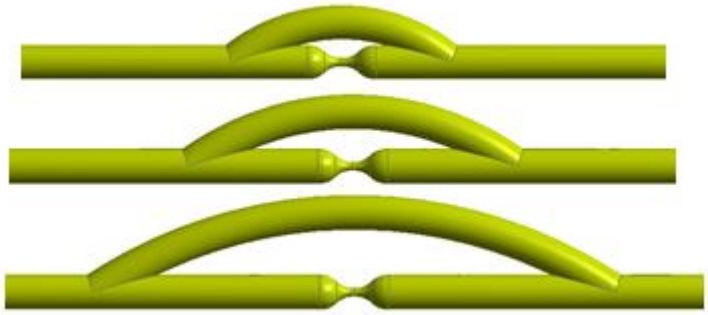

Figure 35. Some different bypass graft configuration for L2/D equal to 2.5 (top), 4 (middle) and 6.67 (bottom) at fixed bypass junction angle α = 30° and bypass diameter ratio D1/D = 1. [Ref. 7.5]

Constructal Theory assumes that living systems evolve limited by space [1]. Accordingly, Constructal Theory systems must evolve to provide easier access to its flows [2]. To this end, it was considered that the dimensionless pressure drop $\tilde{p}$ (that will be defined in Eq.(4.2.2.3)) along the length L should be as low as possible. Thus, an optimization problem was formulated as in Ref. [83]: "Find the minimum $\tilde{p}$. The design variable is the length ratio L_2/D." Therefore, the degree of freedom for this problem is the diameter ratio L_2/D. A search is conducted for the length ratio L_2/D that

minimizes the value of the pressure drop $\tilde{p}$ for specific combinations of S, α, D_1/D and Re. Figure 36 details all the steps required by the Constructal Design methodology.

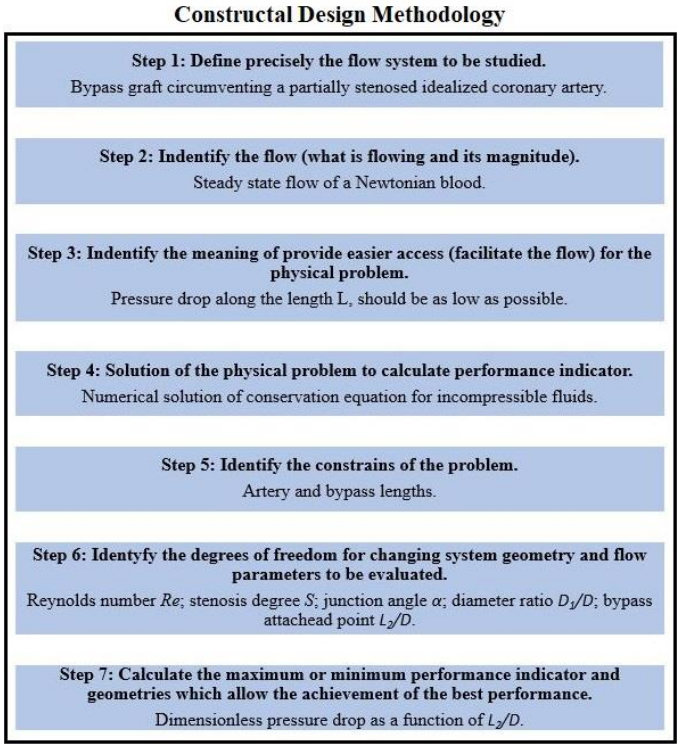

Figure 36 . Constructal design flowchart. [Ref. 7.5]

4.2.2 Mathematical Modelling

The flow system is described by the mass and moment balance equations [83]:

$$\frac{\partial \tilde{u}_i}{\partial \tilde{x}_i} = 0 \qquad (4.2.2.1)$$

$$\frac{\partial \tilde{u}_i}{\partial \tilde{t}} + \tilde{u}_i \frac{\partial \tilde{u}_i}{\partial \tilde{x}_j} = -\frac{\partial \tilde{p}}{\partial \tilde{x}_i} + \frac{1}{Re}\frac{\partial \tilde{\tau}_{ij}}{\partial x_j} \qquad (4.2.2.2)$$

where $\tilde{u}_i$ is the dimensionless velocity field, is the dimensionless position vector, is the dimensionless pressure drop, is the dimensionless extra stress tensor field and Re is the Reynolds number defined as [83]:

$$\tilde{u}_i = \frac{u_i}{U_m}; \qquad \tilde{x}_i = \frac{x}{D}; \qquad \tilde{p} = \frac{\Delta p}{\rho {U_m}^2}; \qquad \tilde{\tau} = \frac{\tau_{ij}}{(U_m \mu)/D}; \qquad Re = \frac{\rho U_m D}{\mu} \qquad (4.2.2.3)$$

where U_m is the average velocity at the inlet, D is the diameter of the artery, ΔP is the pressure drop along L, ρ is the fluid mass density and μ is the fluid viscosity.

The constitutive equation for the extra stress is that of a generalized Newtonian liquid [85]:

$$\tau_{ij} = 2\eta(\dot{\gamma})D_{ij} \qquad (4.2.2.4)$$

where is the viscosity function and D_{ij} is the strain rate tensor, given as the symmetric part of the velocity gradient tensor [59]. For a Newtonian fluid, is a constant and equal to μ [59]. For the simulation it was considered a Newtonian blood as working fluid. The physical properties and parameters used for the dimensioning of Eqs.(4.2.2.1)-(4.2.2.2), according to rules Eq.(4.2.2.3), are ρ=1000 kg/m^3 and μ=0.0035 Pa s.

4.2.3 Numerical Method and Computational Grid

Using ANSYS/FLUENT [67], the Finite Volume Method [86] was employed to solve the partial differential equation system. A pressure-based solver was used with a pressure-velocity coupling method, second-order interpolation functions for velocity fields, and linear interpolation function for the pressure field. All calculations were conducted in a double-precision representation of real numbers. The iterative algorithm was a false transient. The mesh was parameterized to keep the element sizes proportional according to the stenosis configuration and diameter ratio studied. Figure 37 shows the division of the domain.

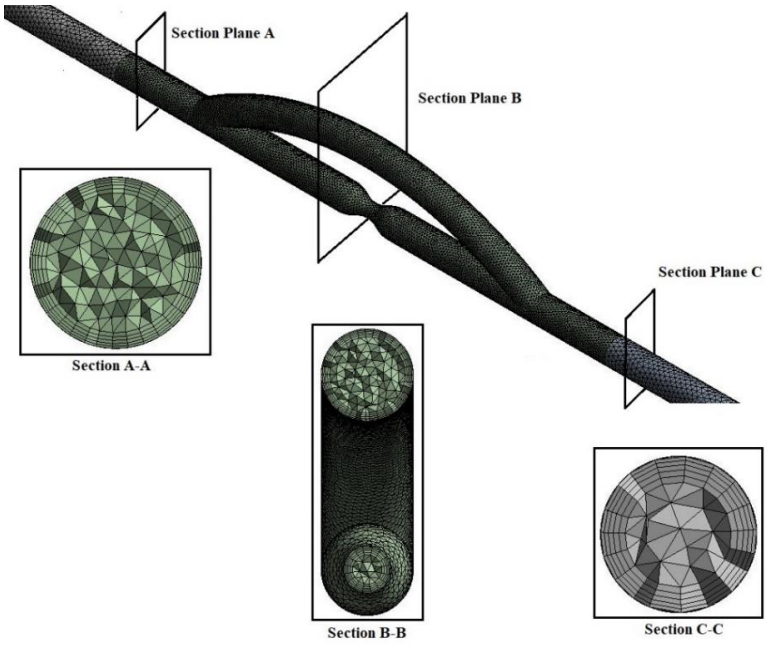

Figure 37. Computational mesh. [Ref. 7.5]

The inlet and outlet ducts are discretized with tetrahedral finite elements with size 5.5×10^{-4} m. Instead, the area of interest was discretized with smaller tetrahedral finite elements having size 3.0×10^{-4} m. Along the walls, prismatic layers elements were used to capture the boundary layer better. Figure 37 presents a sample of the computational mesh for the model with detailed views at the cross-section in the different zone of the domain. As a convergence criterion scaled residuals of each equation at an iteration were used and compared with a user-defined convergence criterion equal to 10^{-6} for velocity and pressure fields. The Grid Convergence Index (GCI) method was applied for different values of Reynold number Re and length junction L_2/D at two values of stenosis degree S (50%, and 75%). As explained by Celik et al. [83], this method is useful for calculation and reporting of discretization error estimated in CFD simulations where experimental data may not be available for comparison. Table 7 and Table 8 summarize these results for S = 50% and S = 75% respectively. N_i represents the number of elements. It can be verified that the maximum GCI index was 2.36% using a refining mesh of a 30% factor. It is important to observe that, based on experience and not on formal derivation, a maximum GCI value of 5%

is considered acceptable for this method [83]. The method to evaluate the pressure drop ΔP is explained in Section 4.2.4.

Table 7. Grid Convergence Index (GCI) for S = 50 %, α = 30° and D1/D = 1 (with D = 3 mm). [Ref. 7.5]

		Case 1	Case 2	Case 3	Case 4	Case 5	Case 6	Case 7
	L_2/D	2.50	2.67	3.33	4.00	5.00	6.00	6.67
	N_1	259310	262360	276020	286970	304790	114870	118950
	N_2	156580	158630	164620	170220	179030	73428	75842
	N_3	105150	106960	110460	113490	118560	50887	52255
Re=150	ΔP_{N1} [Pa]	109.55	109.46	106.73	102.42	98.09	91.71	87.41
	ΔP_{N2} [Pa]	109.39	109.40	106.86	103.30	97.87	91.48	87.16
	ΔP_{N3} [Pa]	109.52	109.53	106.96	103.48	98.04	91.79	87.48
	GCI %	0.80	0.060	0.58	0.29	0.97	0.91	1.30
Re=250	ΔP_{N1} [Pa]	202.39	200.07	197.79	191.77	182.89	171.38	162.02
	ΔP_{N2} [Pa]	201.93	200.11	197.24	191.18	182.27	171.08	162.02
	ΔP_{N3} [Pa]	202.15	200.42	196.86	191.82	182.63	171.10	161.81
	GCI %	0.27	0.0040	0.86	0.50	0.60	0.017	4.17×10^{-7}
Re=400	ΔP_{N1} [Pa]	367.90	367.90	356.99	349.56	336.80	318.20	302.45
	ΔP_{N2} [Pa]	367.98	366.61	356.46	347.82	335.10	316.68	300.97
	ΔP_{N3} [Pa]	366.87	364.96	35640	348.62	335.38	316.74	301.19
	GCI %	0.0023	1.81	3.67×10^{-6}	0.54	0.13	0.027	0.11

Table 8. Grid Convergence Index (GCI) for S = 75 %, α = 30° and D1/D = 1 (with D = 3 mm). [Ref. 7.5]

		Case 1	Case 2	Case 3	Case 4	Case 5	Case 6	Case 7
	L_2/D	2.50	2.67	3.33	4.00	5.00	6.00	6.67
	N_1	258330	261020	273360	285660	303880	321410	333890
	N_2	156090	157110	163950	170180	178670	187930	194740
	N_3	104770	92633	110070	113380	116550	121490	125240
Re=150	ΔP_{N1} [Pa]	118.50	119.20	118.13	117.24	115.87	114.00	112.38
	ΔP_{N2} [Pa]	118.58	119.39	118.19	117.31	116.09	114.31	112.90
	ΔP_{N3} [Pa]	118.70	119.69	118.22	117.84	116.54	114.75	113.02
	GCI %	0.17	0.34	0.064	0.011	0.23	0.81	0.17
Re=250	ΔP_{N1} [Pa]	220.58	219.39	221.67	219.44	218.77	217.09	214.24
	ΔP_{N2} [Pa]	219.85	221.87	221.58	219.18	218.63	216.93	215.00
	ΔP_{N3} [Pa]	219.97	22.75	221.94	219.97	219.13	216.50	214.36
	GCI %	0.081	0.018	0.017	0.073	0.031	0.055	2.36
Re=400	ΔP_{N1} [Pa]	407.32	402.57	405.40	403.72	403.98	408.43	407.32
	ΔP_{N2} [Pa]	405.12	407.88	405.05	403.85	402.66	405.36	406.71
	ΔP_{N3} [Pa]	403.98	408.40	406.66	404.33	405.83	406.45	406.01
	GCI %	0.73	0.18	0.030	0.015	0.29	0.52	1.27

In Table 9 the GCI index for geometry without bypass is analyzed with the aim of comparing the results of the different geometries. The mesh with the identical elements size was applied at the artery graft without bypass for evaluating the pressure drop on the same length and compare the results.

Table 9. Grid Convergence Index (GCI) stenosis artery. [Ref. 7.5]

		S=50%	S=75%
	N_1	318440	417500
	N_2	185110	234950
	N_3	118740	153360
Re=150	$\Delta P_{N1,0}$ [Pa]	286.61	4745.40
	$\Delta P_{N2,0}$ [Pa]	286.94	4739.95
	$\Delta P_{N3,0}$ [Pa]	288.85	4738.83
	GCI %	0.030	0.037
Re=250	$\Delta P_{N1,0}$ [Pa]	627.61	11791.00
	$\Delta P_{N2,0}$ [Pa]	622.31	11780.35
	$\Delta P_{N3,0}$ [Pa]	622.49	11420.80
	GCI %	0.037	0.0034
Re=400	$\Delta P_{N1,0}$ [Pa]	1300.30	27750.00
	$\Delta P_{N2,0}$ [Pa]	1301.10	27690.35
	$\Delta P_{N3,0}$ [Pa]	1302.00	27680.98
	GCI %	0.62	0.050

4.2.4 Procedure

Figure 38 shows the planes position where the pressure inlet P_{in} and pressure outlet P_{out} measurements were taken. The measurements planes have been positioned symmetrically concerning the shrinkage point. The distance L has been defined at 50 mm, or equivalent L/D=16.67. The L dimension remains fixed for all simulations. Once the pressure values have been obtained, the pressure drop (Δp/L) has been calculated as:

$$\left(\frac{\Delta P}{L}\right) = P_{in} - P_{out} \tag{4.2.4.1}$$

After that, the values calculated according to Eq.(4.2.4.1) have been compared with the pressure drop due without the bypass computed in the same way, obtaining the dimensionless quantity:

$$\tilde{p} = \frac{(\Delta P/L)}{(\Delta P/L)_0} \tag{4.2.4.2}$$

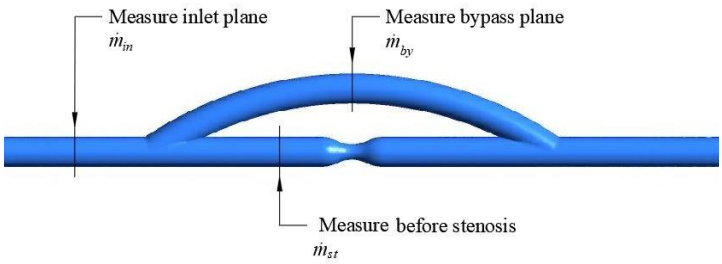

Figure 38. Plane measure. [Ref. 7.5]

4.3 Results and Discussion

Figure 39 and Figure 40 show the pressure drop as a function of the degree of freedom L_2/D with range $2.50 \leq L_2/D \leq 6.67$. Each curve represents the results of stenosis degree S equal to 50% and 75% at Reynolds Number Re equal to 150, 250, and 400.

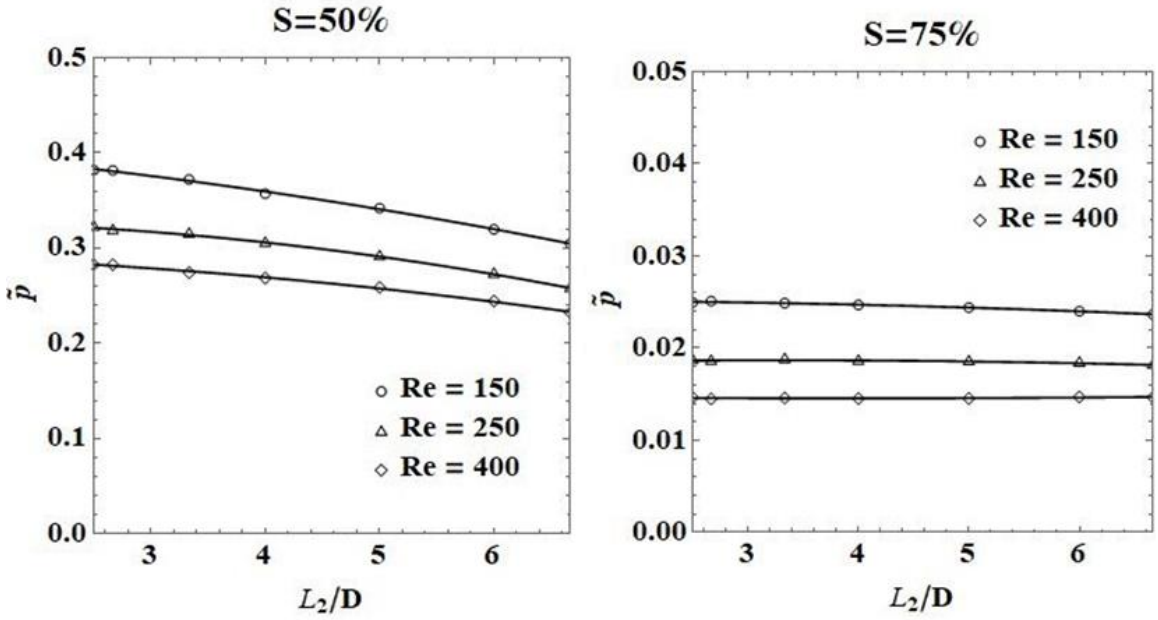

Figure 39. Comparison of dimensionless pressure drop trend for S=50% (left) and S=75% (right) at different Reynolds Number Re. [Ref. 7.5]

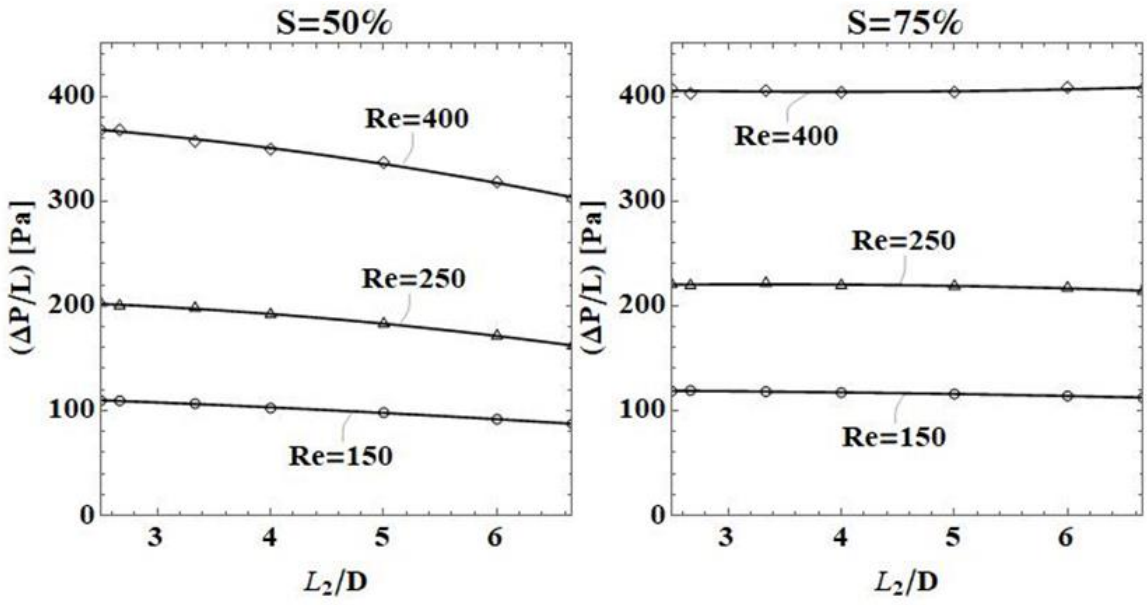

Figure 40. Comparison of dimensional pressure drop trend for S=50% (left) and S=75% (right) at different Reynolds Number Re. [Ref. 7.5]

The results show a monotonically decreasing trend for the pressure drop with increasing the distance of the bypass connection point L_2. This effect is significantly affected by the velocity of the fluid. When the Reynolds Number Re increases, the pressure drop follows the same trend of the other Reynolds numbers, but the magnitude of $\tilde{p}$, or ($\Delta p/L$), decreases. The stenosis S value has an important effect on the pressure drop. The pressure mitigation effect with the bypass attachment point is less evident when S = 75%. Its trend remains approximately constant for each Reynolds values. To understand better the beneficial effect of the bypass, the mass flux in the different areas of the system was assessed. Table 10 and Table 11 are referred to Figure 41 and show the mass flow rate for S = 50% and S = 75% respectively.

The stenosis section was considered before the actual stenosis zone to be able to compare all mass flow rate with the other sections since the diameter remains equal to D.

As Number Re increases, the mass flow rate is distributed in an increasingly different way, favoring the passage in the bypass section. This effect is more marked when the stenosis S increases. The mass flow rate through the bypass represents approximately 65-70% of the total mass flow rate. Knowing the mass flow rate values in the different bypass sections, it was possible to evaluate the resistances to the passage of fluid, due to the relation

$$R = \frac{\Delta p}{\dot{m}} \tag{4.3.1}$$

where the resistance R is evaluated in [Pa s/kg] in S.I. It is worth mentioning that, with reference to Figure 34., the resistance is evaluated between the outlet and inlet measure plane.

Table 12 and Table 13 show the evaluations of the resistance R in the stenosis and bypass sections for S values 50% and 75% respectively. The graphical results form of Table 12 and Table 13 is represented in Figure 42. The flow resistance decreases monotonically with increasing L_2. In particular, the stenotic resistance undergoes a considerable decrease with the increase of the bypass attachment point.

Finally, Figure 43 illustrates velocity contours and streamlines with reference to a couple of outcome results. Please note the optimal configuration depiced on the right, having the following coordinates: L_2/D=6.67, S=75%, and Re=150.

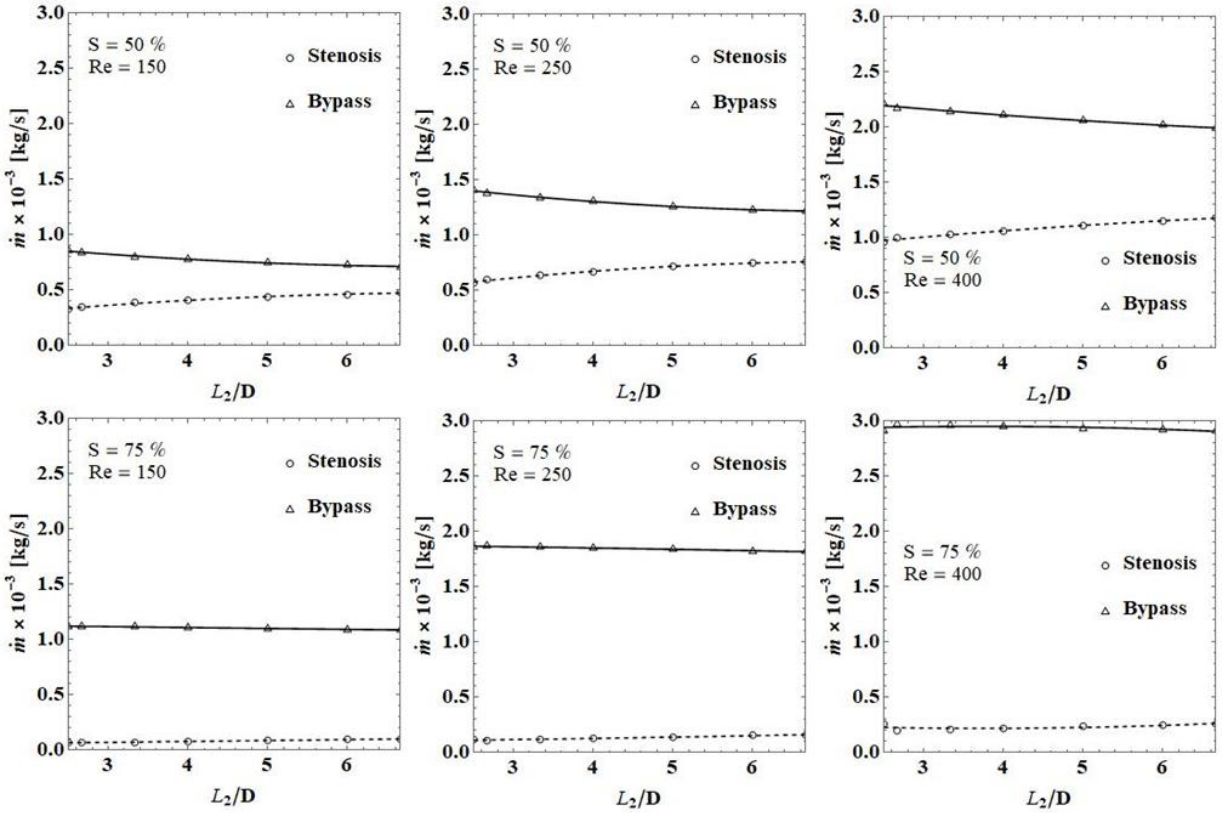

Figure 41. Mass flow rate for S = 50% (top: Table 4) and S = 75% (bottom: Table 5). [Ref. 7.5]

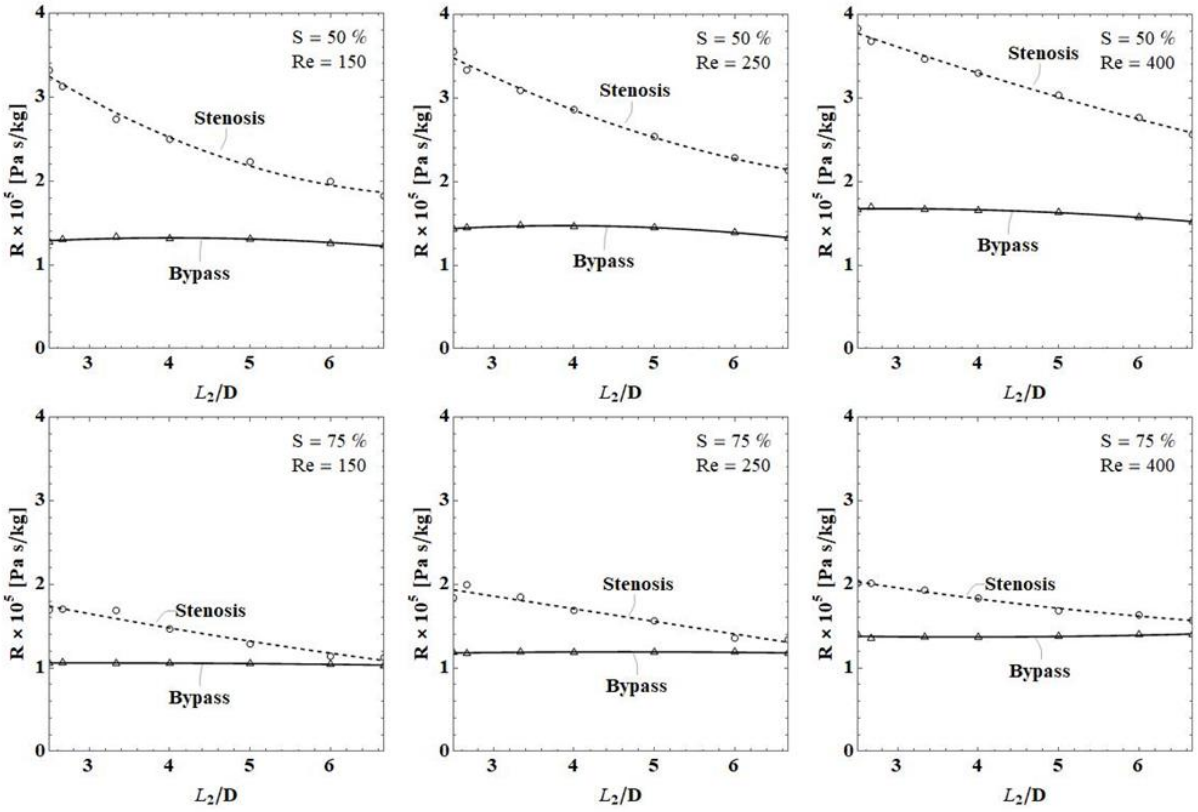

Figure 42. Resistance R for S = 50% (top: Table 6) and S = 75% (bottom: Table 7). [Ref. 7.5]

Table 10. Evaluation of the mass fluxes in the measure inlet section ($\dot{m}_{in}$) stenosis section ($\dot{m}_{st}$) and central bypass section ($\dot{m}_{by}$) for S = 50 %, = 30° α and D1/D = 1 (with D = 3 mm). [Ref. 7.5]

		Re=150, $\dot{m}_{in}$ = 1.19×10-3 kg/s		Re=250, $\dot{m}_{in}$ =1.98×10-3 kg/s		Re=400, $\dot{m}_{in}$ = 3.17×10-3 kg/s	
		10^{-3} kg/s	%	10^{-3} kg/s	%	10^{-3} kg/s	%
L2/D=2.50	$\dot{m}_{st}$	0.33	27.73	0.57	28.79	0.96	30.28
	$\dot{m}_{by}$	0.86	72.27	1.41	71.21	2.21	69.72
L2/D=2.67	$\dot{m}_{st}$	0.35	29.41	0.60	30.30	1.00	31.55
	$\dot{m}_{by}$	0.84	70.59	1.38	69.70	2.17	68.45
L2/D=3.33	$\dot{m}_{st}$	0.39	32.77	0.64	32.32	1.03	32.49
	$\dot{m}_{by}$	0.80	67.23	1.34	67.68	2.14	67.51
L2/D=4.00	$\dot{m}_{st}$	0.41	34.45	0.67	33.84	1.06	33.44
	$\dot{m}_{by}$	0.78	65.55	1.31	66.16	2.11	66.56
L2/D=5.00	$\dot{m}_{st}$	0.44	36.97	0.72	36.36	1.11	35.02
	$\dot{m}_{by}$	0.75	63.03	1.26	63.64	2.06	64.98
L2/D=6.00	$\dot{m}_{st}$	0.46	38.66	0.75	37.88	1.15	36.28
	$\dot{m}_{by}$	0.73	61.34	1.23	62.12	2.02	63.72
L2/D=6.67	$\dot{m}_{st}$	0.48	40.34	0.76	38.38	1.18	37.22
	$\dot{m}_{by}$	0.71	59.66	1.22	61.62	1.99	62.78

Table 11. Evaluation of the mass fluxes in the measure inlet section ($\dot{m}_{in}$) stenosis section ($\dot{m}_{st}$) and central bypass section ($\dot{m}_{by}$) for S = 75 %, = 30° α and D1/D = 1 (with D = 3 mm). [Ref. 7.5]

		Re=150, $\dot{m}_{in}$ = 1.19×10-3 kg/s		Re=250, $\dot{m}_{in}$ =1.98×10-3 kg/s		Re=400, $\dot{m}_{in}$ = 3.17×10-3 kg/s	
		10^{-3} kg/s	%	10^{-3} kg/s	%	10^{-3} kg/s	%
L₂/D=2.50	$\dot{m}_{st}$	0.07	5.88	0.12	6.06	0.26	8.20
	$\dot{m}_{by}$	1.12	94.12	1.86	93.94	2.91	91.80
L₂/D=2.67	$\dot{m}_{st}$	0.07	5.88	0.11	5.56	0.20	6.31
	$\dot{m}_{by}$	1.12	94.12	1.87	94.44	2.97	93.69
L₂/D=3.33	$\dot{m}_{st}$	0.07	5.88	0.12	6.06	0.21	6.62
	$\dot{m}_{by}$	1.12	94.12	1.86	93.94	2.96	93.38
L₂/D=4.00	$\dot{m}_{st}$	0.08	6.72	0.13	6.57	0.22	6.94
	$\dot{m}_{by}$	1.11	93.28	1.85	93.43	2.95	93.06
L₂/D=5.00	$\dot{m}_{st}$	0.09	7.56	0.14	7.07	0.24	7.57
	$\dot{m}_{by}$	1.10	92.44	1.84	92.93	2.93	92.43
L₂/D=6.00	$\dot{m}_{st}$	0.10	8.40	0.16	8.08	0.25	7.89
	$\dot{m}_{by}$	1.09	91.60	1.82	91.92	2.92	92.11
L₂/D=6.67	$\dot{m}_{st}$	0.10	8.40	0.16	8.08	0.26	8.20
	$\dot{m}_{by}$	1.09	91.60	1.82	91.92	2.91	91.80

Table 12. Resistance R values for S = 50%. [Ref. 7.5]

	L₂/D	Δp/L [Pa]	$\dot{m}_{st}$ 10^{-3} [kg/s]	$\dot{m}_{by}$ 10^{-3} [kg/s]	R_{st} [Pa s / kg]	R_{by} [Pa s / kg]
	2.50	109.55	0.33	0.86	331970	127380
	2.67	109.46	0.35	0.84	312740	130310
	3.33	106.73	0.39	0.80	273670	133410
Re=150	4	102.42	0.41	0.78	249800	131310
	5	98.09	0.44	0.75	222930	130790
	6	91.71	0.46	0.73	199370	125630
	6.67	87.41	0.48	0.71	182100	123110
	2.50	202.39	0.57	1.41	355070	143540
	2.67	200.07	0.60	1.38	333450	144980
	3.33	197.79	0.64	1.34	309050	147600
Re=250	4	191.77	0.67	1.31	286220	146390
	5	182.89	0.72	1.26	254010	145150
	6	171.38	0.75	1.23	228510	139330
	6.67	162.02	0.76	1.22	213180	132800
	2.50	367.90	0.96	2.21	383230	166470
	2.67	367.90	1.00	2.17	367900	169540
	3.33	356.99	1.03	2.14	346590	166820
Re=400	4	349.56	1.06	2.11	329770	165670
	5	336.80	1.11	2.06	303420	163500
	6	318.20	1.15	2.02	276700	157520
	6.67	302.45	1.18	1.99	256310	151980

Table 13. Resistance R values for S = 75%. [Ref. 7.5]

	L₂/D	Δp/L [Pa]	$\dot{m}_{st}$ 10^{-3} [kg/s]	$\dot{m}_{by}$ 10^{-3} [kg/s]	R_{st} [Pa s / kg]	R_{by} [Pa s / kg]
	2.50	118.50	0.07	1.12	169290	105800
	2.67	119.20	0.07	1.12	170290	106430
	3.33	118.13	0.07	1.12	168760	105470
Re=150	4	117.24	0.08	1.11	146550	105620
	5	115.87	0.09	1.10	128740	105340
	6	114.00	0.10	1.09	114000	104590
	6.67	112.38	0.10	1.09	112380	103100
	2.50	220.58	0.12	1.86	183820	118590
	2.67	219.39	0.11	1.87	199450	117320
	3.33	221.67	0.12	1.86	184720	119180
Re=250	4	219.44	0.13	1.85	168800	118620
	5	218.77	0.14	1.84	156260	118900
	6	217.09	0.16	1.82	135680	119280
	6.67	214.24	0.16	1.82	133900	117710
	2.50	403.70	0.26	2.91	201290	139970
	2.67	402.57	0.20	2.97	201280	135550
	3.33	405.40	0.21	2.96	193050	136960
Re=400	4	403.72	0.22	2.95	183510	136850
	5	403.98	0.24	2.93	168320	137880
	6	408.43	0.25	2.92	163370	139870
	6.67	407.32	0.26	2.91	156660	139970

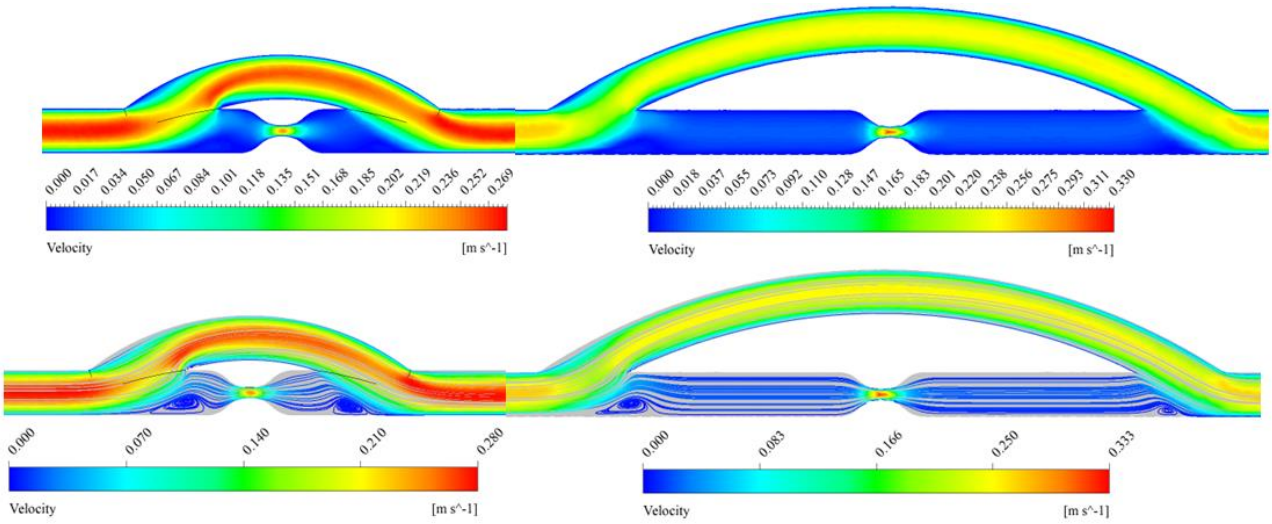

Figure 43. Velocity contours (top) and streamlines (bottom) with reference to a couple of points having coordinates L2/D=6.67, S=75%, Re=150 (right), and L2/D=2.27, S=75%, and Re=150 (left). [Ref. 7.5]

4.4 Conclusions

In this work, it was studied the influence of the bypass attachment point L_2 from the artery stenosis position in different flow condition at fixed value of the junction angle $\alpha = 30°$ and diameter ratio $D_1/D = 1$. Three pressure drop trends for each stenosis degree were created using Constructal Design related to the CFD analysis. The stenosis degree S considered were equal to 50% and 75%. Instead, the Reynolds number Re used were 150, 250 and 400. The results obtained show a decrease in the pressure drop trend as the distance of the bypass attachment point increases. The decreasing pressure trend was less pronounced when S increases. Therefore, the optimum point is the point as far as possible from the shrinkage. It was evaluated the mass flows rate in the various sections of the system. Moreover, the results showed that the flow was all the more diverted in the bypass section when the Reynolds number was more significant. It also computed the resistance flow values in the bypass and stenosis section. It is an alternative formulation for talking about the pressure drop trend.

At this point, some limitations of this study should be mentioned. First of all, a steady-state condition was applied while the blood flow is known to be pulsating. Secondly, the blood was assumed as a Newtonian fluid, which may affect the results found at low Reynolds number. Moreover, the graft and arteries were assumed as rigid walls and idealized without considering a patient-specific vascular model. Besides,

literature does not yet provide many experimental data that are essential for validation and clinical adoption of any proposed configuration.

Despite the simplifications mentioned above and assumptions, by applying Constructal Design methodology, the main conclusions and the optimal graft design found in this paper are following previous studies that evaluated the graft design with other methodologies.

5. Fluid Models Comparison for the Study of the Bypass

The classification of fluids can be performed in two ways: (i) based on the response of an external pressure; (ii) based on the effects produced under the action of a shear force. In the first case, compressible fluids are distinguished from incompressible ones according to whether the volume of an element of fluid depends on the pressure or not. In the case of a gas, compressibility affects the flow characteristics, while a liquid, except in special circumstances, can be considered incompressible and the response to shear forces is of greater importance.

This chapter introduces the fluid models in their entirety, in order to uniquely distinguish the differences between Newtonian fluid and non-Newtonian fluid. Then the different consequences of the application of a non-Newtonian model for the description of the blood flow inside the bypass analyzed in the previous chapters will be analyzed.

5.1 Classification of Fluid Behaviour

5.1.1 Definition of a Newtonian Fluid

Consider a thin fluid layer contained between two parallel planes distant *dy* as shown in Figure 44. If the upper wall is translated in the *x*-direction with a force F, this will be balanced by an equal and opposite internal friction force. For an incompressible Newtonian fluid in laminar flow, the resulting shear stress is equal to the product of the shear rate and the viscosity of the fluid. In this simple case, the shear rate can be expressed as the velocity gradient in the direction perpendicular to that of the shear force, i.e.,

$$\frac{F}{A} = \tau_{yx} = \mu\left(-\frac{dV_x}{dy}\right) = \mu\dot{\gamma}_{yx} \qquad (5.1.1.1)$$

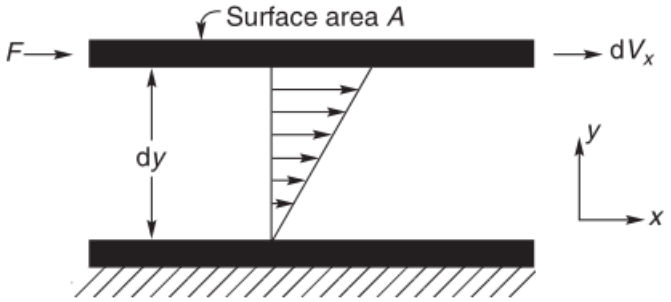

Figure 44. Schematic representation of unidirectional shearing flow. [89]

Note that in Eq.(5.1.1.1) the first subscript on both τ and $\dot{\gamma}$ indicates the direction normal to that of shearing surface, while the second subscript refers to the direction of the force and the flow.

Considering the equilibrium of a fluid element, it can be seen that on each shear plane there are two equal and opposite shear stresses: a positive one that moves slower and a negative one that moves faster. The negative sign in Eq.(5.1.1.1) indicates that τ_{yx} is a measure of the resistance to motion. Considering another point of view , for an incompressible fluid of density ρ, Eq,(5.1.1.1) can be written as:

$$\tau_{yx} = -\frac{\mu}{\rho}\frac{d}{dy}(\rho V_x) \qquad (5.1.1.2)$$

The quantity (ρV_x) is the linear momentum in the *x*-direction per unit volume of the fluid and τ_{yx} represents the momentum flux in the *y*-direction and the negative sign indicates that the momentum transfer occurs in the direction of decreasing velocity.

The constant of proportionality, μ (ratio of the shear stress to the rate of shear) which is called the Newtonian viscosity is, by definition, independent of shear rate ($\dot{\gamma}_{yx}$) or shear stress (τ_{yx}) and depends only on the material and its temperature and pressure.

The “flow curve” or “rheogram” is the plot of shear stress (τ_{yx}) against shear rate ($\dot{\gamma}_{yx}$). For a Newtonian fluid is a straight line of slope, μ, and passing through the origin; the sigle constant, μ, thus completely characterizes the flow behaviour of a Newtonian fluid at fixed temperature and pressure. The shear stress–shear rate data shown in Figure 45 demonstrate the Newtonian fluid behaviour of a cooking oil and a corn syrup; the values of the viscosity for some substances encountered in everyday life are given in Table 14.

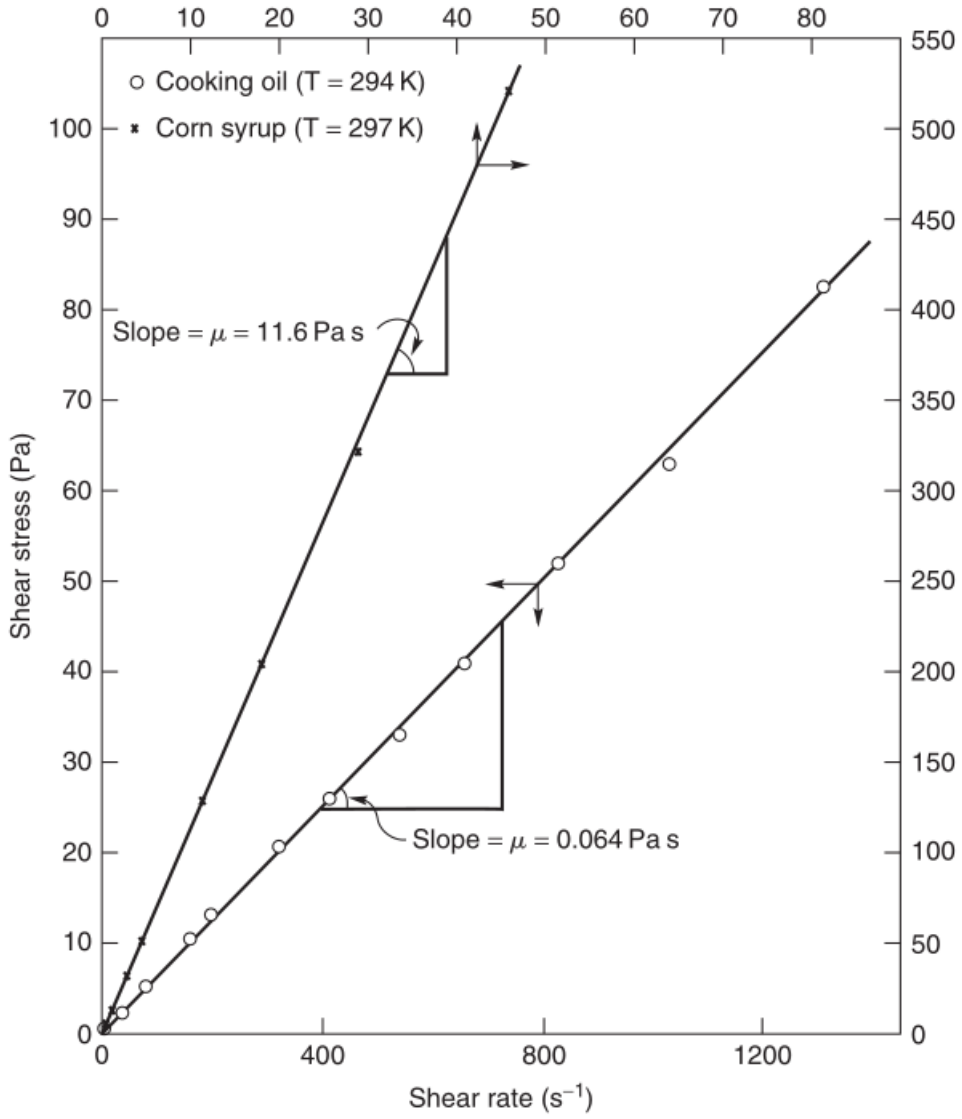

Figure 45. Typical shear stress-shear rate data for a cooking oil and corn syrup [89]

Table 14. Typical viscosity values at room temperature [89]

Substance	μ (mPa s)
Air	10^{-2}
Benzene	0.65
Water	1
Molten sodium chloride (1173 K)	1.01
Ethyl alcohol	1.20
Mercury (293 K)	1.55
Molten lead (673 K)	2.33
Ethylene glycol	20
Olive oil	100
Castor oil	600
100% Glycerine (293 K)	1500
Honey	10^4
Corn syrup	10^5
Bitumen	10^{11}
Molten glass	10^{15}

Figure 44 and Eq.(5.1.1.2) represent the simplest case wherein the velocity vector which has only one component, in the *x*-direction and it varies only in the *y*-direction. Such a flow configuration is known as simple shear flow. For the more complex case of three-dimensional flow, it is necessary to set up the appropriate partial differential equations. For instance, the more general case of an incompressible Newtonian fluid may be expressed - for the *x*-plane (area oriented normal to the *x*-direction) – as follows [87], [88]:

$$\tau_{xx} = -2\mu\frac{\partial V_x}{\partial x} + \frac{2}{3}\mu\left(\frac{\partial V_x}{\partial x} + \frac{\partial V_y}{\partial y} + \frac{\partial V_z}{\partial z}\right) \tag{5.1.1.3}$$

$$\tau_{xy} = -\mu\left(\frac{\partial V_x}{\partial y} + \frac{\partial V_y}{\partial x}\right) \tag{5.1.1.4}$$

$$\tau_{xz} = -\mu\left(\frac{\partial V_x}{\partial z} + \frac{\partial V_z}{\partial x}\right) \tag{5.1.1.5}$$

Figure 46 shows the nine stress components schematically in an element of fluid.

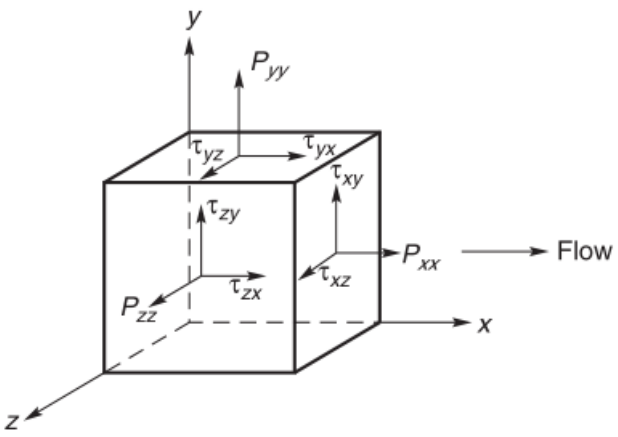

Figure 46. Stress components in three-dimensional flow [89]

By considering the equilibrium of a fluid element, it can be shown that $\tau_{yx} = \tau_{xy}$; $\tau_{xz} = \tau_{zx}$ and $\tau_{yz} = \tau_{zy}$. The normal stresses can be visualized as being made up of two components: isotropic pressure and a contribution due to flow, i.e.,

$$P_{xx} = -p + \tau_{xx} \tag{5.1.1.6}$$

$$P_{yy} = -p + \tau_{yy} \tag{5.1.1.7}$$

$$P_{zz} = -p + \tau_{zz} \tag{5.1.1.8}$$

where τ_{xx}, τ_{yy}, τ_{zz} contributions arising from flow are known as deviatoric normal stresses for Newtonian fluids and as extra stresses for non-Newtonian fluids. For an incompressible Newtonian fluid, the isotropic pressure is given by:

$$p = -\frac{1}{3}\left(P_{xx} + P_{yy} + P_{zz}\right) \tag{5.1.1.9}$$

From Eq.(5.1.1.6) to Eq.(5.1.1.9) it follows that

$$\tau_{xx} + \tau_{yy} + \tau_{zz} = 0 \tag{5.1.1.10}$$

For a Newtonian fluid is simple shearing motion, the deviatoric normal stress components are identically zero, i.e.,

$$\tau_{xx} = \tau_{yy} = \tau_{zz} = 0 \qquad (5.1.1.11)$$

Thus, the complete definition of a Newtonian fluid is that it not only possesses a constant viscosity but it also satisfies the condition of Eq.(5.1.1.11), or simply that it satisfies the complete Navier–Stokes equations. Thus, for instance, the so-called constant viscosity Boger fluids ([89], [90]) which display constant shear viscosity but do not conform to Eq.(5.1.1.11) must be classed as non-Newtonian fluids. A cursory inspection of AAAA reveals the widespread occurrence of non-Newtonian flow behaviour in materials encountered in everyday life as well as in diverse industrial settings.

Table 15. Examples of substances exhibiting non-Newtonian fluid behaviour [89]

- Adhesives (wall paper paste, carpet adhesive, for instance)
- Ales (beer, liqueurs, etc.)
- Animal waste slurries from cattle farms
- Biological fluids (blood, synovial fluid, saliva, etc.)
- Bitumen
- Cement paste and slurries
- Chalk slurries
- Chocolates
- Coal slurries
- Cosmetics and personal care products (nail polish, lotions and creams, lipsticks, shampoos, shaving foams and creams, toothpaste, etc.)
- Dairy products and dairy waste streams (cheese, butter, yogurts, fresh cream, whey, for instance)
- Drilling muds
- Fire fighting foams
- Foodstuffs (fruit/vegetable purees and concentrates, sauces, salad dressings, mayonnaise, jams and marmalades, ice-cream, soups, cake mixes and cake toppings, egg white, bread mixes, snacks)
- Greases and lubricating oils
- Mine tailings and mineral suspensions
- Molten lava and magmas
- Paints, polishes and varnishes
- Paper pulp suspensions
- Peat and lignite slurries
- Polymer melts and solutions, reinforced plastics, rubber
- Printing colours and inks
- Pharmaceutical products (creams, foams, suspensions, for instance)
- Sewage sludge
- Wet beach sand
- Waxy crude oils

5.2.1 Non-Newtonian Fluid behaviour

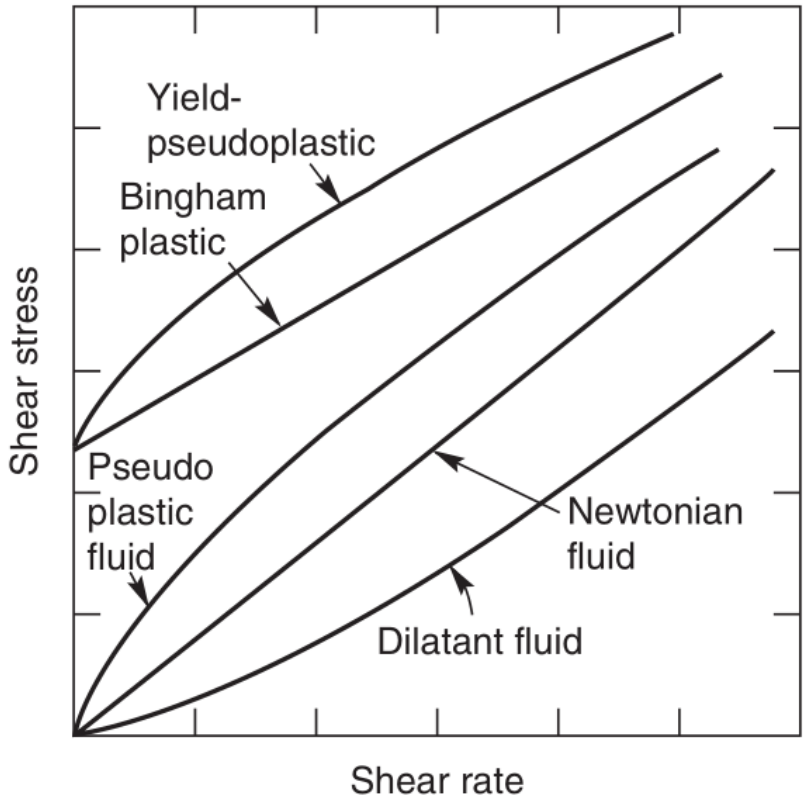

Figure 47. Types of time-independent flow behaviour [89]

A non-Newtonian fluid is one whose flow curve (shear stress versus shear rate) is non linear or does not pass through the origin (Figure 47), i.e. where the apparent viscosity, shear stress divided by shear rate, is not constant at a given temperature and pressure but is dependent on flow conditions such as flow geometry, shear rate, etc. and sometimes even on the kinematic history of the fluid element under consideration. Such materials may be conveniently grouped into three general classes:

1) Fluids for which the rate of shear at any point is determined only by the value of the shear stress at that point at that instant; these fluids are variously known as “time independent”, “purely viscous”, “inelastic” or “generalized Newtonian fluids” (GNF).
2) More complex fluids for which the relation between shear stress and shear rate depends, in addition, upon the duration of shearing and their kinematic history; they are called “time-dependent fluids”.

3) Substances exhibiting characteristics of both ideal fluids and elastic solids and showing partial elastic recovery, after deformation; these are categorized as "visco-elastic fluids".

This classification scheme is arbitrary in that most real materials often exhibit a combination of two or even all three types of non-Newtonian features. Generally, it is, however, possible to identify the dominant non-Newtonian characteristic and to take this as the basis for the subsequent process calculations. Also, as mentioned earlier, it is convenient to defi ne an apparent viscosity of these materials as the ratio of shear stress to shear rate, though the latter ratio is a function of the shear stress or shear rate and/or of time.

There are many types and models for the description of non-Newtonian fluids; for our purpose we consider the non-Newtonian fluid models used to describe the rheological behaviour of blood.

5.1.2.1 Time-Independent

In simple shear, the flow behaviour of this class of materials may be described by a constitutive relation of the form

$$\dot{\gamma}_{yx} = f(\tau_{yx}) \tag{5.1.2.1.1}$$

or its inverse form,

$$\tau_{yx} = f_1(\dot{\gamma}_{yx}) \tag{5.1.2.1.2}$$

This equation implies that the value of $\dot{\gamma}_{yx}$ at any point within the sheared fluids is determined only by the current value of shear stress at that point or vice cersa. Depending upon the form of the function in Eq.(5.1.2.1.1) or Eq.(5.1.2.1.2), these fluids may be further subdivided into three types:

a) Shear-thinning or pseudoplastic

b) Viscoplastic

c) Shear-thickening or dilatant.

Qualitative flow curves on linear scales for these three types of fluid behaviour are shown in Figure 47; the linear relation typical of Newtonian fluids is also included.

The most common type of time-independent non-Newtonian fluid behavior observed is pseudoplasticity or shear-thinning, characterized by an apparent viscosity which decreases with increasing shear rate. Both at very low and at very high shear rates, most shear-thinning polymer solutions and melts exhibit Newtonian behavior, i.e., shear stress–shear rate plots become straight lines, as shown schematically in Figure 48, and on a linear scale will pass through origin. The resulting values of the apparent viscosity at very low and high shear rates are known as the zero shear viscosity, μ_0, and the infinite shear viscosity, μ_∞, respectively.

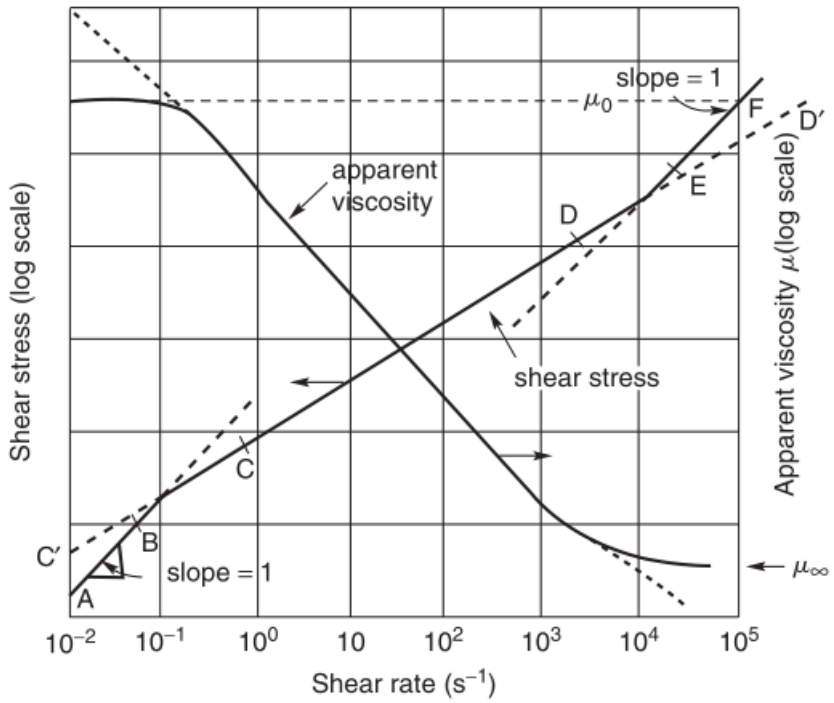

Figure 48. Schematic representation of shear-thinning behaviour [89]

Thus, the apparent viscosity of a shear-thinning fluid decreases from μ_0 to μ_∞ with increasing shear rate. Data encompassing a sufficiently wide range of shear rates to illustrate this complete spectrum of pseudoplastic behaviour are difficult to obtain, and are scarce. A single instrument will not have both the sensitivity required in the low

shear rate region and the robustness at high shear rates, so that several instruments are often required to achieve this objective. Figure 49 shows the apparent viscosity - shear rate behaviour of an aqueous polyacrylamide solution at 293 K over almost seven decades of shear rate. The apparent viscosity of this solution drops from 1400 mPa s to 4.2 mPa s, and so it would hardly be justifiable to assign a single average value of viscosity for such a fluid!

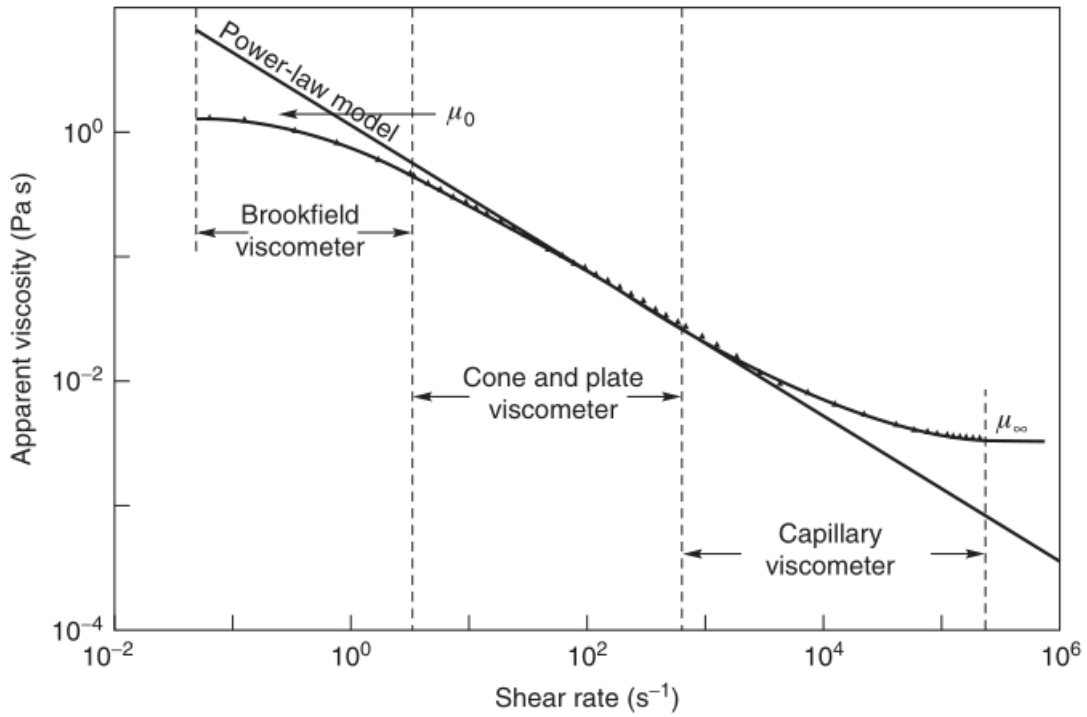

Figure 49. Demonstration of zero shear and infinity shear viscosities for a shear-thinning polymer solution [89]

The values of shear rates marking the onset of the upper and lower limiting viscosities are dependent upon several factors, such as the type and concentration of polymer, its molecular weight distribution and the nature of solvent, etc. Hence, it is difficult to suggest valid generalizations but many materials exhibit their limiting viscosities at shear rates below 10^{-2} s^{-1} and above 10^5 s^{-1}, respectively. Generally, the range of shear rate over which the apparent viscosity is constant (in the zero-shear region) increases as molecular weight of the polymer falls, as its molecular weight distribution becomes narrower, and as polymer concentration (in solution) drops. Similarly, the rate of decrease of apparent viscosity with shear rate also varies from

one material to another, as can be seen in Figure 50 for three aqueous solutions of chemically different polymers.

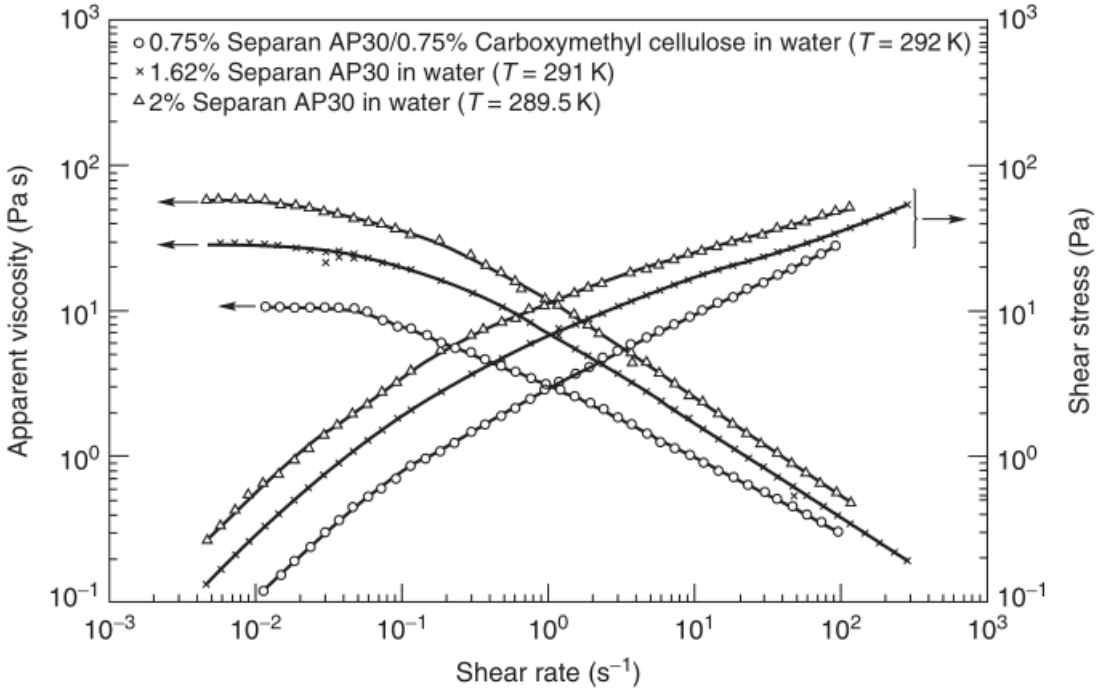

Figure 50. Representative shear stress and apparent viscosity plots for three pseudo-plastic polymer solutions. [89]

MATHEMATICAL MODELS FOR SHEAR-THINNING FLUID BEHAVIOUR

Many mathematical expressions of varying complexity and form have been proposed in literature to model shear-thinning characteristics; some of these are straightforward attempts at curve fitting, giving empirical relationships for the shear stress (or apparent viscosity) - shear rate curves for example, while others have some theoretical basis in statistical mechanics – as an extension of the application of the kinetic theory to the liquid state or the theory of rate processes, etc. Only a selection of the most commonly used viscosity models for describing blood is provided here; more complete descriptions of other models are available in many books ([87], [91]) and in review paper [92].

(a) The power-law or Ostwald de Waele model

The relationship between shear stress and shear rate (plotted on double logarithmic coordinates) for a shear-thinning fluid can often be approximated by a straight line over a limited range of shear rate (or stress). For this part of the flow curve, an expression of the following form is applicable:

$$\tau_{yx} = m\left(\dot{\gamma}_{yx}\right)^{n} \qquad (5.1.2.1.3)$$

so the apparent viscosity for the so-called power-law fluid is thus given by:

$$\mu = \frac{\tau_{yx}}{\dot{\gamma}_{yx}} = m\left(\dot{\gamma}_{yx}\right)^{n-1} \qquad (5.1.2.1.4)$$

For $n<1$ the fluid exhibits shear-thinning properties; for $n=1$ the fluid shows Newtonian behaviour, and for $n>1$ the fluid shows shear-thickening behaviour.

In these equations, m and n are two empirical curve-fitting parameters and are known as the fluid consistency coefficient and the flow behaviour index respectively. For a shear-thinning fluid, the index may have any value between 0 and 1. The smaller the value of *n*, the greater is the degree of shear-thinning. For a shear-thickening fluid, the index *n* will be greater than unity. When $n=1$, Eq. (5.1.2.1.3) and Eq. (5.1.2.1.4) reduce to Eq. (5.1.1.2) which describes Newtonian fluid behaviour.

Although the power-law model offers the simplest representation of shear-thinning behaviour, it does have a number of shortcomings. Generally, it applies over only a limited range of shear rates and therefore the fitted values of *m* and *n* will depend on the range of shear rates considered. Furthermore, it does not predict the zero and infinite shear viscosities, as shown by dotted lines in Figure 48. Finally, it should be noted that the dimensions of the flow consistency coefficient, *m*, depend on the numerical value of *n* and therefore the m values must not be compared when the *n* values differ. On the other hand, the value of *m* can be viewed as the value of apparent

viscosity at the shear rate of unity and will therefore depend on the time unit (e.g. second, minute or hour) employed. Despite these limitations, this is perhaps the most widely used model in the literature dealing with process engineering applications. Finally, while each non-Newtonian fluid is unique and its rheological behaviour must be evaluated directly, Table 16 provides a compilation of the power-law constants (m and n) for a variety of substances. It needs to be emphasized here that these values are provided here to give the readers a feel for their values.

Table 16. Typical values of power-law constants for a few systems. [89]

System	Temperature (K)	n (−)	m (Pa s^n)
Agro- and food-related products			
Aerated poultry waste slurry (x is % volume of solids)	283–298	1.81–0.161 ln x	1.12×10^{-11} $(x)^{2.59}$
Ammonium alginate solution (3.37%)	297	0.5	13
Apple butter	–	0.15	200
Apple sauce	300	0.3–0.45	12–22
Apricot puree	300	0.3–0.4	5–20
Banana puree	293–315	0.33–0.5	4–10
Carrot puree	298	0.25	25
Chicken (minced)	296	0.10	900
Chocolate	303	0.5	0.7
Guava puree	296.5	0.5	40
Human blood	300	0.9	0.004
Mango pulp	300–340	0.3	3–10
Marshmallow cream	–	0.4	560
Mayonnaise	298	0.6	5–100
Papaya puree	300	0.5	10
Peach puree	300	0.38	1–5
Peanut butter	–	0.07	500
Pear puree	300	0.4–0.5	1–5
Plum puree	287	0.35	30–80
Tomato concentrate (5.8% solid)	305	0.6	0.22
Tomato ketch up	295	0.24	33
Tomato paste	–	0.5	15
Whipped desert toppings	–	0.12	400
Yoghurt	293	0.5–0.6	25
Polymer melts			
High density polyethylene (HDPE)	453–493	0.6	$3.75–6.2 \times 10^3$
High impact polystyrene	443–483	0.20	$3.5–7.5 \times 10^4$
Polystyrene	463–498	0.25	$1.5–4.5 \times 10^4$
Polypropylene	453–473	0.40	$4.5–7 \times 10^3$
Low density polyethylene (LDPE)	433–473	0.45	$4.3–9.4 \times 10^3$
Nylon	493–508	0.65	$1.8–2.6 \times 10^3$
Polymethylmethyacrylate (PMMA)	493–533	0.25	$2.5–9 \times 10^4$
Polycarbonate	553–593	0.65–0.8	$1–8.5 \times 10^3$
Personal care products			
Nail polish	298	0.86	750
Mascara	298	0.24	200
Toothpaste	298	0.28	120
Sunscreen lotions	298	0.28	75
Ponds cold cream	298	0.45	25
Oil of Olay	298	0.22	25

(b) The Carreau viscosity equation

When there are significant deviations from the power-law model at very high and very low shear rates as shown in Figure 49, it is necessary to use a model which takes account of the limiting values of viscosity μ_0 and μ_∞.

Based on the molecular network considerations, Carreau [93] put forword the following viscosity model which incorporates both limiting viscosities μ_0 and μ_∞:

$$\frac{\mu - \mu_\infty}{\mu_0 - \mu_\infty} = \left[1 + \left(\lambda \dot{\gamma}_{yx}\right)^2\right]^{(n-1)/2} \qquad (5.1.2.1.5)$$

where *n* and λ are two curve-fitting parameters. This model can describe shear-thinning behaviour over wide ranges of shear rates but only at the expense of the added complexity of four parameters. This model predicts Newtonian fluid behaviour $\mu = \mu_0$ when either *n=1* or λ=0 or both.

The *Cross viscosity model* and the *Ellis fluid model* also fall into the *Shear-thinning fluid family*, but in literature these models are not commonly used for the description of blood, therefore they are not reported here, but they are widely evaluable in the literature [94].

To conclude the description of the time-independent fluids, the viscoplastic models and the dilating models are briefly illustrated.

The viscoplastic type of fluid behaviour is characterized by the existence of a yield stress (τ_0) which must be exceeded before the fluid will deform or flow. Conversely, such a material will deform elastically (or flow en masse like a rigid body) when the externally applied stress is smaller than the yield stress. Once the magnitude of the external stress has exceeded the value of the yield stress, the flow curve may be linear or non-linear but will not pass through origin (Figure 47). Hence, in the absence of surface tension effects, such a material will not level out under gravity to form an

absolutely flat free surface. One can, however, explain this kind of fluid behaviour by postulating that the substance at rest consists of three-dimensional structures of sufficient rigidity to resist any external stress less than τ_0. For stress levels greater than τ_0, however, the structure breaks down and the substance behaves like a viscous material. In some cases, the build-up and breakdown of structure has been found to be reversible, i.e., the substance may regain its initial value of the yield stress.

A fluid with a linear flow curve for $|\tau_{yx}| > |\tau_0|$ is called Bingham plastic fluid and is characterized by a constant plastic viscosity and a yield stress. On the other hand, a substance possessing a yield stress as well as non-linear flow curve on linear coordinates (for $|\tau_{yx}| > |\tau_0|$), is called "yield-pseudoplastic" material. Figure 51 illustrate viscoplastic behaviour as observed in a meat extract an in a polymer solution.

It is interesting to note that a viscoplastic material also display an apparent viscosity which decreases with increasing shear rate. At very low shear rates, the apparent viscosity is effectively infinite at the instant immediately before the substance yields and begins to flow. It is thus possible to regard these materials as possessing a particular class of shear-thinning behaviour.

The mathematical models for viscoplastic fluids are:

1) The Bingham plastic model;
2) The Herschel-Bulkley fluid model;
3) The Casson fluid model.

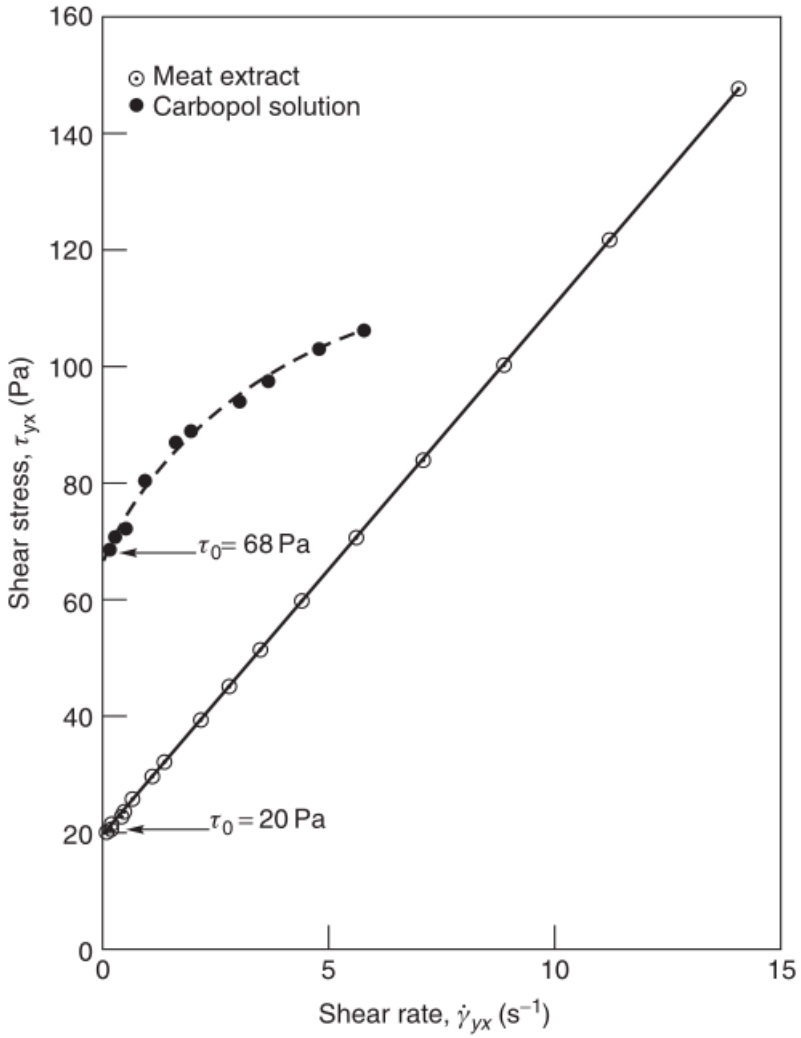

Figure 51. Representative stress-shear rate data showing viscoplastic behaviour in a meat extract (Bingham plastic) and in an aqueous Carbopol polymer solution (yeld-pseudoplastic). [89]

Dilatant fluids are similar to pseudoplastic systems in that they show no yield stress but their apparent viscosity increases with increasing shear rate; thus these fluids are also called shear-thickening. This type of fluid behaviour was originally observed in concentrated suspensions and a possible explanation for their dilatant behaviour is as follows: at rest, the voidage is minimum and the liquid present is sufficient to fill the void space. At low shear rates, the liquid lubricates the motion of each particle past others and the resulting stresses are consequently small. At high shear rates, on the other hand, the material expands or dilates slightly (as also observed in the transport of sand dunes) so that there is no longer sufficient liquid to fill the increased void space and prevent direct solid–solid contacts which result in increased friction and higher

shear stresses (as shown schematically in Figure 52). This mechanism causes the apparent viscosity to rise rapidly with increasing rate of shear.

The term dilatant has also been used for all other fluids which exhibit increasing apparent viscosity with increasing rate of shear. Many of these, such as starch pastes, are not true suspensions and show no dilation on shearing. The above explanation therefore is not applicable but nevertheless such materials are still commonly referred to as dilatant fluids.

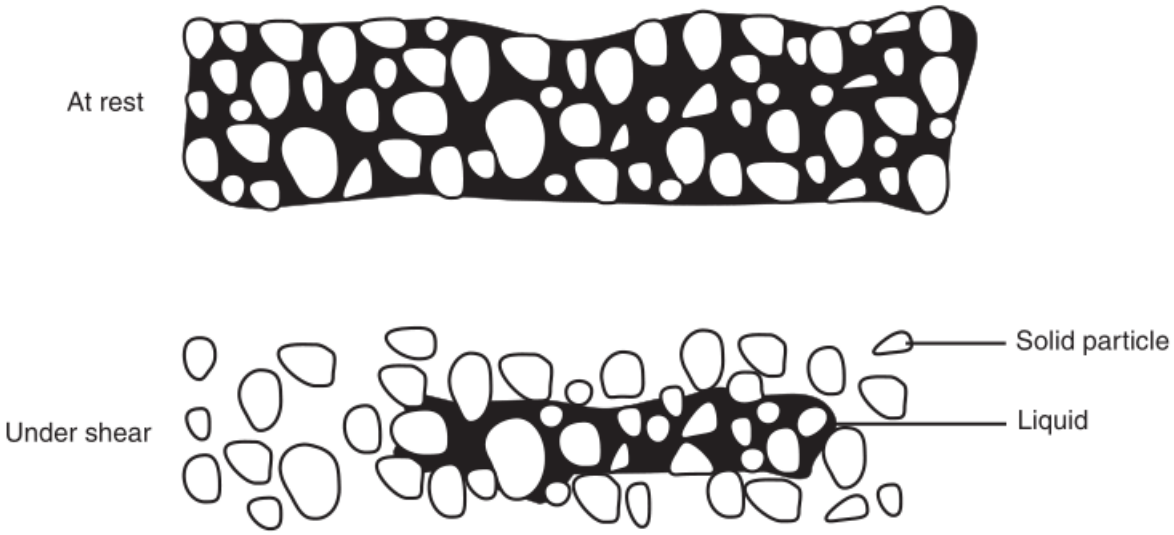

Figure 52. Schematic representation of shear-thickening behaviour. [89]

Of the time-independent fluids, this sub-class has received very little attention; consequently very few reliable data are available. Until recently, dilatant fluid behaviour was considered to be much less widespread in the chemical and processing industries.

The limited information reported so far suggests that the apparent viscosity–shear rate data often result in linear plots on double logarithmic coordinates over a limited shear rate and the flow behaviour may be represented by the power-law model, Eq.(5.1.2.1.6), with the flow behaviour index, *n*, greater than unity, i.e.,

$$\mu = m\left(\dot{\gamma}_{yx}\right)^{n-1} \qquad (5.1.2.1.6)$$

One can readily see that for *n>1*, Eq. (5.1.2.1.6) predicts increasing viscosity with increasing shear rate. The dilatant behaviour may be observed in moderately concentrated suspensions at high shear rates, and yet, the same suspension may exhibit pseudo-plastic behaviour at lower shear rates, as shown in Figure 53; it is not yet possible to ascertain whether these materials also display limiting apparent viscosities.

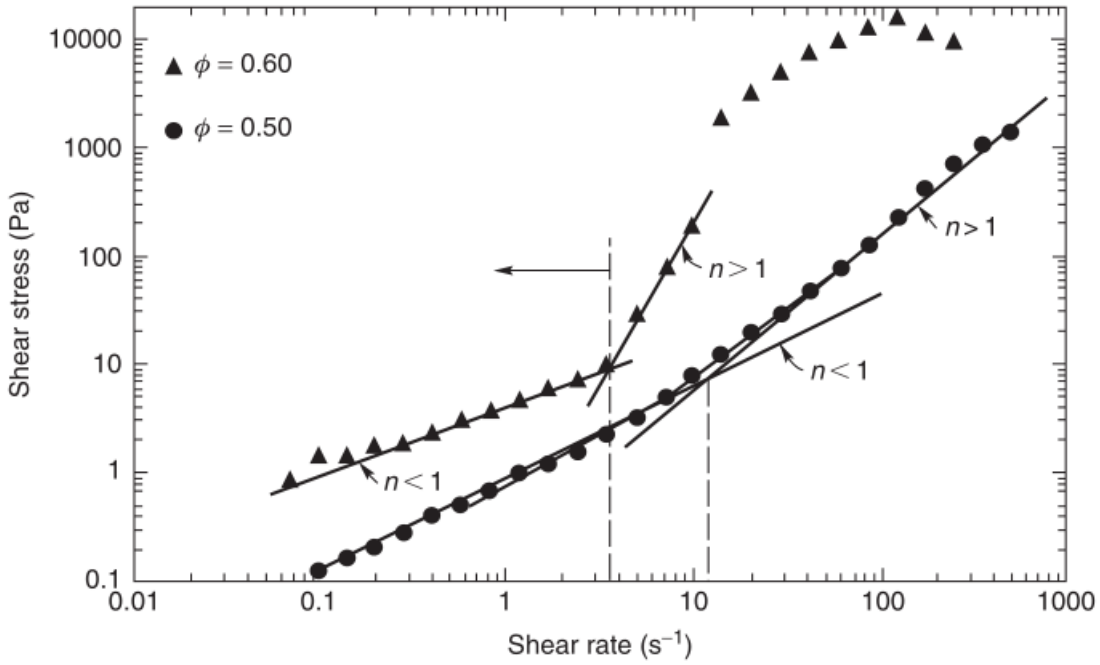

Figure 53. Shear stress-shear rate behaviour of polyvinylchloride (PVC) in dioctylphthalate (DOP) dispersion at 298 K showing regions of shear-thinning and shear-thickening [95].

5.2 Comparison of Different Bypass Fluid Models

For the comparison study between the different fluid models, the transient case in which the inlet velocity was considered pulsed was numerically solved (Appendix A). The conditions of the simulations are the same as in the pulsed regime case of chapter 3. Referring to the models most commonly used in literature, we want to justify that the use of the Newtonian model is a valid approximation also in this case. Therefore, the model compered are: (i) Newtonian, (ii) Power-Law and (iii) Carreau models. The validity of the approximation is justified both through the study of the flow field and through the analysis of cyclic stresses. Table 17 summarizes the values of the properties used in the simulations for the different models.

Table 17. Property values used in simulations for different models. [Ref. 7.1]

	Newtonian	**Power Law**	**Carreau**
ρ [kg/m^3]	1060	1060	1060
μ [$Pa\ s$]	3.45*10^{-3}	-	-
k	-	0.017	-
a	-	-	2
n	-	0.708	0.2128
λ	-	-	3.313005
μ_0 [$Pa\ s$]	-	-	0.056
μ_∞ [$Pa\ s$]	-	-	0.0035

The validation of the numerical model was performed using the Grid Convergence Index (GCI) method considering the Newtonian blood fluid to compere the results with Vimmr et al. [35].

The grid quality tests were conducted for the cases shown in Table 18, where N_i is the number of mesh elements and ($\tilde{p}_{N_i}^{4T}$) is the Root Mean Square value of the pressure drop measured in the fourth cardiac cycle.

As explained by Celik et al. [68], this method is useful for calculating and reporting discretization error estimates in CFD simulations. It is important to observe that the method considers, based on experience rather than formal derivation, a GCI value until 5% as acceptable (Celik et al. [68]). In this case the maximum GCI value is 2.52%. This ensures an acceptable mesh quality for all simulations as this value is less than 5%.

Figure 54 illustrates the meshes valid for the calculation, i.e. those corresponding to N3 in the Table 3.

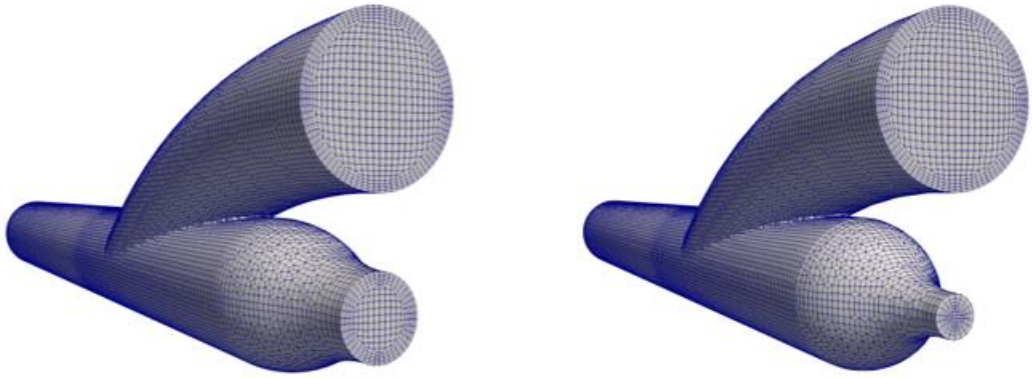

Figure 54. Mesh sectional view. Stenosis degree 50% on the left and stenosis degree 75% on the right. [Ref. 7.1]

In Table 19 it is represented the error of the measure of the Root Mean Square from the relative cycle. The relative error is computed from Eq.(5.2.1).

$$\varepsilon_{(i+1),i}\% = \frac{\left|\tilde{p}_{(i+1)T} - \tilde{p}_{iT}\right|}{\tilde{p}_{(i+1)T}} 100, \quad i = 1,2,3 \tag{5.2.1}$$

The pressure errors evaluated in the fourth cycle are the order of $10^{-6}\%$, which is acceptable as an approximation.

In order to have a further validation of the mesh models used and the relative numerical setting, the data of Vimmr *et al.* [35] were used as input data (Newtonian fluid described in Table 17) to compare the velocity field in two section of the geometry. The results were represented in Figure 55. It is noted that the velocity

differences are minimal and due to the different meshes used compared to Vimmr *et al.* [35]. For this reason, the meshes used can be validated.

Table 18. Grid Convergence Index (GCI) for different bypass configurations. [Ref. 7.1]

	S=50%	***S=75%***
N_1	115239	113832
N_2	221972	219901
N_3	427584	426428
$\widetilde{\boldsymbol{p}}_{\boldsymbol{N_1}}^{\boldsymbol{4T}}$ $[\boldsymbol{Pa}]$	0.1138141973	0.1238977365
$\widetilde{\boldsymbol{p}}_{\boldsymbol{N_2}}^{\boldsymbol{4T}}$ $[\boldsymbol{Pa}]$	0.1128971193	0.1225465280
$\widetilde{\boldsymbol{p}}_{\boldsymbol{N_3}}^{\boldsymbol{4T}}$ $[\boldsymbol{Pa}]$	0.1122418939	0.1222117354
GCI	**2.5203%**	**0.4490%**

Table 19. Relative error $\varepsilon_{(i+1),i}$ from the cardiac cycle (i+1) to the cycle i in dimensional and non-dimensional format. [Ref. 7.1]

	S=50%	***S=75%***
$\widetilde{\boldsymbol{p}}_{\boldsymbol{1T}}$ $[\boldsymbol{Pa}]$	0.1122829233	0.1222636913
$\widetilde{\boldsymbol{p}}_{\boldsymbol{2T}}$ $[\boldsymbol{Pa}]$	0.1122418444	0.1222117059
$\widetilde{\boldsymbol{p}}_{\boldsymbol{3T}}$ $[\boldsymbol{Pa}]$	0.1122418914	0.1222117833
$\widetilde{\boldsymbol{p}}_{\boldsymbol{4T}}$ $[\boldsymbol{Pa}]$	0.1122418939	0.1222117354
$\boldsymbol{\varepsilon_{2,1}}$%	$3.65985 \cdot 10^{-2}$	$4.25372 \cdot 10^{-2}$
$\boldsymbol{\varepsilon_{3,2}}$%	$4.18653 \cdot 10^{-5}$	$6.33594 \cdot 10^{-5}$
$\boldsymbol{\varepsilon_{4,3}}$%	$2.24951 \cdot 10^{-6}$	$3.91521 \cdot 10^{-6}$

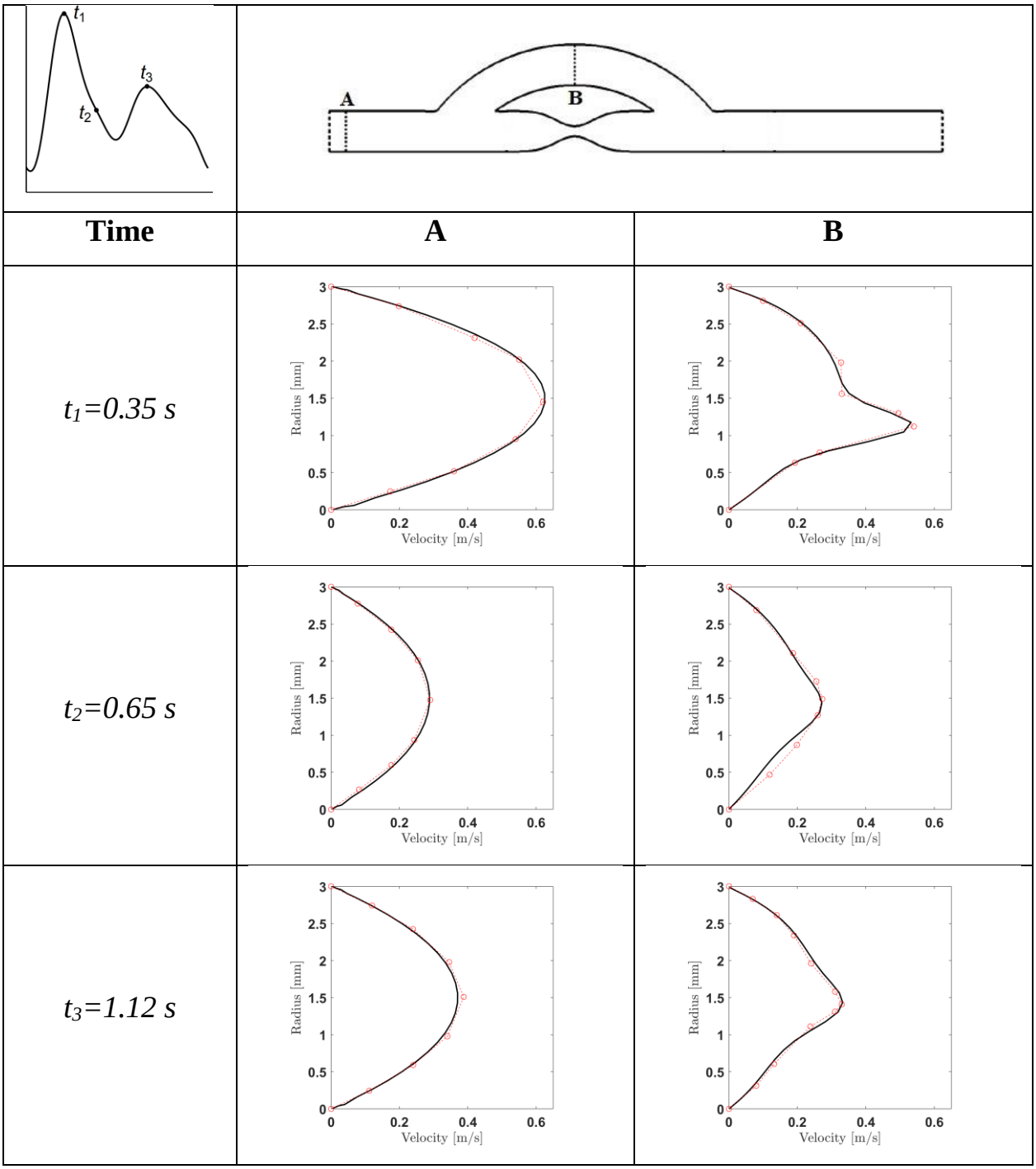

Figure 55. Comparison of the velocity profiles in the inlet (A) and bypass (B) sections for different values of time-steps (t_1, t_2 and t_3) with the results of Vimmr *et al.* [35] (red line) in the case of stenosis degree $S=75\%$, junction angle $\alpha=30°$, diameter ratio $D/d=1$ and Newtonian fluid with density $\rho=1060\ kg\ m^{-3}$ and dynamic viscosity $\mu=3.45*10^{-3}\ Pa\ s$. [Ref. 7.1]

5.2.1 Results

with the aim of comparing the results of the different numerical models, the velocity results were analyzed in three different forms. First, the 3D velocity results were analyzed in order to capture the three-dimensional behavior of the flow (Figure 56, Figure 57 and Figure 58). Second, the velocity contours on the geometry cross section were examined in order to make the flow field more visible by identifying the flow recirculation areas (Figure 59, Figure 60 and Figure 61). Third, 2D velocity plots profiles on specific geometries sections were analyzed in order to make the difference between the models clearer (Figure 62 and Figure 63).

To determine the intensity of shear oscillations, the well-known oscillatory shear index (OSI) is introduced according to the study of He and Ku [96]

$$OSI = \frac{1}{2}\left(1 - \frac{\left|\int_0^T \boldsymbol{\tau}_W \, dt\right|}{\int_0^T |\boldsymbol{\tau}_W| \, dt}\right), \tag{5.2.1.1}$$

where $\boldsymbol{\tau}_W$ is the Wall Shear Stress (WSS) vector and T is the period of the cardiac cycle. The OSI values range from *0* to *0.5*. The time used to calculate the OSI field is the one referred to the last cardiac cycle of the simulation, that is the period that goes from *3T* to *4T* in order to consider the effect in the steady-state flow zone.

Figure 64 shows the OSI fields in the perspective views of the two geometries (*S = 50%* and *S = 75%*) for the different fluid models. It is easy to notice that the Power Law model, due to its velocity profile, differs a lot from the other models and the OSI values are almost zero. The Newtonian model and that of Carreau, on the other hand, are comparable and the differences are almost minimal. It is noted that the accentuated values of OSI occur in the fluid recirculation areas and in the junctions between the bypass and the main vein.

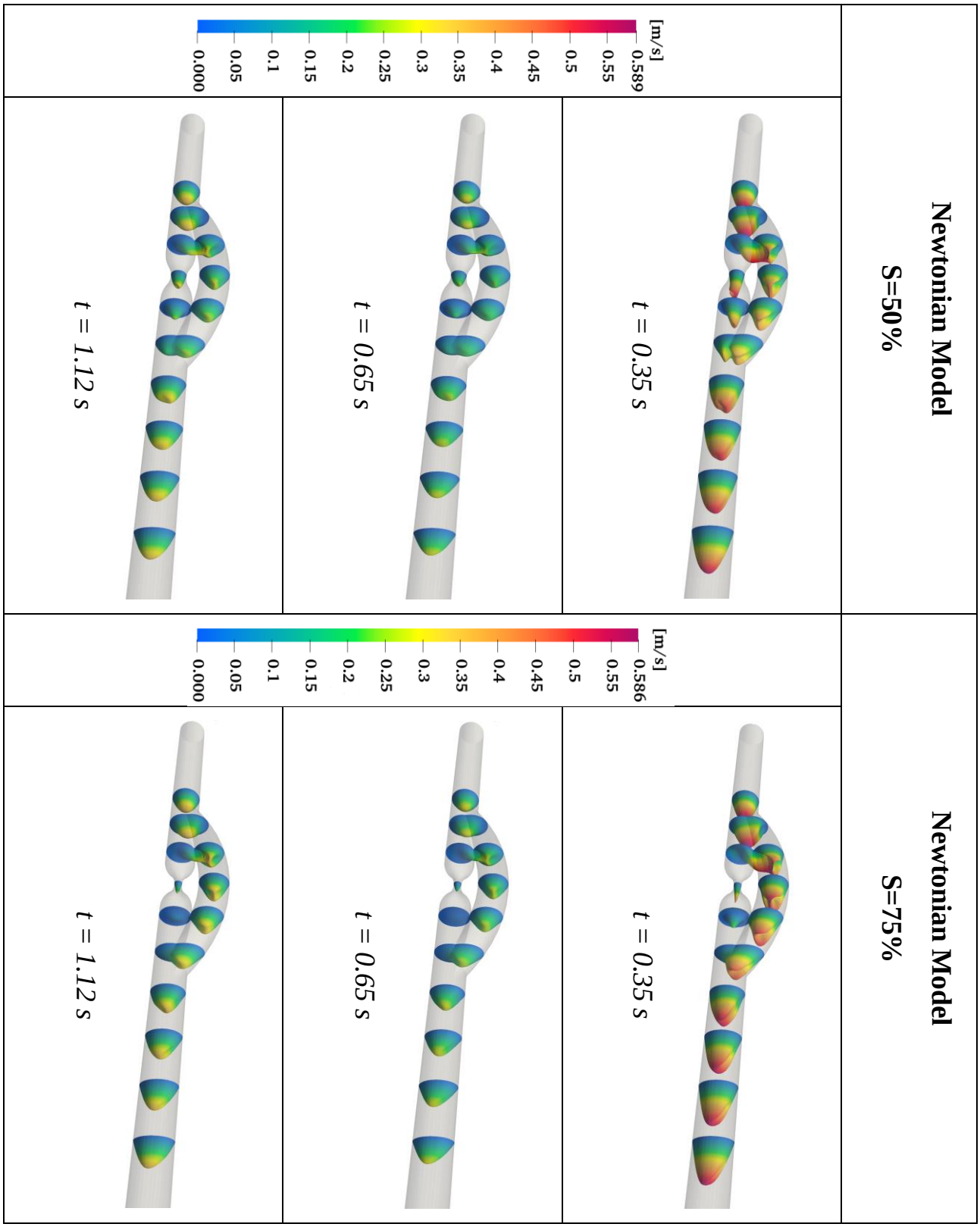

Figure 56. 3D velocity profiles for Newtonian model at different time steps for both stenosis degree (*S=50%* and *S=75%*) [Ref. 7.1]

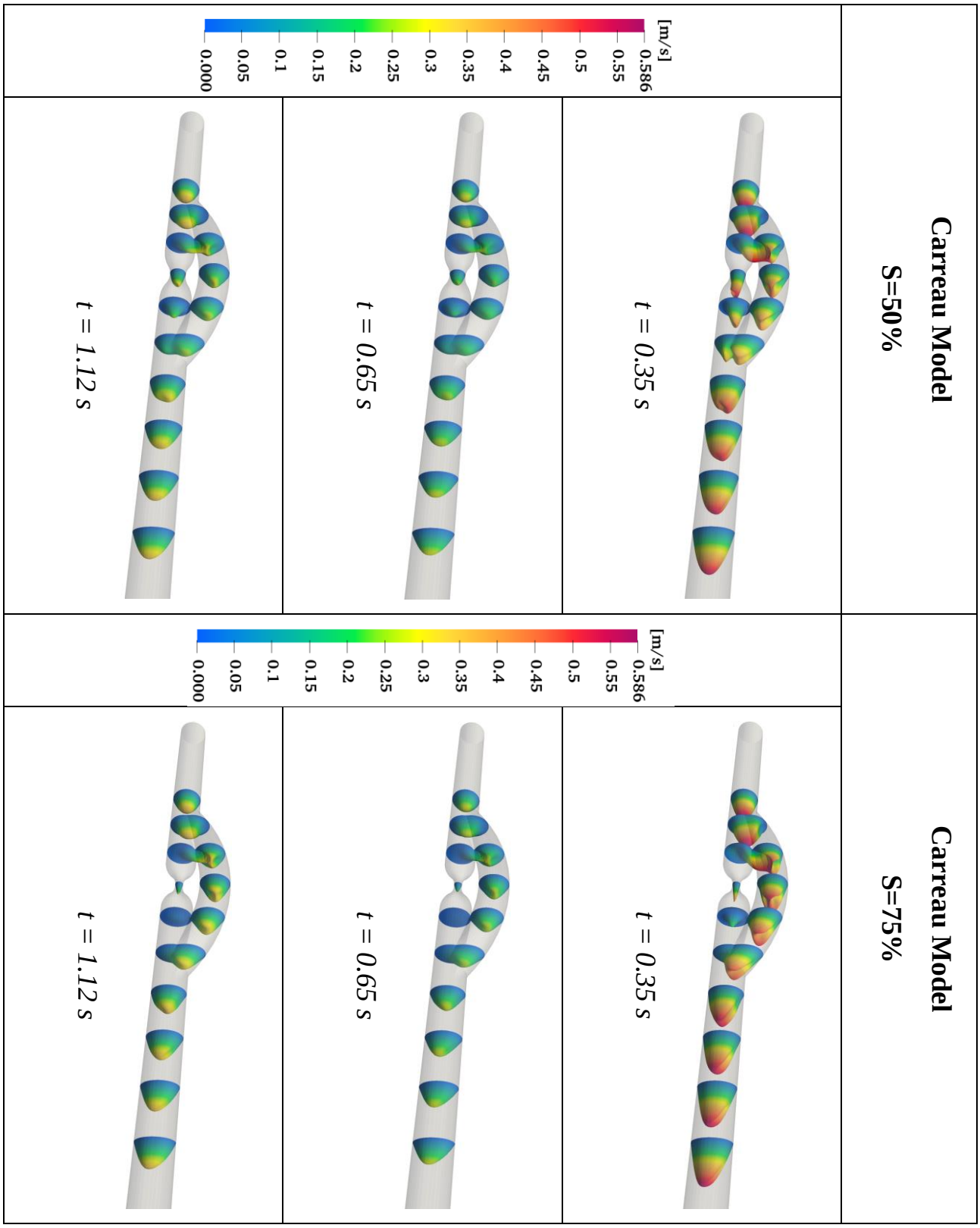

Figure 57. 3D velocity profiles for Carreau model at different time steps for both stenosis degree (*S=50%* and *S=75%*) [Ref. 7.1]

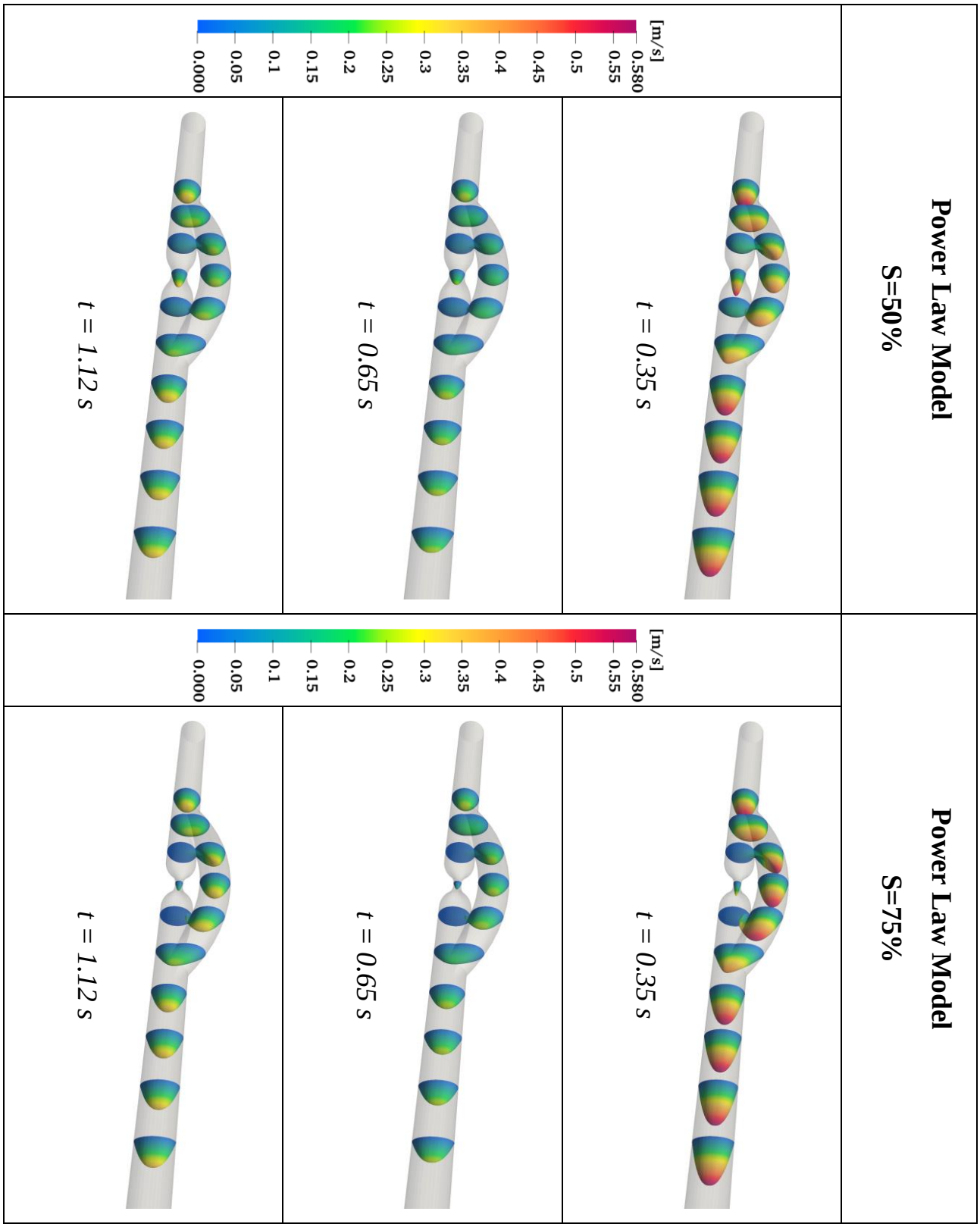

Figure 58. 3D velocity profiles for Power Law model at different time steps for both stenosis degree (S=50% and S=75%) [Ref. 7.1]

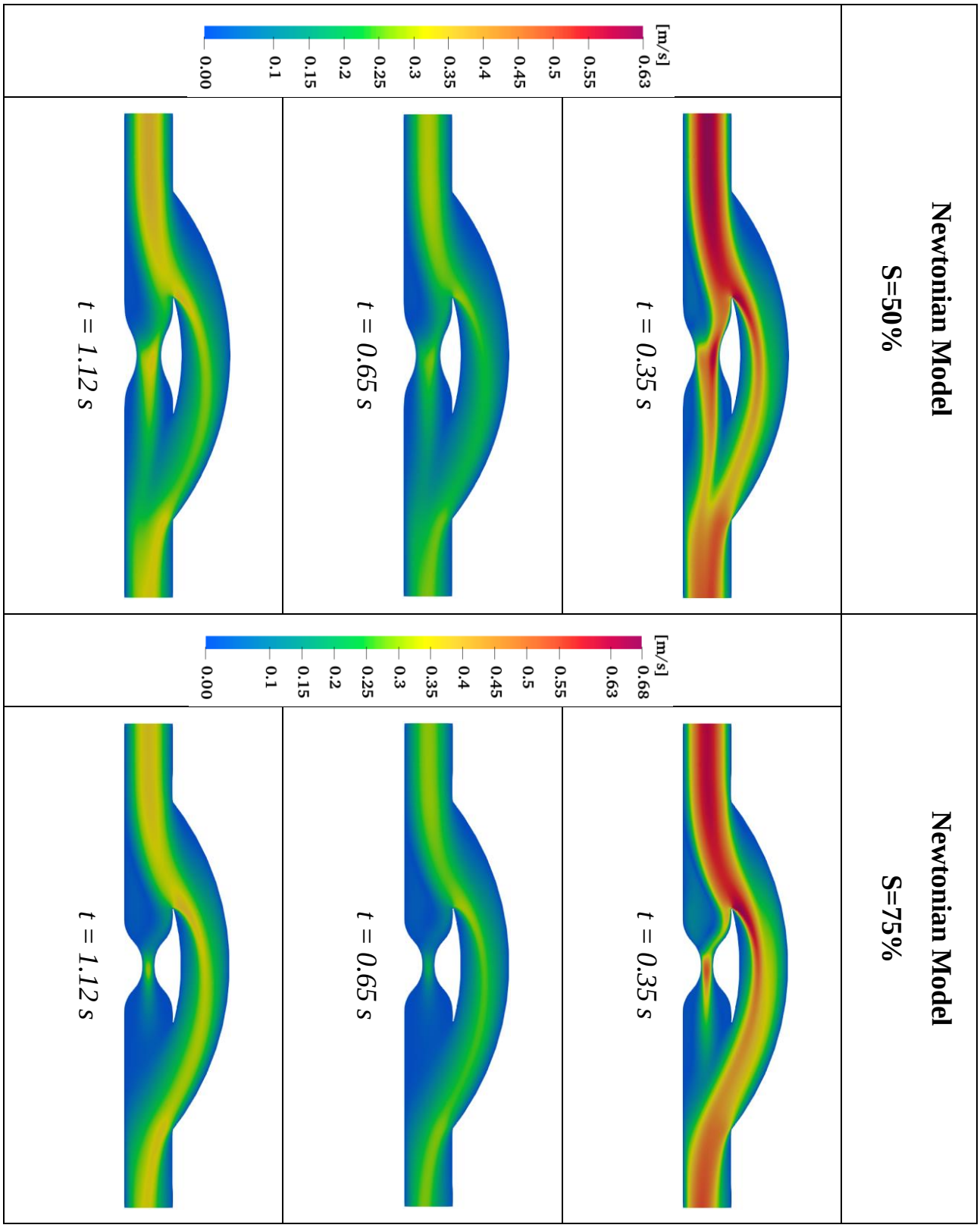

Figure 59. Contour velocity profiles for Newtonian model at different time steps for both stenosis degree (*S=50%* and *S=75%*) [Ref. 7.1]

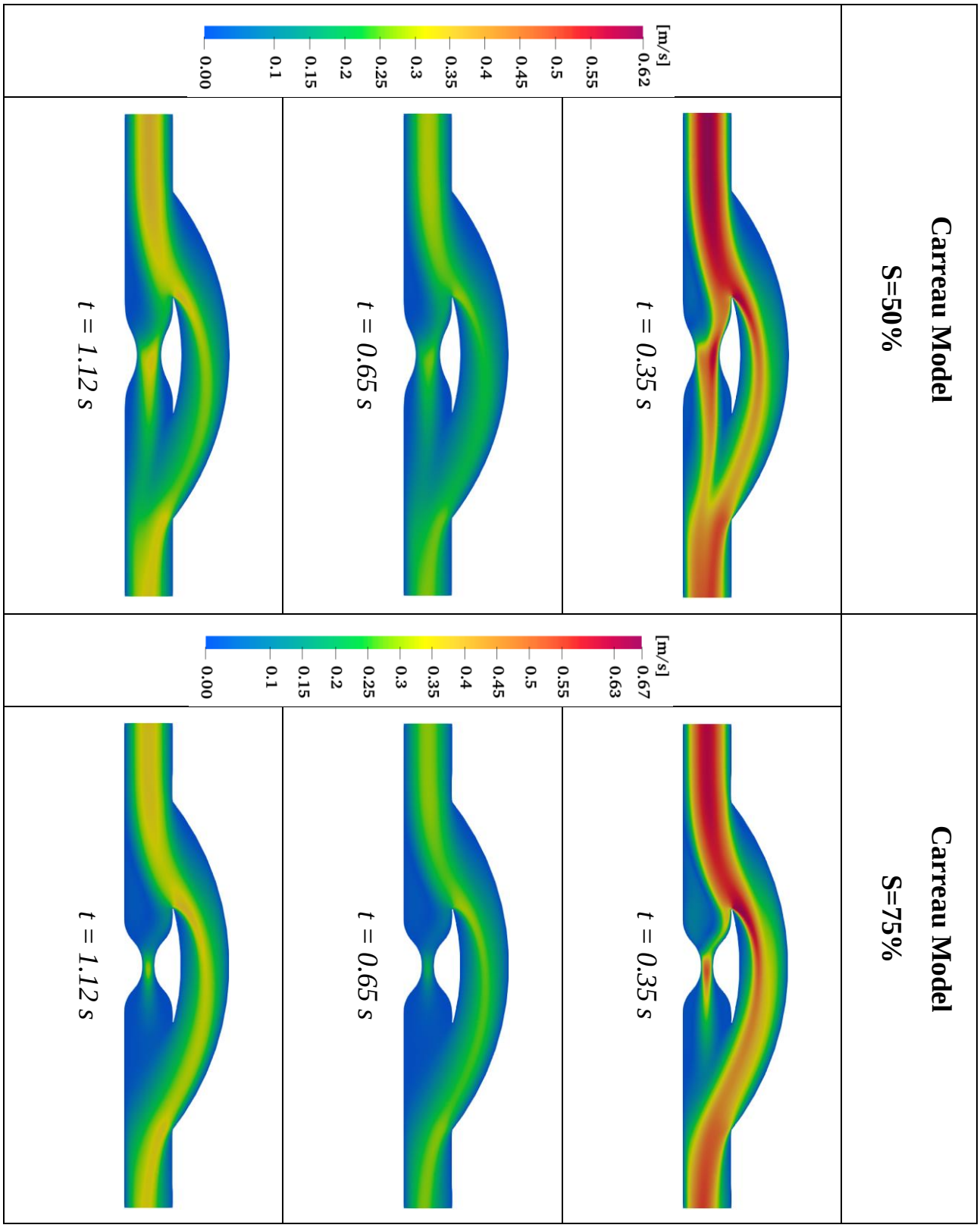

Figure 60. Contour velocity profiles for Carreau model at different time steps for both stenosis degree (*S=50%* and *S=75%*) [Ref. 7.1]

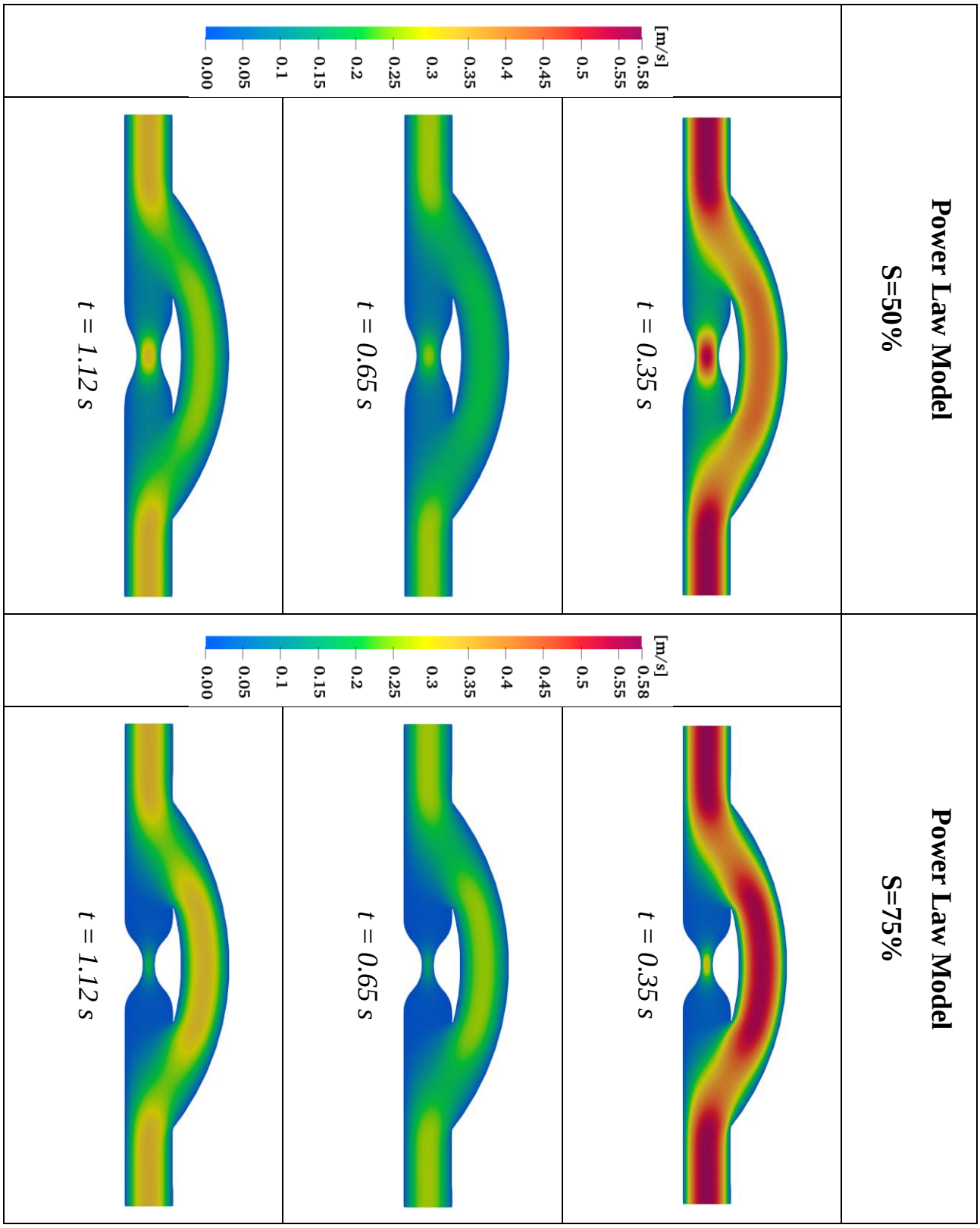

Figure 61. Contour velocity profiles for Power Law model at different time steps for both stenosis degree (*S=50%* and *S=75%*) [Ref. 7.1]

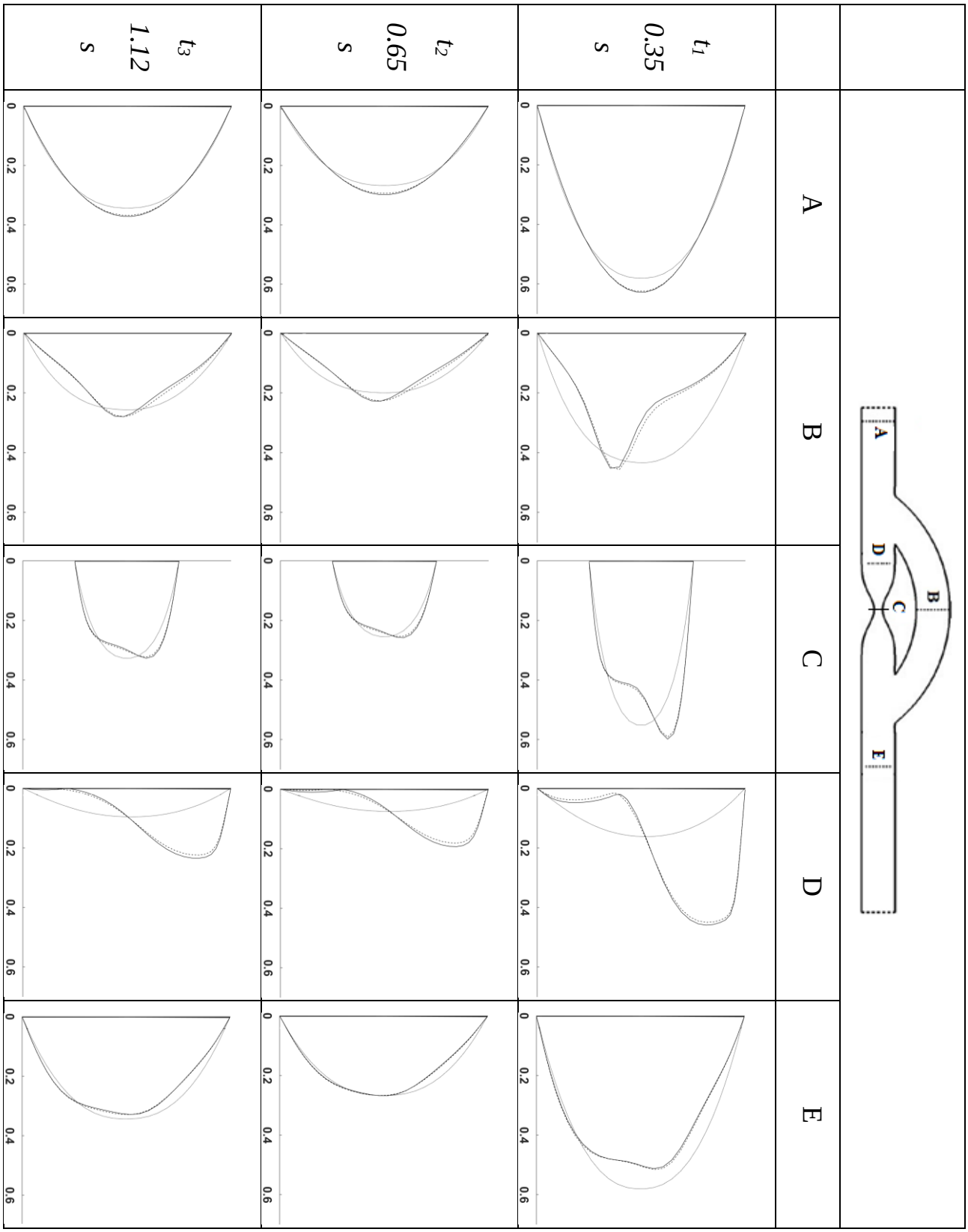

Figure 62. 2D velocity profiles comparison along sections A, B, C, D and E for three time steps (t_1, t_2 and t_3) for stenosis degree *S=50%*. Solid line for Newtonian, dashed line for Carreau and dotted line for Power Law. [Ref. 7.1]

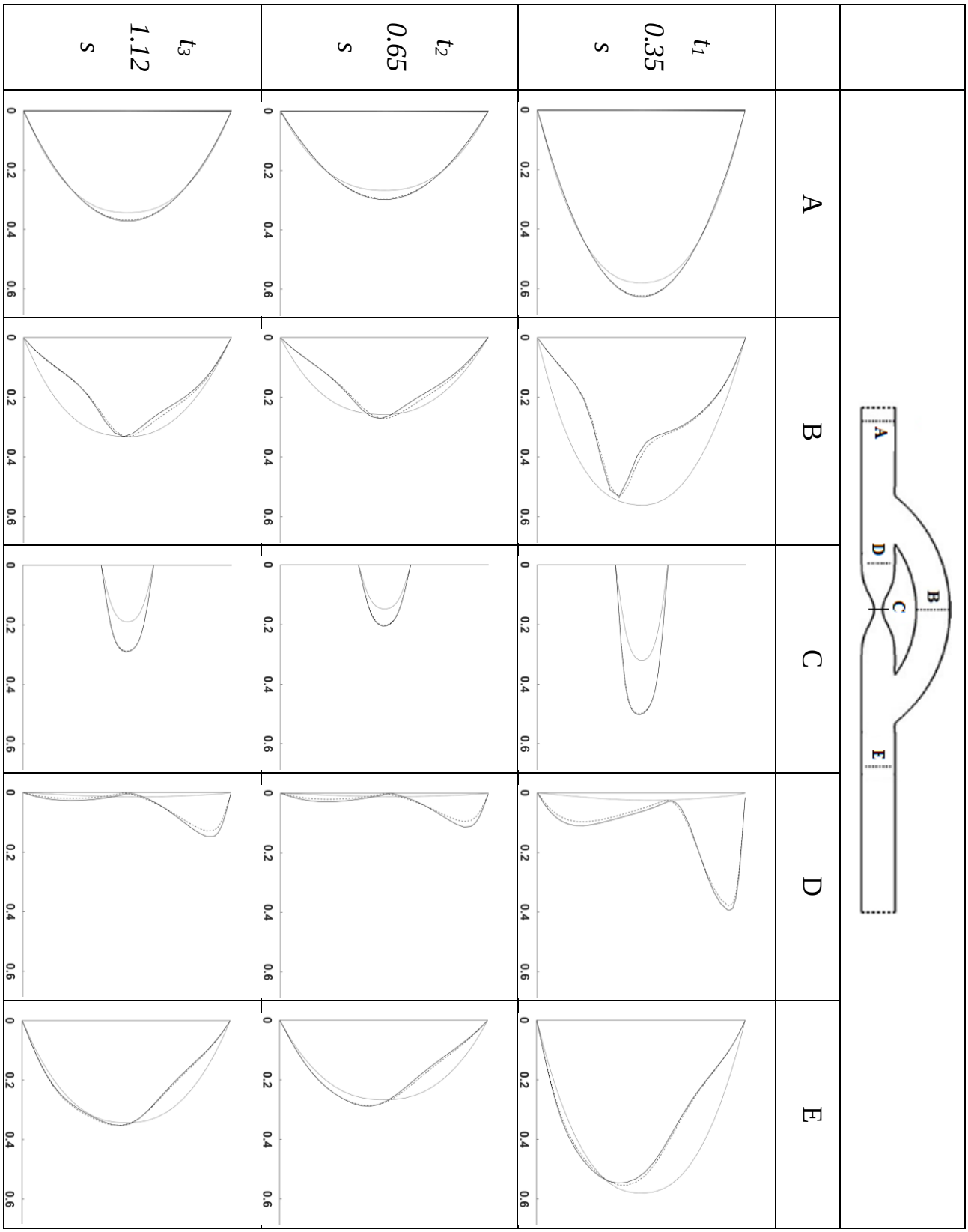

Figure 63. 2D velocity profiles comparison along sections A, B, C, D and E for three time steps (t_1, t_2 and t_3) for stenosis degree *S=75%*. Solid line for Newtonian, dashed line for Carreau and dotted line for Power Law. [Ref. 7.1]

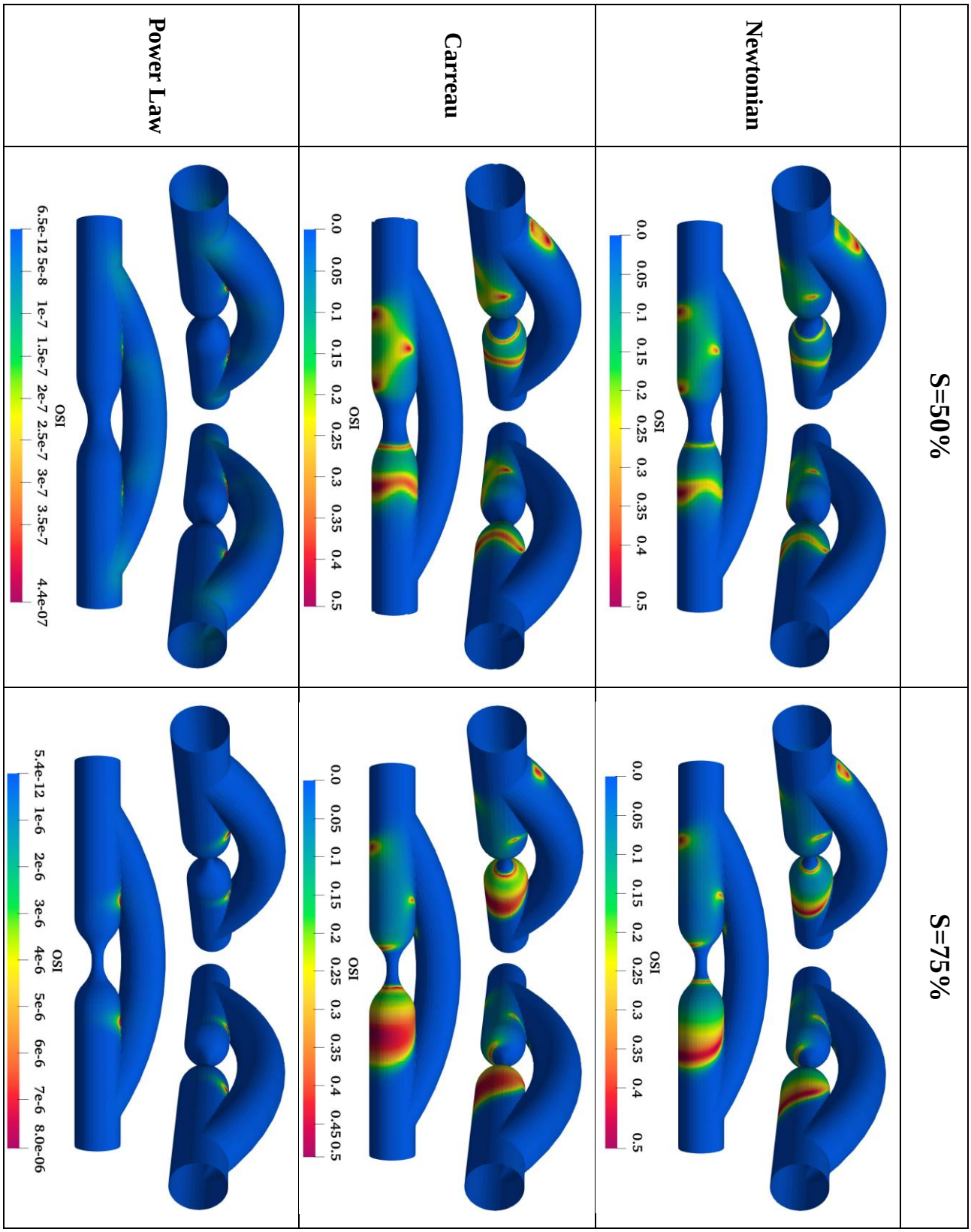

Figure 64. Oscillatory Shear Index (OSI) [Ref. 7.1]

6 Conclusion

This manuscript investigates the Constructal Design method as an innovative method for the research of geometry that maximizes the performance of a specific element, or system, of an engineering nature.

In the first chapter, a general look is given to ideas regarding construction theory, construction law and the construction design method (CDM).

The main features of this topic and the development of some interesting applications (heat transfer, flows in bifurcations) are discussed, and the results presented. Some critical issues on the validity of this theory in engineering problems are explained and the discussion is opened in a critical way by reporting numerous examples in the literature in support of this theory.

The thesis is developed by presenting the mathematical model for the description of the fluid pulsed flow inside a pipe. The result is a Womersley-style velocity profile. It has been pointed out that this profile approaches the Poiseuille parabolic profile only if the Womersley number exceeding 2. The Womersley profile velocity formulation was then used in the cardiac bypass simulations.

Chapter 3 describes the mathematical model of cardiac bypass considering a pulsed flow regime with a Newtonian fluid. Various simulations have been carried out by determining the constraints across the Constructal Design and using the Response Surface methodologies. The result provided the geometric configuration that minimizes pressure drops.

Chapter 4, on the other hand, the similar problem was faced with the aim of identifying the effect on the pressure drops due to the variation of the bypass connection point. The results obtained show a decrease in the pressure drop trend as the distance of the bypass attachment point increases. The decreasing pressure trend

was less pronounced when the stenosis increases. Therefore, the optimum point is the point as far as possible from the shrinkage.

Finally, in chapter 5, the effect on the bypass when the fluid under examination is not Newtonian was investigated. The Newtonian, Carreau and Power Law models were compared. The Power Law model, due to its velocity profile, differs a lot from the other models and the Oscillatory Shear Index (OSI) values are almost zero. The Newtonian model and that of Carreau, on the other hand, are comparable and the differences are almost minimal. It is noted that the accentuated values of OSI occur in the fluid recirculation areas and in the junctions between the bypass and the main vein.

In this work, the topic of Constructal Design for the optimization of a cardiac bypass was mainly dealt with. During the PhD program, other topics were treated and published. In chapter 7 the list of publications is shown.

7 List of Publications

1. **Prediction Capabilities of a One-Dimensional Wall-Flow Particulate Filter Model.** Andrea Natale Impiombato, Cesare Biserni, Massimo Milani, Luca Montorsi. (Submission Proceeding) **2021**.

2. **Pulsatile Bypass Flow: Power Law versus Newtonian model.** Andrea Natale Impiombato, Francesco Orlandi, Giorgio La Civita, Flavia Schwarz Franceschini Zinani, Luiz Alberto Oliveira Rocha, cesare Biserni. (Submission proceedeng on Journal of Advances in Applied & Computational Mathematics) **2021**.

3. **A Simple Transient Poiseuille-Based Function to Mimic Womersley Function and to Model Pulsatile Blood Flow.** Andrea Natale Impiombato, Giorgio La Civita, Francesco Orlandi, Flavia Schwarz Franceschini Zinani, Luiz Rocha, Cesare Biserni. Dynamics. **2021.**

4. **Pulsatile Flow Through an Idealized Arterial Bypass Graft: an Application of the Constructal Design Method.** Andrea Natale Impiombato, Flavia Schwarz Franceschini Zinani, Luiz Rocha, Cesare Biserni. Journal of Applied and Computational Mechanics. **2020.**

5. **Constructal Design of an Idealize Arterial Bypass Graft: Effect of the Bypass Attachment Pointon Resistance to Flow.** Andrea Natale Impiombato, Flavia Schwarz Franceschini Zinani, Luiz Rocha, Cesare Biserni. Journal of Applied and Computational Mechanics. **2020**.

6. **Buoyancy-driven convection in a horizontal porous layer saturated by a power-law fluid: The effect of an open boundary.** Michele Celli, Andrea Natale Impiombato, Antonio Barletta. Interna Journal of Heat an Mass Transfer. **2020**.

7. **Synthesis and characterization of mordenite zeolite from metakaolin and rice husk ash as a source of aluminium and silicon.** Klunk, M.A., Schröpfer, S.B., Dasgupta, S., Das, M., Caetano, N.R., Impiombato, A.N., Wander, P.R., Moraes, C.A.M. Chemical Paper, **2020**.

8. **Onset of thermal convection in a horizontal porous layer saturated by a power-law fluid.** Michele Celli, Andrea Natale Impiombato, Antonio Barletta. 37th UIT Heat Transfer Conference, Padova, 24-26 June **2019**.

9. **Thermal convection of a power-law fluid saturating a horizontal porous layer with an open boundary.** Michele Celli, Andrea Natale Impiombato, Antonio Barletta. International Journal of Heat and Mass Transfer. **2019.**

10. **Couette Vortex Formation and Topology in Duct with an Embedded Cavity: A Possible Application in Flow Structures of Natural Systems.** Eugenia Rossi di Schio, Cesare Biserni, Andrea Natale Impiombato. 19th CIRIAF National Congress, Perugia Italy, April 12, **2019**.

11. **Numerical analysis on building envelope moisture condensation: a case study using the Glaser Diagram Method.** Cesare Biserni and Andrea Natale Impiombato. AIP Conference Proceedings 2191, 020023 (2019). 17 December **2019**.

12. **Comparative study using different external sources of aluminum on the zeolites synthesis from rice husk ash.** Klunk, M.A., Das, M., Dasgupta, S., Impiombato, A.N., Caetano, N.R., Wander, P.R., Moraes, C.A.M. Materials Research Express **2019**.

Appendix A: Pulsatile Flow Rate Description

The pulsed flow within the veins is taken as a reference by the literature (Vimmr et al. [35]) and describes the time-dependent inlet flow rate Q(t) through the Fourier series:

$$Q(t) = Q_0 + \sum_{k=1}^{5} Q_k \cos(k\omega t - \phi_k) \qquad (A.1)$$

where the cardiac cycle period is T=1.68 s, Q_0=65.07 mL/min represents the average inlet flow rate, and Q_k, and φ_k, k=1,…,5 are the amplitude and phase angle, respectively. The values of Eq.(A.1) are coherent with the ones found by Vimmr et al. [35]: Q_1=18.149 mL/min, Q_2=34.828 mL/min, Q_3=12.329 mL/min, Q_4=9.107 mL/min, Q_5=2.944 mL/min, φ_1=1.944 rad, φ_2=2.836 rad, φ_3=-2.124 rad, φ_4=-1.875 rad and φ_5=-0.447 rad (Figure A.1).

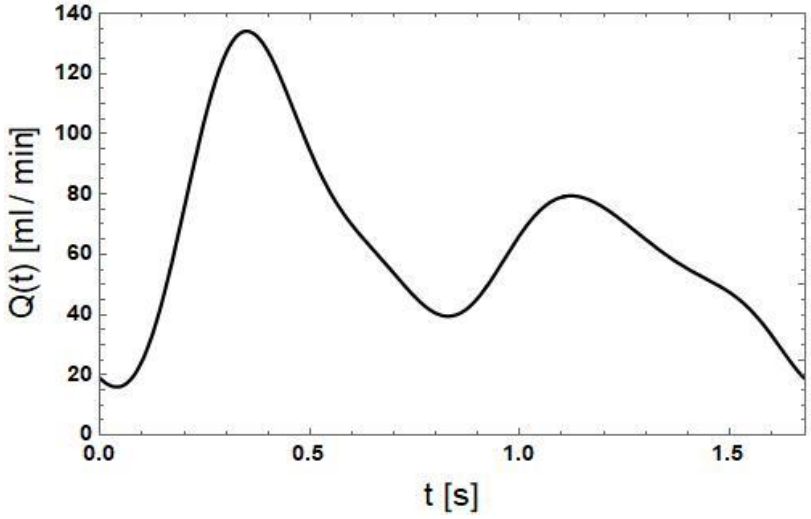

Figure A.1. Time-dependent flow rate Q(t) [Ref. 7.3]

Bibliography

[1] A. Bejan and S. Lorente, “The constructal law of design and evolution in nature,” *Philos. Trans. R. Soc. B Biol. Sci.*, vol. 365, no. 1545, pp. 1335–1347, 2010, doi: 10.1098/rstb.2009.0302.

[2] A. Bejan, “Design with Constructal Law,” vol. 22, no. 1, pp. 140–147, 2008.

[3] L. A. O. Rocha, S. Lorente, and A. Bejan, *Constructal theory in heat transfer*. 2018.

[4] A. Bejan, “Constructal-theory network of conducting paths for cooling a heat generating volume,” *Int. J. Heat Mass Transf.*, vol. 40, no. 4, pp. 799–811, 1997, doi: 10.1016/0017-9310(96)00175-5.

[5] A. Bejan, *The physics of life: the evolution of everything*. St. Martin’s Press, 2016.

[6] A. Kosner, “‘Freedom is good for design,’How to use Constructal Theory to liberate any flow system.” Forbes, 2012.

[7] G. Lorenzini, C. Biserni, E. Da Silva Diaz Estrada, E. D. Dos Santos, L. A. Isoldi, and L. A. O. Rocha, “Genetic algorithm applied to geometric optimization of isothermal Y-shaped cavities,” *J. Electron. Packag. Trans. ASME*, vol. 136, no. 3, pp. 1–9, 2014, doi: 10.1115/1.4027421.

[8] C. Biserni, L. A. O. Rocha, and A. Bejan, “Inverted fins: Geometric optimization of the intrusion into a conducting wall,” *Int. J. Heat Mass Transf.*, vol. 47, no. 12–13, pp. 2577–2586, 2004, doi: 10.1016/j.ijheatmasstransfer.2003.12.018.

[9] L. A. O. Rocha, G. Lorenzini, C. Biserni, and Y. Cho, “Constructal design of a cavity cooled by convection,” *Int. J. Des. Nat. Ecodynamics*, vol. 5, no. 3, pp. 212–220, 2010, doi: 10.2495/DNE-V5-N3-212-220.

[10] G. Lorenzini, C. Biserni, L. A. Isoldi, E. D. Dos Santos, and L. A. O. Rocha, “Constructal design applied to the geometric optimization of Y-shaped cavities embedded in a conducting medium,” *J. Electron. Packag. Trans. ASME*, vol. 133, no. 4, pp. 1–8, 2011, doi: 10.1115/1.4005296.

[11] C. Biserni, L. A. O. Rocha, G. Stanescu, and E. Lorenzini, “Constructal H-shaped cavities according to Bejan’s theory,” *Int. J. Heat Mass Transf.*, vol. 50, no. 11–

12, pp. 2132–2138, 2007, doi: 10.1016/j.ijheatmasstransfer.2006.11.006.

[12] A. Bejan and S. Lorente, “Constructal theory of generation of configuration in nature and engineering,” *J. Appl. Phys.*, vol. 100, no. 4, 2006, doi: 10.1063/1.2221896.

[13] A. Bejan, S. Lorente, and J. Lee, “Unifying constructal theory of tree roots, canopies and forests,” *J. Theor. Biol.*, vol. 254, no. 3, pp. 529–540, 2008, doi: 10.1016/j.jtbi.2008.06.026.

[14] A. H. Reis and A. Bejan, “Constructal theory of global circulation and climate,” *Int. J. Heat Mass Transf.*, vol. 49, no. 11–12, pp. 1857–1875, 2006, doi: 10.1016/j.ijheatmasstransfer.2005.10.037.

[15] A. Bejan, V. Badescu, and A. De Vos, “Constructal theory of economics,” *Appl. Energy*, vol. 67, no. 1–2, pp. 37–60, 2000, doi: 10.1016/S0306-2619(00)00023-4.

[16] H. Wang, W. Dai, and A. Bejan, “Optimal temperature distribution in a 3D triple-layered skin structure embedded with artery and vein vasculature and induced by electromagnetic radiation,” *Int. J. Heat Mass Transf.*, vol. 50, no. 9–10, pp. 1843–1854, 2007, doi: 10.1016/j.ijheatmasstransfer.2006.10.005.

[17] A. Bejan, “Constructal thermodynamics: Life and evolution as physics,” in *Proc. Constructal Law & Second Law Conference*, 2015, pp. 19--37.

[18] M. Birla, *FedEx Delivers: How the World’s Leading Shipping Company Keeps Innovating and Outperforming the Competition*. John Wiley & Sons, 2013.

[19] G. R. McGhee, *Convergent evolution: limited forms most beautiful*. MIT Press, 2011.

[20] J. Burstein and K. Andersen, *Spark: How creativity works*. Harper Collins, 2011.

[21] V. W. Hwang and G. Horowitt, “The rainforest: The secret to building the next Silicon Valley,” *Regenwald Los Altos Hills, CA*, 2012.

[22] E. R. Weibel, *Symmorphosis: on form and function in shaping life*. Harvard University Press, 2000.

[23] C. D. Murray, “The physiological principle of minimum work: I. The vascular system and the cost of blood volume,” *Proc. Natl. Acad. Sci. U. S. A.*, vol. 12, no. 3, p. 207, 1926.

[24] A. Bejan, L. Rocha, and S. Lorente, “Thermodynamic optimization of geometry: T-and Y-shaped constructs of fluid streams,” *Int. J. Therm. Sci.*, vol. 39, no. 9–11, pp. 949--960, 2000.

[25] W. Wechsatol, S. Lorente, and A. Bejan, “Optimal tree-shaped networks for fluid flow in a disc-shaped body,” *Int. J. Heat Mass Transf.*, vol. 45, no. 25, pp. 4911–4924, 2002.

[26] L. Gosselin and A. Bejan, “Tree networks for minimal pumping power,” *Int. J. Therm. Sci.*, vol. 44, no. 1, pp. 53--63, 2005.

[27] L. Gosselin and A. Bejan, “Emergence of asymmetry in constructal tree flow networks,” *J. Appl. Phys.*, vol. 98, no. 10, pp. 104--903, 2005.

[28] W. Wechsatol, A. Bejan, and S. Lorente, “Tree-shaped flow architectures: strategies for increasing optimization speed and accuracy,” *Numer. Heat Transf. Part A Appl.*, vol. 48, no. 8, pp. 731--744, 2005.

[29] Z. Lu, K. Zhang, J. Liu, and F. Li, “Effect of branching level on the performance of constructal theory based Y-shaped liquid cooling heat sink,” *Appl. Therm. Eng.*, vol. 168, no. December 2019, p. 114824, 2020, doi: 10.1016/j.applthermaleng.2019.114824.

[30] L. Kuddusi and N. Eğrican, “A critical review of constructal theory,” *Energy Convers. Manag.*, vol. 49, no. 5, pp. 1283–1294, 2008, doi: 10.1016/j.enconman.2007.05.023.

[31] L. Ghodoossi, “Conceptual study on constructal theory,” *Energy Convers. Manag.*, vol. 45, no. 9–10, pp. 1379–1395, 2004, doi: 10.1016/j.enconman.2003.09.002.

[32] O. Yenigun and E. Cetkin, “Experimental and numerical investigation of constructal vascular channels for self-cooling: Parallel channels, tree-shaped and hybrid designs,” *Int. J. Heat Mass Transf.*, vol. 103, pp. 1155–1165, 2016, doi: 10.1016/j.ijheatmasstransfer.2016.08.074.

[33] J. R. Womersley, “Method for the calculation of velocity, rate of flow and viscous drag in arteries when the pressure gradient is known,” *J. Physiol.*, vol. 3, no. Wiley Online Library, pp. 553--563, 1955.

[34] A. N. Impiombato, G. La Civita, F. Orlandi, F. S. Franceschini Zinani, L. A. Oliveira Rocha, and C. Biserni, “A Simple Transient Poiseuille-Based Approach to Mimic the Womersley Function and to Model Pulsatile Blood Flow,” *Dynamics*, vol. 1, no. 1, pp. 9–17, 2021, doi: 10.3390/dynamics1010002.

[35] J. Vimmr, A. Jonášová, and O. Bublík, “Effects of three geometrical parameters on pulsatile blood flow in complete idealised coronary bypasses,” *Comput. Fluids*, vol. 69, pp. 147–171, 2012, doi: 10.1016/j.compfluid.2012.08.007.

[36] C. Loudon and A. Tordesillas, “The use of the dimensionless Womersley number

to characterize the unsteady nature of internal flow," *J. Theor. Biol.*, vol. 191, no. 1, pp. 63–78, 1998, doi: 10.1006/jtbi.1997.0564.

[37] T. J. Pedley, "Arterial and venous fluid dynamics," in *Cardiovascular fluid mechanics*, Springer, 2003, pp. 1--72.

[38] D. Ku, "Pulsatile flow and atherosclerosis in the human carotid bifurcation. Positive correlation between plaque location and low oscillating shear stress. Arteriosclerosis," *Int. Commun. Heat Mass Transf.*, vol. 35, no. 10, pp. 1360–1367, 2008, doi: http://dx.doi.org/10.1016/j.icheatmasstransfer.2008.06.010.

[39] F.-B. Tian, L. Zhu, P.-W. Fok, and X.-Y. Lu, "Simulation of a pulsatile non-Newtonian flow past a stenosed 2D artery with atherosclerosis," *Comput. Biol. Med.*, vol. 43, no. 9, pp. 1098--1113, 2013, doi: https://doi.org/10.1016/j.compbiomed.2013.05.023.

[40] G. Liu, J. Wu, D. N. Ghista, W. Huang, and K. K. Wong, "Hemodynamic characterization of transient blood flow in right coronary arteries with varying curvature and side-branch bifurcation angles," *Comput. Biol. Med.*, vol. 64, pp. 117--126, 2015, doi: http://dx.doi.org/10.1016/j.compbiomed.2015.06.009.

[41] B. Guerciotti, C. Vergara, S. Ippolito, A. Quarteroni, C. Antona, and R. Scrofani, "A computational fluid--structure interaction analysis of coronary Y-grafts," *Med. Eng. Phys.*, vol. 47, pp. 117--127, 2017.

[42] H. S. Bassiouny, S. White, S. Glagov, E. Choi, D. P. Giddens, and C. K. Zarins, "Anastomotic intimal hyperplasia: mechanical injury or flow induced," *J. Vasc. Surg.*, vol. 15, no. 4, pp. 708--717, 1992.

[43] R. F. Dutra, F. S. Zinani, L. A. Rocha, and C. Biserni, "Constructal design of an arterial bypass graft," *Heat Transf.*, vol. 49, no. 7, pp. 4019--4039, 2020.

[44] C. Bertolotti and V. Deplano, "Three-dimensional numerical simulations of flow through a stenosed coronary bypass," *J. Biomech.*, vol. 33, no. 8, pp. 1011--1022, 2000.

[45] T. Ko, K. Ting, and H. Yeh, "Numerical investigation on flow fields in partially stenosed artery with complete bypass graft: An in vitro study," *Int. Commun. heat mass Transf.*, vol. 34, no. 6, pp. 713--727, 2007.

[46] D. Lee, J. Su, and H. Liang, "A numerical simulation of steady flow fields in a bypass tube," *J. Biomech.*, vol. 34, no. 11, pp. 1407--1416, 2001.

[47] L. P. Chua, J. Zhang, and T. Zhou, "Numerical study of a complete anastomosis model for the coronary artery bypass," *Int. Commun. heat mass Transf.*, vol. 32, no. 3–4, pp. 473--482, 2005.

[48] T. Fan *et al.*, “Hemodynamics of left internal mammary artery bypass graft: effect of anastomotic geometry, coronary artery stenosis, and postoperative time,” *J. Biomech.*, vol. 49, no. 5, pp. 645--652, 2016.

[49] T. Ko, K. Ting, and H. Yeh, “A numerical study on the effects of anastomotic angle on the flow fields in a stenosed artery with a complete bypass graft,” *Int. Commun. heat mass Transf.*, vol. 35, no. 10, pp. 1360--1367, 2008.

[50] M. W. Roos, E. Wadbro, and M. Berggren, “Computational estimation of fluid mechanical benefits from a fluid deflector at the distal end of artificial vascular grafts,” *Comput. Biol. Med.*, vol. 43, no. 2, pp. 164--168, 2013.

[51] A. Post *et al.*, “Elucidating the role of graft compliance mismatch on intimal hyperplasia using an ex vivo organ culture model,” *Acta Biomater.*, vol. 89, pp. 84--94, 2019.

[52] F. Xiong and C. Chong, “A parametric numerical investigation on haemodynamics in distal coronary anastomoses,” *Med. Eng. Phys.*, vol. 30, no. 3, pp. 311--320, 2008.

[53] H. Do, A. A. Owida, W. Yang, and Y. S. Morsi, “Numerical simulation of the haemodynamics in end-to-side anastomoses,” *Int. J. Numer. Methods Fluids*, vol. 67, no. 5, pp. 638--650, 2011.

[54] A. Tiwari, P. D. Shah, and S. S. Chauhan, “Analytical study of micropolar fluid flow through porous layered microvessels with heat transfer approach,” *Eur. Phys. J. Plus*, vol. 135, no. 2, p. 209, 2020.

[55] A. Bejan, “The geometric structures derived from this principle for engineering applications are named constructal designs,” *Adv. Eng. Thermodyn.*, 1997.

[56] A. Bejan and J. P. Zane, *Design in nature: How the constructal law governs evolution in biology, physics, technology, and social organizations*. 2013.

[57] U. Lucia, G. Grisolia, and M. R. Astori, “Constructal law analysis of Cl- transport in eyes aqueous humor,” *Sci. Rep.*, vol. 7, no. 1, pp. 1--4, 2017.

[58] U. Lucia, G. Grisolia, D. Dolcino, M. R. Astori, E. Massa, and A. Ponzetto, “Constructal approach to bio-engineering: the ocular anterior chamber temperature,” *Sci. Rep.*, vol. 6, no. 1, pp. 1--6, 2016.

[59] J. C. Slattery, *Advanced transport phenomena*. Cambridge University Press, 1999.

[60] S. Berger and L.-D. Jou, “Flows in stenotic vessels,” *Annu. Rev. Fluid Mech.*, vol. 32, no. 1, pp. 347--382, 2000.

[61] K. Perktold, M. Resch, and H. Florian, “Pulsatile non-Newtonian flow characteristics in a three-dimensional human carotid bifurcation model,” *J Biomech Eng*, vol. 113, pp. 464–475, 1991.

[62] F. Gijsen, E. Allanic, F. Van De Vosse, and J. Janssen, “The influence of the non-Newtonian properties of blood on the flow in large arteries: unsteady flow in a 90 curved tube,” *J. Biomech.*, vol. 32, no. 7, pp. 705--713, 1999.

[63] K. Perktold, R. Peter, and M. Resch, “Pulsatile non-Newtonian blood flow simulation through a bifurcation with an aneurysm,” *Biorheology*, vol. 26, no. 6, pp. 1011--1030, 1989.

[64] A. Tiwari and S. S. Chauhan, “Effect of varying viscosity on two-fluid model of blood flow through constricted blood vessels: a comparative study,” *Cardiovasc. Eng. Technol.*, vol. 10, no. 1, pp. 155--172, 2019.

[65] D. Kumar, R. Vinoth, and V. S. Raviraj Adhikari, “Non-Newtonian and Newtonian blood flow in human aorta: A transient Analysis,” *Biomed. Res.*, 2017.

[66] S. V Patankar, “Numerical Heat Transfer and Fluid Flow,’McGraw-Hill, New York,” 1980.

[67] A. Fluent, “Ansys fluent,” *Acad. Res. Release*, 2019.

[68] I. B. Celik, P. J. Ghia, Urmila and Roache, and C. J. Freitas, “Procedure for estimation and reporting of uncertainty due to discretization in CFD applications,” *J. fluids Eng. ASME*, vol. 130, no. 7, 2008.

[69] A. Razera, R. da Fonseca, L. Isoldi, E. dos Santos, L. Rocha, and C. Biserni, “Constructal design of a semi-elliptical fin inserted in a lid-driven square cavity with mixed convection,” *Int. J. Heat Mass Transf.*, vol. 126, pp. 81--94, 2018.

[70] R. Klein, C. Biserni, F. Zinani, and L. Rocha, “Constructal Design of tube arrangements for heat transfer to non-Newtonian fluids,” *Int. J. Mech. Sci.*, vol. 133, pp. 590--597, 2017.

[71] H. TSUKUI, M. SHINKE, Y. K. PARK, and K. YAMAZAKI, “Longer coronary anastomosis provides lower energy loss in coronary artery bypass grafting.,” *Heart Vessels*, vol. 32, no. 1, pp. 83--89, 2017, doi: http://dx.doi.org/10.1007/s00380-016-0880-4.

[72] D. N. Ku, D. P. Giddens, C. K. Zarins, and S. Glagov, “Pulsatile Flow and Atherosclerosis in the Human Carotid Bifurcation,” *Ateriosclerosis*, vol. 5, pp. 293--302, 1985.

[73] C. Bertolotti, V. Deplano, J. Fuseri, and P. Dupouy, “Numerical and experimental models of post-operative realistic flows in stenosed coronary bypasses,” *J. Biomech.*, vol. 34, no. 8, pp. 1049--1064, 2001.

[74] S.] Koksungnoen, P. Rattanadecho, and P. Wongchadakul, “numerical model of blood flow in the coronary artery bypass graft during no pulse and pulse situations: Effects of an anastomotic angle and characteristics of fluid,” *J. Mech. Sci. Technol.*, vol. 32, pp. 4545--4552, 2018.

[75] F. Ballarin *et al.*, “Numerical modeling of hemodynamics scenarios of patient-specific coronary artery bypass grafts,” *Biomech. Model. Mechanobiol.*, vol. 16, pp. 1373--1399, 2017.

[76] F. Kabinejadian and D. N. Ghista, “Compliant model of a coupled sequential coronary arterial bypass graft: Effects of vessel wall elasticity and non-Newtonian rheology on blood flow regime and hemodynamic parameters distribution,” *Med. Eng. Phys.*, vol. 34, pp. 860--872, 2012.

[77] S. O’Callaghan, M. Walsh, and T. McGloughlin, “Numerical modelling of Newtonian and non-Newtonian representation of blood in a distal end-to-side vascular bypass graft anastomosis,” *Med. Eng. Phys.*, vol. 28, pp. 70--74, 2006.

[78] J. P. Ku, C. J. Elkins, and C. A. Taylor, “Comparison of CFD and MRI Flow and Velocities in an In Vitro Large Artery Bypass Graft Model,” *Ann. Biomed. Eng.*, vol. 33, pp. 257--269, 2005.

[79] M. Bonert, J. G. Myers, S. Fremes, J. Williams, and C. R. Ethier, “A Numerical Study of Blood Flow in Coronary Artery Bypass Graft Side-to-Side Anastomoses,” *Ann. Biomed. Eng.*, vol. 30, pp. 599--611, 2002.

[80] G. Troina *et al.*, “Computational Modeling and Constructal Design Theory Applied to the Geometric Optimization of Thin Steel Plates with Stiffeners Subjected to Uniform Transverse Load,” *Metals (Basel).*, vol. 10, pp. 220--249, 2020.

[81] R. R. Amaral *et al.*, “Constructal design method dealing with stiffened plates and symmetry boundaries,” *Theor. Appl. Mech. Lett.*, vol. 10, pp. 366--376, 2020.

[82] A. Bejan, *Advanced Engineering Thermodynamics. 2nd ed.* New York: John Wiley & Sons, 1997.

[83] A. K. Politis, G. P. Stavropoulos, M. N. Christolis, F. G. Panagopoulos, N. S. Vlachos, and N. C. Markatos, “Numerical modeling of simulated blood flow in idealized composite arterial coronary grafts: Steady state simulations,” *J. Biomech.*, vol. 40, pp. 1125--1136, 2007.

[84] J. Vimmr and A. Jon'avsov'a, "Non-Newtonian effects of blood flow in complete coronary and femoral bypasses," *Math. Comput. Simul.*, vol. 80, no. 6, pp. 1324--1336, 2010.

[85] A. Bejan, *Convection heat transfer*. John Wiley & Sons, 2013.

[86] B. Baliga and S. Patankar, "A new finite-element formulation for convection-diffusion problems," *Numer. Heat Transf.*, vol. 3, no. 4, pp. 393--409, 1980.

[87] R. B. Bird, R. C. Armstrong, and O. Hassager, "Dynamics of polymeric liquids. Vol. 1: Fluid mechanics," 1987.

[88] R. Bird, W. Stewart, and E. Lightfoot, "Interphase transport in nonisothermal mixtures," *Transp. Phenomena, 2nd ed.(John Wiley Sons, Inc., New York, United States Am. 2007)*, p. 679, 2002.

[89] D. Boger, "A highly elastic constant-viscosity fluid," *J. Nonnewton. Fluid Mech.*, vol. 3, no. 1, pp. 87--91, 1977.

[90] G. Prilutski, R. Gupta, T. Sridhar, and M. Ryan, "Model viscoelastic liquids," *J. Nonnewton. Fluid Mech.*, vol. 12, no. 2, pp. 233--241, 1983.

[91] P. J. Carreau and Others, "Rheology of polymeric systems: principles and applications," 1997.

[92] R. B. Bird, "Useful non-Newtonian models," *Annu. Rev. Fluid Mech.*, vol. 8, no. 1, pp. 13--34, 1976.

[93] P. J. Carreau, "Rheological equations from molecular network theories," *Trans. Soc. Rheol.*, vol. 16, no. 1, pp. 99--127, 1972.

[94] M. M. Cross, "Rheology of non-Newtonian fluids: a new flow equation for pseudoplastic systems," *J. Colloid Sci.*, vol. 20, no. 5, pp. 417--437, 1965.

[95] W. H. Boersma, J. Laven, and H. N. Stein, "Shear thickening (dilatancy) in concentrated dispersions," *AIChE J.*, vol. 36, no. 3, pp. 321--332, 1990.

[96] X. He and D. N. Ku, "Pulsatile flow in the human left coronary artery bifurcation: average conditions," *J. Biomech. Eng.*, vol. 118, no. 1, pp. 74--82, 1996.

Acknowledgement

There are many people to whom I owe recognition for the support given to me over the years. I thank Professors Antonio Barletta and Michele Celli who were the first to stimulate my enthusiasm to undertake the path of the doctorate. I thank Prof. Cesare Biserni who transmitted me a lot of his method, supported me in the face of difficulties and allowed me to meet as many people who made me grow professionally and as a person. In particular, I thank Prof. Flavia S.F. Zinani and Professor Luiz A.O. Rocha who welcomed me into their group during the stay to Brazil and helped me in the development of the thesis topic.

I owe a special thanks to my family that allowed me to undertake the path of the doctorate by supporting me in all my choices. I thank my sister Giò and her partner Nicola for giving us two beautiful children.

A last, but not least, thanks to all my brazilian friends with whom I created a second family and gave me moments of extreme joy.

With Affection

Andrea N. Impiombato